To my wife Iwona,
my dearest support in everything I do.

Silesian University of Technology

Department of Thermal Engineering
Faculty of Energy and Environmental Engineering
Silesian University of Technology, Poland

Experimental investigation of the solar pyrolysis of waste biomass

Ph.D. thesis of

Szymon Sobek, MSc, Eng.

Supervisor:

Dr hab. inż. Sebastian Werle, prof. PŚ, Silesian University of Technology

Gliwice, 2021

Abstract

The Ph.D. thesis presents the results of experimental research on the solar pyrolysis of waste biomass carried out on a bench-scale test stand designed by the Author. The first chapters of the work present a literature review of solar pyrolysis and the basic theoretical issues of the process itself. In the work, the author presented a design of a solar pyrolysis reactor powered by artificial solar radiation, according to the original concept of indirect heating of biomass, responding to the problems of heat loss in reactors made of transparent materials described in the literature. Laboratory experiments were carried out for samples of three types of waste biomass: waste wood, waste straw, and sewage sludge.

On the designed test stand, the course of the biomass pyrolysis was examined and described, taking into account: the shares and quality of pyrolysis products, measurement of temperature profiles, the actual heating rates of samples during the process, and the formation of the main gas products. The shares of the products together with the determined values of the heat of combustion based on their elemental composition allowed to determine the chemical energy conversion factors of the fuel (biomass). Apart from the experimental results, the paper also presents the methodology for determining the parameters of the kinetics of the pyrolysis reaction of the tested fuels based on thermogravimetric measurements (TGA). Based on the latest literature, the current kinetic methods such as model-fitting, deconvolution, and model-free, isoconversional techniques were used.

The studies for all types of biomass showed the dominant share of the liquid fraction, the so-called bio-oils in products. Thanks to the adopted measurement methodology, it was possible to obtain pyrolysis gas rich in hydrogen, however, with a low share in the final products, with a mass fraction of less than 12%. The thesis was confirmed that solar pyrolysis may be an original method of producing high porosity char, depending on the process parameters and the type of feedstock. In the case of straw, exceeding the melting temperatures of ash during pyrolysis resulted in a significant loss of the porous surface. The increase in calorific value of solid products of solar pyrolysis of lignocellulosic biomass was denoted, concerning the primary chemical energy of biomass. Determination of the biomass chemical energy conversion indexes allowed to state that only the solar pyrolysis of wood resulted in a measurable increase in the chemical energy content in products (+ 12%), in the case of other biomass samples only the opposite effect was noted.

The proposed methodology for determining the parameters of the kinetics of the pyrolysis reaction is based on a combination of isoconversional methods and traditional methods based on reaction models. Friedman's method provided valuable information on the complexity of the pyrolysis process and the values of initial parameters for further calculations. As a result of kinetic computations, it was shown that the pyrolysis of waste wood and straw was subject to the mechanism of 3 independent reactions, the so-called pseudo-components whose physical meaning is attributed to the independent breakdown of cellulose, hemicelluloses, and lignin. The same methodology was used to select the mechanism of sewage sludge pyrolysis kinetics - a model of 10 independent reactions, the assignment of which to the decomposition of substances is problematic due to the complexity of the composition of the sludge itself. The kinetic models determined based on

the obtained parameters made it possible to predict the behavior of biomass samples in the reactor during experiments on a laboratory scale.

Streszczenie

W pracy doktorskiej przedstawiono wyniki badań eksperymentalnych procesu solarnej pirolizy biomasy odpadowej realizowanych na zaprojektowanym przez Autora stanowisku badawczym napędzanym sztucznym promieniowaniem słonecznym. W pierwszych rozdziałach pracy przedstawiono przegląd literatury badań pirolizy solarnej oraz podstawowe zagadnienia teoretyczne samego procesu. W pracy Autor zaprezentował projekt reaktora pirolizy solarnej według oryginalnej koncepcji pośredniego ogrzewania biomasy przez przegrodę, odpowiadając na opisane w literaturze problemy strat ciepła w reaktorach wykonanych z materiałów transparentnych. Eksperymenty laboratoryjne przeprowadzono dla próbek trzech rodzajów biomasy odpadowej: drewna odpadowego, słomy odpadowej oraz osadów ściekowych.

Na zaprojektowanym stanowisku badawczym, zbadano i opisano przebieg pirolizy biomasy z uwzględnieniem: udziałów i jakości produktów pirolizy, pomiaru profili temperatur, szybkości nagrzewania próbek w trakcie trwania procesu oraz formacji głównych produktów gazowych. Udziały produktów wraz z wyznaczonymi wartościami ciepła spalania na podstawie ich składu pierwiastkowego pozwoliły na wyznaczenie współczynników konwersji energii chemicznej paliwa (biomasy). Oprócz wyników eksperymentalnych w pracy przedstawiono również metodykę wyznaczania parametrów kinetyki reakcji pirolizy badanych paliw na podstawie pomiarów termograwimetrycznych (TGA). Na podstawie informacji z najnowszej literatury wykorzystano aktualne metody kinetyczne ang. *model-fitting*, *deconvolution* oraz techniki izokonwersji.

W badaniach dla wszystkich rodzajów biomasy wykazano dominujący udział frakcji ciekłej tzw. bio olejów w produktach. Dzięki przyjętej metodyce pomiarów w pracy zdołano uzyskać gaz pirolityczny bogaty w wodór, jednakże o niskich udziałach w produktach procesowych, z udziałem masowym poniżej 12 %. Potwierdzono tezę, że piroliza solarna może być oryginalną metodą produkcji karbonizatów o dużej porowatości zależnej od parametrów prowadzenia procesu oraz rodzaju surowca wsadowego. W przypadku słomy przekroczenie temperatur topnienia popiołu w trakcie pirolizy spowodowało znaczną utratę powierzchni porowatej. Odnotowano również wzrost kaloryczności stałych produktów pirolizy solarnej biomasy lignocelulozowej w stosunku do pierwotnej energii chemicznej biomasy. Wyznaczenie wskaźników konwersji energii chemicznej biomasy pozwoliło stwierdzić, że jedynie piroliza solarna drewna zaowocowała wymiernym wzrostem zawartości energii chemicznej w produktach (+12%).

Proponowana metodyka wyznaczania parametrów kinetyki reakcji pirolizy oparta jest o połączenie metod izokonwersji oraz tradycyjnych metod opartych o modele reakcji. Metoda Friedmana dostarczyła cennych informacji na temat złożoności procesu pirolizy, oraz wartości parametrów początkowych do dalszych obliczeń. W wyniku obliczeń kinetycznych wykazano, że piroliza drewna odpadowego i słomy podlegała mechanizmowi 3 reakcji niezależnych rozkładów celulozy, hemiceluloz oraz ligniny. Ta sama metodyka

posłużyła do rozpoznania mechanizmu kinetyki pirolizy osadów ściekowych - modelu 10 niezależnych reakcji, których przypisanie do rozkładu substancji jest problematyczne z uwagi na złożoność składu samego osadu. Wyznaczone na podstawie otrzymanych parametrów modele kinetyczne pozwoliły przewidzieć zachowanie się próbek biomasy w reaktorze podczas eksperymentów w skali laboratoryjnej.

Thesis organization

Presented doctoral dissertation is organized according to the main research tasks of the National Science Center, Poland, OPUS 12 project "Study on the solar pyrolysis process of the waste biomass" on which the very same thesis is based on. Main chapters of the work reflect research objectives, which were determined by the Supervisor during writing a proposal for OPUS 12 project call, granted at the fall of 2016. The Research Tasks designated for the Ph.D. candidate were constructed as follows:

1. Performing technical, chemical and elemental analysis of analyzed fuels.
2. Building an original research stand will allow to study the influence of the temperature of the solar pyrolysis process of selected species of waste biomass on the composition and yield of process products - liquid fraction (bio-oil), solid fraction (bio-carbon) and gas (pyrolysis gas).
3. Determination of the measurement methodology for the parameters of the kinetics of the waste biomass pyrolysis process.
4. Investigation of energy distribution in the products of the pyrolysis process.
5. Determination of the rate of conversion of the chemical energy of biomass into chemical energy of useful products.

As a result, presented dissertation is organized in 6 main chapters with a comprehensive summary, critically reviewing the whole work. **Chapter 1** *General introduction* is a comprehensive analysis of the current statues of the EU climate and energy policies, renewable energy sector, bioenergy utilization and potential, with a brief characterization of the biomass and waste thermochemical conversion methods. Number of doctoral theses already investigated a problem of biomass conversion field, especially pyrolysis, torrefaction and gasification, so only latest studies, updates and state-of-the-art findings on the solar pyrolysis are presented. **Chapter 2** *Materials used in the study* focuses on Research Task I, as a brief presentation of the investigated feedstock with emphasis on motivation of its choice, energetic potential, fuel properties presentation, and the need of the further study. **Chapter 3** *Design and construction of the solar pyrolysis laboratory reactor* summarizes the entire venture of designing and assembling a reliable bench-scale solar pyrolysis reactor. The Chapter is based on two scientific articles published by S. Sobek and S. Werle in the first years of the Ph.D. in 2018-2019, namely "Solar pyrolysis of waste biomass: Part 1 reactor design", and "Comparative Review of Artificial Light Sources for Solar-Thermal Biomass Conversion Research Applications", published in Renewable Energy (Impact Factor, IF=6.274) and Ecological Chemistry and Engineering S. (IF=1.488) respectively. The chapter summarizes Research Task II, with complex review of the available light sources for solar-thermal research applications, motivation of the reactor

design, geometry and materials, ideas for the collection of the products, and latest data acquisition system and measurements implementation. Within the chapter, all of the necessary information about measurement techniques and further experimental procedures are presented and discussed. **Chapter 4** Thermogravimetric analysis of the feedstock behavior during pyrolysis describes the techniques and methodology of the TGA measurements carried out for the study. Additionally, the importance of reliable TGA data for kinetic computations, and potential errors one might denote are highlighted, all within the International Confederation for Thermal Analysis and Calorimetry (ICTAC) Kinetic Committee recommendations. **Chapter 5** *Kinetic analysis of the solar pyrolysis process of the waste biomass*, focused on Research Task III, presents a novel approach to biomass thermochemical conversion kinetics in general. Proposed methodology implements latest finding within the field of the model-based and model-free, isoconversional kinetics, resulting in a complex kinetic schemes (mechanisms) of the solar pyrolysis of the investigated feedstock. Chapter presents a latest literature review, current state of the knowledge on pyrolysis kinetics, with presentation of the latest techniques, both analytical, and numerical *i.e.*, master-plot method, deconvolution techniques, and kinetic predictions The theory presented within Chapter 5 is based mostly on Sergey Vyazovkin book "Isoconverisonal kinetic of thermally stimulated processes" extended with Ph.D. candidate key-findings from the articles published. **Chapter 6** *Results* presents all of the key-findings of the experimental and kinetic tasks carried out during the Ph.D. study. Kinetic models for the waste straw, wood, and sewage sludge, along with results of the TGA, are presented and methodologies developed for its determination are extensively discussed. Apart from traditional model-based kinetics, original approach to isoconversional rate modelling of the waste biomass pyrolysis, with own-determination of the apparent reaction models profiles specific for each feedstock decomposition. The input for calculation was provided by the isoconversional analysis results for each of the analyzed biomass type. After kinetic computations, the results of experimental campaign of the solar pyrolysis process of the waste biomass are presented. In this part of the thesis, based on Research Tasks IV and V, all the experimental finding are presented, including solar pyrolysis products distribution and quality, denoted pyrolysis heating rates, temperature profiles, pyrolysis gas quality, with high hydrogen content, and correlation of the gaseous compounds formation to the kinetic predictions.

During the Ph.D. study, a Candidate, Szymon Sobek was listed in 14 scientific articles published in high impact factor Journals, with 6 papers as a leading author. According to the Scopus database the total number of citations from 2018 is 78, with the Hirsh index *h-index = 6 (access on February 23t^h, 2021)*. The publications list is given below:

1. Trinh TT, Werle S, Tran K-Q, Magdziarz A, Sobek S, Pogrzeba M. *Energy crops for sustainable phytoremediation – Fuel characterization*. Energy Procedia 2019;158:873–8. https://doi.org/10.1016/j.egypro.2019.01.224.
2. Trinh TT, Werle S, Tran KQ, Magdziarz A, Sobek S, Pogrzeba M. *Energy crops for sustainable phytoremediation - Thermal decomposition kinetics*. Energy Procedia 2019;158:873–8. https://doi.org/10.1016/j.egypro.2019.01.224.

3. Werle S, Sobek S. *Gasification of sewage sludge within a circular economy perspective: a Polish case study*. Environ Sci Pollut Res 2019;26. https://doi.org/10.1007/s11356-019-05897-2.
4. Werle S, Sobek S, Kaczor Z. *Biomass pyrolysis-the predictions of the process behavior based on the chemical structure of fuel*. J Int Sci Publ 2019;13:128–35.
5. **Sobek S**, Werle S. *Solar pyrolysis of waste biomass: Part 1 reactor design*. Renew Energy 2019;143:1939–48. https://doi.org/10.1016/j.renene.2019.06.011.
6. **Sobek S**, Werle S. *Solar pyrolysis of waste biomass: Part 2 kinetic modeling and methodology of the determination of the kinetic parameters for solar pyrolysis of sewage sludge*. Renew Energy 2020. https://doi.org/10.1016/j.renene.2020.02.061.
7. **Sobek S**, Werle S. *Kinetic modelling of waste wood devolatilization during pyrolysis based on thermogravimetric data and solar pyrolysis reactor performance*. Fuel 2020;261:116459. https://doi.org/10.1016/j.fuel.2019.116459.
8. Tran K-Q, Werle S, Trinh TT, Magdziarz A, Sobek S, Pogrzeba M. *Fuel characterization and thermal degradation kinetics of biomass from phytoremediation plants*. Biomass and Bioenergy 2020;134:105469. https://doi.org/https://doi.org/10.1016/j.biombioe.2020.105469.
9. **Sobek S**, Werle S. *Isoconversional determination of the apparent reaction models governing pyrolysis of wood, straw and sewage sludge, with an approach to rate modelling*. Renew Energy 2020;161:972–87. https://doi.org/10.1016/j.renene.2020.07.112.
10. **Sobek S**, Werle S. *Comparative Review of Artificial Light Sources for Solar-Thermal Biomass Conversion Research Applications*. Ecol Chem Eng S 2019;26:443–53. https://doi.org/10.1515/eces-2019-0033.
11. Kaczor Z, Buliński Z, Sobek S, Werle S. *Application of inverse methodology to estimate unknown parameters of the mathematical model of biomass solar pyrolysis*. Renew Energy 2021;163:858–69. https://doi.org/10.1016/j.renene.2020.09.018.
12. Werle S, Dudziak M, Sobek S. *Water solution purification by phenol adsorption on solid fraction from thermal treatment of waste biomass - occurrences of unfavourable phenomenon.* Desalination and Water Treatment 2020;186:72–7. https://doi.org/10.5004/dwt.2020.25113.
13. **Sobek S**, Werle S. *Solar pyrolysis of waste biomass: a comparative study of products distribution, in situ heating behavior with application of model-free kinetic predictions*. Fuel 292; May 15, 2021; https://doi.org/10.1016/j.fuel.2021.120365
14. Wang Z, Wang Q, Yang X, Xia S, Zheng A, Zeng K, Zhao Z, Li H, Sobek S, Werle S. *Comparative assessment of pretreatment options for biomass pyrolysis: linking biomass compositions to resulting pyrolysis behaviors, kinetics and product yields*. Energy & Fuels, February 2, 2021; https://doi.org/10.1021/acs.energyfuels.0c04186.

Table of Contents

Chapters

List of Figures

List of Tables

Nomenclature

Acronyms

CE	circular economy
CFD	computational fluid dynamics
CI	confidence interval
CSP	concentrated solar power
DNI	direct normal irradiation
EC	European Commission
EEA	European Environment Agency
EU	European Union
EUF	energy upgrade factor
EBG	Entrained bed gasifiers
FBG	fixed bed gasifiers
FLBG	fluidized bed gasifiers
GC	gas chromatography
GHG	greenhouse gases
HTC	hydrothermal carbonization
HTL	hydrothermal liquefaction
ICTAC	International Confederation for Thermal Analysis and Calorimetry
IR	infrared
MS	mass spectrometry
MSW	municipal solid waste
MR	mean residual
NDIR	nondispersive infrared sensor
LED	light-emitting diode

Parameters and variables

C	elemental carbon weight fraction (wt.%)
H	elemental hydrogen weight fraction (wt.%)
N	elemental nitrogen weight fraction (wt.%)
O	elemental oxygen weight fraction (wt.%)
T	temperature (°C)
τ	time (s)
p/p_0	relative vapour pressure
BET	Brunauer, Emmett, Teller surface area (m^2/g)
n	number of observations
v	degree of freedom
S^2	sample variance estimate (°C)
s	sample standard deviation estimate (°C)
$t_{\alpha,v}$	t-Student distribution value
g	product share (wt.%)
V	flow rate (m^3/s)
m	mass (kg)
ρ_{gas}	pyrolysis gas density (kg/m^3)
Cp	specific heat capacity (J/kgK)
α	fuel conversion extent (-)
τ^*_α	predicted fuel conversion time (min)
$d\alpha/d\tau$	conversion rate (%/min)
E_α, A_α	isoconversional activation energy (kJ/mol) and pre-exponential factor (min^{-1})

PLC	programmable logic controller	E, A	Arrhenius activation energy (kJ/mol) and pre-exponential factor (min^{-1})
PM	particulate matter	$k(T)$	Arrhenius rate constant (min^{-1})
SCW	supercritical water	$f(\alpha)$	reaction model function (-)
SRF	solid recovered fuel	R	universal gas constant (kJ/mol K)
SS	sewage sludge	$T(\tau)$	thermoanalytical temperature program
RDF	refuse derived fuel	β	linear heating rate (K/min)
RES	renewable energy sources	$dT/d\tau$	actual heating rate (K/min)
WS	waste straw	SST	ash shrinkage temperature (°C)
WW	waste wood	DT	ash deformation temperature (°C)
WWTP	waste water treatment plant		
QTH	quartz-tungsten halogen	*Superscripts*	
TGA	thermogravimetric analysis	$^{diff.}$	calculated by difference
c	cellulose	$^{a.r.}$	as received
h	hemicellulose	^{d}	dry
l	lignin	*	kinetic prediction value
Q_r	heat of the reaction (J/mol)		
H	enthalpy (J)	*Subscripts*	
ΔH^{θ}	standard enthalpy of formation (J/kg)	$_{in}$	value at the reactor inlet
M	moisture	$_{out}$	value at the reactor outlet
VM	volatile matter	$_{0}$	initial value of the parameter
VL	visible light	$_{f}$	final value of the parameter
FC	fixed carbon	$_{gas}$	pyrolysis gas
AC	ash content	$_{oil}$	bio-oil
HHV	higher heating value (MJ/kg)	$_{char}$	char
LHV	lower heating value (MJ/kg)	$_{feed}$	feedstock

1. General introduction

1.1. Background

In 2016, despite being continuously diminished by the rising growth rate of modern renewables, nearly 80% of the world's total energy consumption was still provided by fossil fuels. The increase in renewable energy deployment continued in 2017, especially in the power sector, owing to factors such as: improved access to financing, global concerns about energy security, human health and the environment, growing energy demand in young and developing economies, urgent need for emission-free electric energy, clean cooking facilities, and dedicated policy initiatives and support for ambitious targets [1]. With continuous economic and social growth, the global energy demand is rising while available fossil fuels resources are slowly approaching exhaustion. In 2014, the world's primary energy demand was estimated at 13 000 megatons of oil equivalents (1 Mtoe = 41,868 GJ), representing an increase of 22% and 54%, compared to 2004 and 1994, respectively [2]. This rapidly-rising energy demand has begun the alarmingly intensive exploitation of natural environments in the search for new renewable energy sources. Greenhouse gasses (GHG) comprise more than 80% of global anthropogenic emissions, so decisive action in the energy sector is needed to mitigate the effects of global warming [3].

1.1.1. Current status of the EU Climate and Energy

The European Green Deal for the European Union (EU) sets a new course, addressing climate and environmental-related challenges for the future years. A new growth strategy aims to " transform EU into a fair and prosperous society, with a modern, resource-efficient and competitive economy with zero-net emissions of greenhouse gases in 2050, and where economic growth is decoupled from resource use" [4]. Expectations for efficient and sustainable waste-derivatives and biomass conversion are growing every year. Worldwide biomass and waste potential is considered as a possible solution for the future problems related to the depletion of fossil fuel reserves and corresponding environmental problems [5–8]. The EU policy framework for climate and energy in the period from 2020 to 2030 sets a goal for at least 40% cuts in greenhouse gas emissions (GHG) in reference to

1990, at least 32% share of renewable energy share in final energy consumption with 32.5% increase in overall energy efficiency [9]. Therefore, the development of waste-to-energy scenarios needs to be focused on searching for alternative fuels for effective thermochemical conversion based on locally available Renewable Energy Sources (RES), minimizing negative carbon footprint impact.

In recent years, researchers and power engineers attention was drawn to Municipal Solid Waste (MSW) due to its availability, its alarming growth rate and energy potential [10–12]. However, the feedstock turned out to be problematic in energy handling, especially due to its heterogeneity, inconsistent fuel properties and a lack of uniform thermal behavior [13,14]. One method of overcoming this problem involves converting MSW to refuse-derived fuel (RDF), which became more competitive comparing its combustion behavior to fossil fuels in terms of energy production [15,16], and even increased it plastic, textile and non-recyclable waste potential for gasification [17–19] and pyrolysis [20–22]. RDF is a promising fuel, however, without efficient household waste sorting implementation costs are too high to compete with already used fossils. A different approach to alternative fuels is available, with recognition of the local biomass and waste biomass potential. In Poland one of the biomass key-suppliers are agriculture, wood industry and municipal economies. A variety of locally available biomass and waste with huge energetic potential sets a need for experimental studies for specific feedstock conversion to recognize its potential first. With specification of the desirable conversion routes and supply chains, efficient and universal kinetic methodologies able to evaluate different types of processes based on the lowest use of thermoanalytical measurement techniques and savings in computational effort must be considered.

1.1.2. Biomass as a source of renewable energy

One of the most promising renewable energy sources in terms of energetic potential and availability for Poland is biomass. According to the European Environment Agency (EEA), the biomass potential in Europe is estimated at 225 Mtoe per year from key suppliers, such as agriculture, wood industries, and municipal economies [7]. In Poland, the annual biomass energy potential is equal to >20 million Mg of waste straw, approx. 4 million Mg of waste wood, and approx. 6 million Mg of sewage sludge [8]. Having in mind the Green Deal agreement and goals associated with carbon-neutrality until 2050, a straight forward combustion of biomass must be reconsidered. Apart from biomass energy utilization for heat, a number of alternative conversion routes is available e.g., pyrolysis, hydrothermal liquefaction, aimed for sustainable bio-carbon materials, chemicals, and bio-active compounds production.

1.1.3. Bioenergy utilization

A very large number of biomass species has been and still is considered as a renewable energy source. These are divided into several conventional groups, depending on crop type, and on the type of the fuel which it is to be converted into, classified in 1996 by Mørten G. Grønli [23]:

- The first group – perennial lignocellulosic plants, mainly woody species, both long term (15-50 year rotation) and short term (6-15 year rotation), multiple stem coppicing of perennial crops. Willow and poplar are the two species that were considered for energy production in northern and temperate zones of Europe at the end of the XX century.
- The second group – herbaceous annual crops, including *Miscanthus* and sweet sorghum, still with considerable interest as a waste renewable energy source from phytoremediation process of the contaminated soils [24].
- The third group – high sugar/starch crops, mainly used for bioethanol production in some countries *e.g.*, Brazil. Examples are sugar-cane, maize, and sugar beet, couples with a large number of conventional food crops *e.g.*, wheat.
- The fourth group – oil-containing crops such as rape and sunflower, from which vegetable oil can be extracted and further processed into bio-diesel.

Beside those four conventional groups, a number of more unconventional sources can be distinguished, especially interesting with implementation of the Circular Economy concept. Circular Economy idea aims for low carbon footprint, local economy, where resources are supplied from local industries, both products and wastes:

- Residues from conventional forestry and wood industry, comprising branches, sawdust, planner shavings and off-cuts, generally understood as a waste wood and its derivatives.
- Solid agricultural residues, mainly straw from cereal crop, a waste straw.
- Municipal and industrial solid wastes and products of the waste water treatment plants *i.e.*, sewage sludge.
- Residues from brewing industry *i.e.*, spent grain, highly moist and rich in lignocelluloses, currently utilized as a feed for livestock.
- Refuse derived fuel (RDF) is produced from domestic and business waste, which includes biodegradable material as well as plastics. Non-combustible materials such as glass and metals are removed, and the residual material is then shredded. Refuse derived fuel is used to generate energy at recovery facilities, many of them in Europe where they produce electricity and hot water for communal heating systems.

- Solid recovered fuel (SRF) is a standardized (PN-EN 15357:2011 for Polish scenario) alternative to fossil fuel and is produced from mainly commercial waste including paper, sludge, card, wood, textiles and plastic, with criteria of the higher heating value (HHV) > 6 MJ/kg of the dry mass.

Presented resource base is highly diverse in terms of its availability and its physical and chemical properties. In comparison to fossil fuels, biomass and waste has usually lower energy content, higher moisture and different ash composition, usually harmful for industrial boilers. In general, without processing and segregations, the physical form of biomass and waste is highly heterogenous, causing substantial problems and difficulties in use applications without modification of the feed supply line, dryers and milling systems. However, technologies for converting biomass into more convenient energy forms, namely liquid and gaseous fuels, as well as upgraded solid, can be introduced to adapt the fuel to a specific end use. Three principle classes of conversion processes which can be used for biomass and waste upgrade: biochemical via microbiological action (for organic, non-lignocellulosic matter), thermochemical via heat treatment under different atmospheres, and physicochemical processing.

1.1.4. Thermochemical conversion of biomass

Conversion via thermal methods is still one of the most popular ways to release the energetic potential of biomass. In years 2005-2015, co-firing biomass with coal in industrial power plants has been quite successful in the case of fulfilling the share of renewable energy in total production, and reaching appropriate emission gauges for industry. However, despite the renewability of biomass, when combusted, it releases significant amounts of greenhouse gases (GHG), particulate matter (PM), and its alkaline nature causes devastating corrosion on low-temperature exhaust gas sequences. Recently released national legislations have limited the support for co-firing and have identified operational problems caused by adding biomass to industrial boilers, originally fueled with coal and have shown that further co-firing must be reconsidered. However, there are thermal conversion methods which not only generate reduced emissions, but also provide high biomass energy conversion rates, as well as an overall biomass energetic competitiveness upgrade.

The general goal of biomass thermal conversion methods is to produce renewable fuels from low calorific, waste organic matter. The conversion can be proceeded in several ways, where the most popular are: gasification, pyrolysis, hydrothermal carbonization (HTC) and liquefaction (HTL), and torrefaction. Potential application of the mentioned processes based solar-heat implementation opens up the possibilities of storing solar energy in the form of usable chemical energy of post-process products, without any GHG released,

due to emission-free nature of the concentrated solar power (CSP) and significantly lowers the heat acquisition cost [25].

Carbonization

Carbonization is probably the oldest method of biomass conversion known to human kind. The process is thousands of years old and it's based on the very slow decomposition of woody biomass under partially inert atmosphere at temperature approx. 300-600 °C in piles or retort furnaces. Carbonization characterizes itself by significant release of volatiles from biomass. The main purpose of the process is minimization of hydrocarbon content with maximization of fixed carbon, thus the heating value and energy density.

Gasification

The gasification process is the partial oxidation of the biodegradable material in an oxidant-restricted atmosphere. The gasification reactors *i.e.*, gasifiers, can be divided into three main types [26]: fixed bed (FBG), fluidized bed (FLBG), and entrained bed gasifiers (EBG). The aim of the gasification process is conversion of solid fuel into a combustible gas by thermal treating of the feed in a generator with gasification agent, being usually air, or steam [27,28]. The heating value of the gasification gas, being the mixture of CO, H_2, and lower hydrocarbons, varies around a value of 4 MJ/m^3 [26]. Gasification of the solid feedstock results also with generation of the solid fraction, being a carbon rich, ash-like residue [29]. Gasification gas is commonly used as a fuel, not rarely for local energy purposes where abundant waste material can be found e.g., municipal economies or farms. It can be utilized in mechanical or electrical power generation processes. Sometimes it can be utilized as a second fuel in diesel engines working in "dual fuel" operations [30]. The main advantage of gasification process, justifying it's wide applications is the maturity of the process and the following technologies, with numerous successful studies and applications, even during the World War II theater.

Pyrolysis

Undoubtedly, less mature process in terms of basic studies, and non-less attractive considering potential applications is the pyrolysis. Pyrolysis is thermal degradation of carbonaceous material in oxygen-free atmosphere [31–34]. During the pyrolysis three useable products are always produced *i.e.*, bio-oil, pyrolysis gas, and carbon-rich, highly porous solid residue, called the bio-char, so all the initial energy is converted into useful chemical energy of the products. Numerous pyrolysis studies proved that pyrolysis process parameters, like temperature and heating rate, dictate the final product yields [32,35]. Generally the lower the energy supply, the higher the solid fraction yield with the lowest decomposition rates. The higher the temperatures and especially heating rates, first the more liquid and eventually gaseous fraction yields are denoted [2]. It is uncommon to distinguish

pyrolysis as a biomass pre-treatment method. Pyrolysis rarely is orientated for upgraded biomass char *i.e., biochar*, yields, much more often the tendency to a more valuable oil and gas production is observed. Due to the high temperatures of the process and the isolated, inert reaction zone, pyrolysis is a suitable and safe method for the conversion of toxic and contaminated biomass *e.g.*, crops collected after phytoremediation of contaminated soils, or municipal sewage sludge, where the toxins are utilized and decomposed, and heavy metals which are trapped in the solid residue of the pyrolysis process [36]. The conventional implementation of all of the listed methods requires a significant amount of heat to carry out the reaction, which is usually obtained from burning fossil fuels, which indirectly generates GHG emissions, thus diminishing the pro-ecological effect of the entire process. The idea of a solar-driven pyrolysis process is a promising way to produce environmentally- clean renewable energy from low-calorific biomass. Not only does it reduce the cost of necessary heat, but it also significantly reduces GHG emissions and provides a novel storage method of solar energy in the form of stable pyrolysis products.

Torrefaction

Torrefaction is low-temperature thermochemical conversion under inert conditions, which aims for biomass pre-treatment (upgrade) [37–39]. Low temperatures and heating rates prevents feedstock from intense decomposition in order to achieve dry, stable, more homogenous and hydrophobic solid torrefied fuel [40,41]. The main clue why torrefaction is separated from traditional pyrolysis is the process destination and it's ideology. While pyrolysis goal is to release the most of energy from biomass, the aim of torrefaction is to keep, upgrade and expose its energetic potential [42]. Temperature ranges to carry out the process are lower than in the case of carbonization, approx. 200-300 °C. High energy density post-process product shows much greater behavior during milling and energy handling, thus it's application for industrial boilers is viable. Torrefied pellets obtained from biomass with lower heating value varying from 16-29 MJ/kg are competitive candidate for coal replacement. It is plausible, that biomass torrefaction has great application potential in many energy sectors *i.e.*, heating sector, power generation (co- iring) or for gasification and steel production (reducing agent), the only issue is a still high net fuel production cost.

Hydrothermal carbonization (HTC) and liquefaction (HTL)

Widely understood hydrothermal treatment (HT) is considered as a promising method for organic waste and biomass upgrade method. The main advantage of the HT is the ability to directly treat wet feedstock, since medium of the reaction is liquid water. The HT is especially promising for the most abundant lignin conversion, showing potential for solid, carbonic rich second-generation solid fuel, as well as valuable aromatics and phenolics, with numerous successful experimental studies reported so far. Two main routes

of the HT are carried out: HTC and HTL. HTC is a thermochemical process to convert wet biomass into a coal-like material, called hydrochar; and a liquid, rich in organic acids (acetic, formic, levulinic, or lactic acid). HTC occurs in the aqueous phase in a closed reactor at long residence time (1–12 h) and temperatures corresponding to autohydrolysis (150–260 °C). Over the years numerous studies investigated HTC biomass processing, providing insight into solid product quality, yields, and its correlation to the experimental conditions [43]. Comparing the HTC process to a more traditional dry-torrefaction, also producing carbonized, high-energy-density solid, hydrothermal processing seems already to provide some advantages *e.g.*, ability to omit (or save) latent heat supply, lower devolatilization at comparable temperatures, enhanced ash removal, or relatively shorter reaction times due to higher general reactivity of liquid phase [40].

The second route, HTL takes place at higher temperatures and heating rates, leading a process into more liquid-rich product yields regimes. HTL also refers to as hydrous pyrolysis, is a thermochemical depolymerization process in an enclosed reactor to convert wet biomass into biocrude oil and chemicals at moderate temperature, 300–400°C, and high pressure typically 10–25 MPa [44]. Protein-containing feedstock such as food processing waste, manure, and municipal sludge typically having high moisture content, makes HTL an appropriate process for its conversion for further energy, or chemical industry purposes.

Sub-critical water plays a crucial role during HT, acting both as a reaction catalyst and as a solvent, with a significant shift of its polarity due to a drastic decrease of dielectric constant, comparing to water at standard conditions [45,46]. To illustrate, water at 25 °C and 0.1 MPa has a dielectric constant of 78, being a polar solvent not suitable for organic compounds, which most is non-polar. However, in the region near the critical point (374 °C, 22.1 MPa) water acts as a non-polar solvent, being an extremely effective reaction medium for organics, thanks to the new properties, similar to *e.g.*, methanol, acetone, or even methylene chloride, with the increase of the temperature at a hot compressed liquid state. This change in the density correlates with other properties of water such as solvation power, degree of hydrogen bonding, polarity, dielectric strength, molecular diffusivity, and a viscosity [47]. Another property of hot compressed water is its ion product, presenting a maximum at around 250 °C under saturation vapor pressure. Interestingly, a sharp drop in the water ionization products (H_3O^+, OH^-) occurs when exceeding the critical point. Overall, depending on the temperature and pressure hydrothermal media may support either ionic or free radical reactions. At high densities below the critical temperature or in supercritical water at very high pressures, ionic reactions dominate. At high temperatures and low densities, free-radical reactions are superior. Higher temperature reactions reduce char formation, producing more oil or a biocrude, but simultaneous free radicals promote the formation of coke. On the other hand, the solubility of inorganic compounds, mostly polar, in ambient and hot compressed water is completely different from organics. The solubility of inorganic compounds is very high in ambient water, but almost none in

subcritical conditions. All these phenomena must be taken into account, as a one of the main challenges during the design of the efficient fast HTL system [47].

1.2. Solar pyrolysis

1.2.1. Solar energy potential

Considering renewable energy sources such as solar energy, wind energy, geothermal, biomass, and hydropower, the crucial parameters that determine implementation of an energy source are its availability and acquisition cost. Solar energy could be a promising option for the future world because of several reasons. First, solar energy is the most abundant renewable energy source, $1.8 \cdot 10^{14}$ kW is intercepted by the earth. Second, it's completely and sun emits $3.8 \cdot 10^{23}$ kW of energy, of which approximately free and environmentally-clean. Third, there are plenty of efficient solar energy acquisition methods with parabolic-trough collectors, point-focus parabolic dish concentrators, and Fresnel lenses, with numerous reports on successful implementation of these technologies for biomass thermochemical conversion [48–50].

1.2.2. Complexity of the pyrolysis process

Pyrolysis process consists of many simultaneous reactions, such as dehydration, decarboxylation, charring, vapor formation, as well as secondary cracking and repolymerization reactions, that along with and mass transfer phenomena. Complexity of pyrolysis complicate the determination of consistent and universal process mechanism or definition. Despite the difficulties, pyrolysis can be divided into several steps. Drying occurs as soon as external heat is applied, and when moisture is released, the initial decomposition takes places through the release of volatiles. During the first stage of pyrolysis, which occurs between 100 °C and 250 °C, some internal structural rearrangements occur, such as chemical bond breakages and the formation of carbonyl groups. Primary pyrolysis starts after reaching 250 °C and ends depending on the feedstock type, at approximately 450-500 °C, which results in the largest mass loss and the release of primary condensable and non-condensable volatiles. The solid residue of the pyrolysis reaction, char, is continually generated during the process [13]. Pyrolysis, apart from implementation as a sustainable method for biomass and waste conversion, is a substantial component of combustion and gasification process. What's more, recognition of pyrolysis mechanism can give valuable insight into phenomenon of wildfire spread for preventing and emergency life-saving purposes.

1.2.3. Pyrolysis products

As it was already mentioned, the pyrolysis of any carbonaceous feedstock generates three usable products *i.e.*, condensable tars called bio-oil, dry pyrolytic gas, and solid carbon-rich, coke-like residue – the char. Bio-oil is a mixture of mainly oxygenated and nitrogenated high molecular weight aromatic compounds, such as phenols, ketones, alcohols, amides, and nitriles, among others [5]. Recent reports have focused on bioactive compound production from liquid products of biomass thermal conversion i.e., bio-replacements of synthetic substances used in the chemical industry [6] or pharmacy and healthcare [7]. Numerous studies have already described compositions of various bio-oil samples from different feedstock pyrolysis processes using gas chromatography (GC) and gas chromatography mass spectrometry techniques (GC-MS) [8]. In 2020, D. Chen et al. [9] presented bio-oil composition from solar pyrolysis with over 50% valuable phenols content, <30% acids, 30 and <20% furans, from three types of biomass originally pre-treated with aqueous phase bio-oil instead of traditional acid washing. Pyrolytic gas is a mixture of low-molecular-weight gaseous species *i.e.*, CO, CO_2, CH_4, H_2, and lower hydrocarbons, which are relatively easy to detect via infrared (IR) spectra absorption in gas analyzers with Nondispersive Infrared Sensor (NDIR). The char collected after pyrolysis is a carbon-rich, highly porous coke-like residue, with numerous potential applications such as filtering materials, adsorbents, activated carbon source, and sustainable fossil fuel replacement for combustion [10]. Recently, coal based poly-generation technology has been shown to produce electricity, synthetic fuels, and chemical products, and is regarded as a promising alternative for fossil fuels i.e., lignite, utilization with low CO_2 emissions. In this system, coal is firstly fed into a pyrolyzer (550-750 °C), where the autothermic system is executed using heat provided by the combustion from pyrolysis of char, as a fossil solid fuel alternative [11]. Moreover, N. Gao et al. [12] critically reviewed thermochemical conversion methods of SS, and stated that pyrolysis is advantageous for the decomposition of organic pollutants, neutralization of pathogens, and reduction of the volume of the waste. The actual properties of the pyrolysis products i.e., calorific values of gas and char, bio-oil composition, or product yields, are highly dependent on pyrolysis heating conditions, and final particle residence times. Feedstock type, particle size, and even bed type play a crucial role in pyrolysis process, which is supported by A. Mlonka-Mędrala et al. [13]. Usually, the lower the heating rates and process temperatures over time, the more char will be obtained in the final products due to minimal devolatilization and decomposition of the carbon structures of the feed. As heating rates and temperatures increase, enhancement of devolatilization is observed, with two main fractions releasing condensable vapors forming the bio-oil and non-condensable pyrolytic gas, where secondary and even tertiary reactions may occur.

1.2.4. The "speed" of the pyrolysis: main process technologies

Over the years, pyrolysis has been categorized in one of three ways: slow, fast (sometimes called intermediate or medium), and flash [2]. The differentiation between these categories is based on the heating rates at which the reacting feedstock is heated, and the resulting product yields and process temperatures. As previously stated, slow pyrolysis mainly generates highly carbonized char with somewhat equal shares of the rest of the products, while fast pyrolysis with heating rates do not exceed 200 K/s and temperatures 400-600 °C, possessing superiors release of bio-oil vapors, yielding more liquid products. In flash pyrolysis, the most severe heating rates with thousands of *Kelvins per second* cause immediate cleavage of chemical bonds in the feedstock, in which devolatilization is followed by instant thermal cracking of almost any vapors to lower weight molecules. During 58 flash pyrolysis mainly H_2 and CH_4 are produced, yielding the highest gas shares in the products, with almost no solid residue left after the process [15].

Table 1: Pyrolysis technologies classification.

Pyrolysis technology	*Process conditions*			*Product yields*		
	Heating rate, β	Process time, τ	Temperature, T	Solid	Liquid	Gas
Slow	< 50 $K \cdot min^{-1}$	5-30 min	400-600 °C	<35 %	<30 %	<40 %
Fast	10-200 $K \cdot s^{-1}$	< 5 s	400-600 °C	<25 %	<75 %	<20 %
Flash	~1 000 $K \cdot s^{-1}$	< 0.1 s	600-900 °C	<20 %	<20 %	<70 %

Table 1 lists the ranges of key-parameters of major pyrolysis technologies at which the specification is based on. Slow pyrolysis, with the lowest heating rates, and thus the longest reaction times, results in a relatively uniform product distribution, with a slight skew towards higher char yields [32]. Longer reaction times favours char formation and secondary tar-cracking reactions, increasing the final solid yield and secondary-gas formation. Generally, the lower the heating rate and the longer the biomass exposure time during heating, the higher the yield of final solid products.

Fast pyrolysis, despite having the same temperature range as slow pyrolysis, is gaining attention in bio fuels and chemical production, due its high liquid yields. The main reason for the latter is the short reaction time, which is too short to cause char formation due to the high amount of heat supplied with heating rates reaching up to 200 K/s. The high amount of heat supplied meets the endothermal requirements to form condensable vapours, which when combined with the short vapours residence time and rapid cooling, maximizes the final liquid yield [2].

Flash pyrolysis, which has the most intensive heating rates, also has the highest temperatures and shortest reaction times, typically less than 1 s [51]. In this method, concentrated radiation is directly focused on a biomass sample which causes almost instant decomposition, and incident heat fluxes at the reaction zone are often higher than 7 MW/m^2. At higher temperatures, primary vapour secondary reactions are more likely to happen, which leads to higher gas production (up to 75%) than in fast pyrolysis [52].

1.2.5. Pyrolysis energy balance and problems with heat of reaction determination

The evaluation of heat of pyrolysis through the simple energy balance allows for a rough estimation of the heat necessary to perform the pyrolysis process. The energy balance of the pyrolysis takes into consideration the difference between the total enthalpies of the pyrolysis products and the feedstock [53,54].

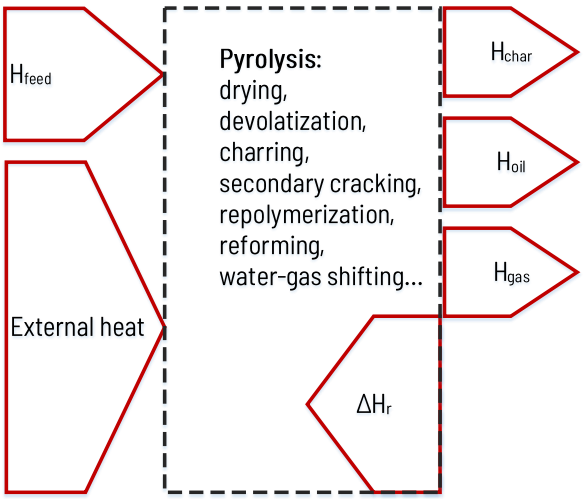

Fig. 1.1. Adiabatic scheme of energy balance for a pyrolytic reactor.

Fig. 1.1 presents a simple scheme of the energy balance for an adiabatic pyrolysis reaction zone, further described with the Eq. (1.1). When considering only a thermodynamic energy balance, the endothermic character of pyrolysis can be explained through the heat of reaction, Q_r, defined as Eq. (1.2) being the simplified sum of the chemical heat of the reaction, ΔH_r, and physical enthalpy of the reactants heating to a destined process temperature.

When applying the first law of thermodynamics to the pyrolysis reaction, a significant difference can be denoted between the total enthalpies of reagents and the products. H. Yang et al. 2013 [53] proposed the energy balance for a pyrolysis reaction that was defined as the difference between the sums of enthalpies of products and the enthalpy of the feedstock biomass, Eq. (1.3).

$$Ext.Heat + H_{feed} = -\Delta Hr + H_{oil} + H_{gas} + H_{char} \tag{1.1}$$

$$Q_r = Ext.heat + \Delta H_r \tag{1.2}$$

$$Q_r = H_{gas}\Big|_{T_{out}} + H_{oil}\Big|_{T_{out}} + H_{char}\Big|_{T_{out}} - H_{feed}\Big|_{T_{in}} \tag{1.3}$$

The specific enthalpy of the *i-th* reactant is calculated as a sum of the standard enthalpy of formation and the physical enthalpy increase between the initial and outlet temperature.

$$H_j = m_j\left(\Delta H_i^{\phi} + \int_{T_1}^{T_2} Cp_j dT\right) \tag{1.4}$$

The specific enthalpy of each of the reactants is defined as a sum of the increase in physical enthalpy from standard parameters to a desirable process temperature and the specific standard enthalpy of formation. Most of the necessary data needed to evaluate the heat of pyrolysis reaction can be found in engineering databases *e.g.*, EES. In fact, the energy balance method requires previous experimental results that measure product yields and compositions to estimate product enthalpies properly in Eq. (1.4).

1.2.6. Enthalpy of the biomass, pyrolysis gas, and char

The calculation of enthalpy for gas and char is relatively simple. The enthalpy of a pyrolytic gas is defined as the weighted (or molar, depending on the balance reference) average of all the physical and standard formation enthalpies of the components in Eq. (1.4). To evaluate char enthalpies, numerous empirical formulas allow *Cp* and the heat of formation to be estimated based on the process temperatures, which resulted in a HHV.
The feedstock enthalpy is calculated based on the biomass elemental composition and a simple conversion of heat of combustion to heat of formation [55].

1.2.7. Enthalpy of pyrolytic oil (bio-oil)

An estimation of the pyrolytic oil enthalpy using the same method as presented is quite problematic due to numerous organic compounds and simultaneous secondary reactions that occur between them. Yang et al. 2013 [53] presented a method to estimate the empirical pyrolytic oil enthalpy. The two equations proposed in his work allows an estimation of the standard enthalpy of formation, as well as the difference of the physical enthalpy between 25 °C and a desirable process temperature. The two formulas are only based on the total *C*, *H*, and *O* content of crude bio-oil, when the *N* and *S* contents are lower than 0.5 and 0.1 wt.% respectively. Otherwise, using a simple energy balance that involves making many assumptions may cause significant errors in computations, making the entire process balancing worthless.

Pyrolysis heat of reaction denoted in recent studies

Based on experiments, researchers have noted that during pyrolysis, both exothermic and endothermic reactions occur [56]. The final nature of the pyrolysis reaction depends on the competition between parallel formation reactions of different products: endothermal volatiles release and exothermal char formation.

In J. Rath et al. study [54], an experiment to determine the heat of pyrolysis for spruce wood was carried out at 550 °C, with a heating rate of 10 K/min and showed that the heat of pyrolysis varied from 2.4 to 3.4 MJ/kg with an 18-21% char yield. H. Yang et al. [53] estimated the heat of pyrolysis of cedar chips at varied heating rates, from 32 to 320 K/min, to be 1.1-1.2 MJ/kg and 1.3-1.6 MJ/kg for process temperatures between 500 and 550 °C, respectively, with a char yield of 38-48 wt.%. M. Stenseng et al. [57] measured the heat of pyrolysis reaction for *Avicel* cellulose to be 0.63–0.71 MJ/kg for samples of 2 and 5 mg, and about 0.560 MJ/kg for samples of 10 and 20 mg. Again, the difference could be partially explained by the differences in char yield. As mentioned before, the heat of pyrolysis is a simplification of the bound energy that needs to be overcome to initiate a reaction. An approximation of the nature of pyrolysis with a simple energy balance is an oversimplification. Eq. (1.1) is a rough estimation of the heat of the pyrolysis reaction that could be generally used for a comparative evaluation of an energy supply for a different type of feedstock. To more accurately calculate the energy supply for a reaction, a kinetic analysis is necessary, and the heat of pyrolysis is one of the parameters used in kinetic computations *e.g.*, temperature correction factors [58].

1.3. Literature review of the latest solar pyrolysis studies

According to the literature, solar pyrolysis has emerged as a mature topic among the scientific community, with a number of comprehensive studies and review papers already published. Various reports have described the impact of heating conditions, reactor

types, and solar heat acquisition performance on the overall solar-driven biomass conversion efficiency through product characterization and thermodynamic balance equations [59]. K. Zeng et al. showed a series of complex solar pyrolysis studies, as well as a review paper [2], addressing the majority of process key-aspects and challenges. The latest solar pyrolysis review published by M.C. Ndukwu [60] addresses the benefits of solar pyrolysis of biomass, summarizing available optical concentrating devices and conceptual heating modes, the existing configuration of solar-thermal and reactor orientations, highlighting solar pyrolysis availability and potential for technology application within the nearest future. In the most recent study from 2020 [61], K. Zeng et al. focused on solid products characterization obtained from heavy metal contaminated biomass. Immobilization of contaminants inside the char particles was confirmed, and a significant increase of char Brunauer-Emmett-Teller (BET) area from 5.3 to 161.0 m^2/g for temperatures of 600-1000 °C and fast heating rates of 50 K/s was shown. Final char shares were between 22-27 wt.%, and high pyrolysis temperature resulted in reduced porosity due to plastic deformation of carbon structures. The other study published by the same group presented solar pyrolysis experiments of beech wood under temperatures 900-2000 °C and fast heating rates 10-50 K/s, as well as investigation of Computational Fluid Dynamics (CFD) modelling. The study proposed a pyrolysis process kinetic scheme and validation of numerical modelling with experimental data obtained using 2 kW vertical solar furnace setup. It was revealed that at higher temperature and heating rate, higher gas yield was obtained [62]. The emphasis of intra-particle tar secondary reaction into gas for pyrolysis of a large sized sample under severe heating conditions was highlighted. In the case of sample size and intra-particle reactions, J. Soria et al. [63] presented an excellent study on biomass pellets size impact on solar pyrolysis gas quality. They showed that large biomass particles may provide sufficient residence time for tar to decompose both homogeneously and heterogeneously inside a porous structures, producing secondary gas, tar, and char. Furthermore, due to biomass low thermal diffusivity it may lead to thermal gradients inside the particle during pyrolysis. This influences intra-particle heat transfer mechanism and tar secondary reactions, which combined with particle size, plays an important role in product distribution from pyrolysis. A. Ayala-Cortés et al. [64] investigated the impact of solar pyrolysis operating parameters on various characteristics of carbon materials *e.g.*, specific surface area, capacitance or conductivity. The experimental results indicated that solar pyrolysis temperature (500-900 °C) and heating rate (4-30 K/min) had insignificant effect on carbon composition, which were in contrast to structure, surface area, and electrochemical response. This reported revealed a well-designed concept of 5 K-type thermocouples temperature measurement of alumina crucible containing the biomass, but with limited information about the biomass behavior during pyrolysis. L. Arribas et al. [65] reported solar-driven pyrolysis and gasification of different waste feedstock types *i.e.*, micro-algae, wheat straw, and sewage sludge, and examined the processes of gases generated by different feed type, however, no additional details were given regarding other

products. The experimental setup consisted of a solar-simulator, 7 kW xenon lamp, and fixed bed reactor. The highest gas yields were obtained for straw with very high hydrogen content in each type of gas produced (30-45 vol.%), in which the particles were heated to 800 °C with an average heating rate of 3.5-4.0 K/s. K. Zeng et al. [31] focused on precise recognition of all solar pyrolysis products, *solar-fuels*, obtained from beechwood treated at temperatures 600-2000 °C and heating rate 50 K/s. The report examined the influence of temperature on product shares. The liquid products were precisely analyzed using GC-MS and up to 75 different chemical species were detected across studied temperature range, proving the immensely complex nature of bio-oil. All products chemical energy content was characterized, and compared to raw biomass lower heating value (LHV) gave 38-53% energy upgrade factor. A.H. Rony also presented an extensive study of artificial solar pyrolysis [66], where a novel pyrolysis process mechanism was proposed. It showed that bio-oil obtained from solar pyrolysis of pinewood could be separated into useful fuels and chemicals, while focused solar light improved phenolic compound production. Solar pyrolysis technology was found to be applicable for renewable fuels production, as well as self-activated bio-derived carbons used also for electronics. D. Lobato-Peralta [67] et al. investigated solar pyrolysis of abundant waste biomass solar pyrolysis for bio-derived carbons, and described that properties of obtained products could be utilized in supercapacitor technology.

1.3.1. Solar pyrolysis reactor technologies

Solar pyrolytic reactors can be divided into two categories based on the adapted light source: natural and artificial. This work is focusing on solar pyrolysis powered by artificial light sources. Artificial reactors adapt artificial light sources to simulate solar radiation, which then is directed through a concentrator on a target area. Light sources include solar simulators adapted from photovoltaic testing units, where the lamp radiation simulates natural solar radiation with uniformity, power, and spectral match.

Solar pyrolytic reactors powered by natural sunlight

There have been a number of recently-published studies on solar pyrolysis where the experimental section was powered by natural sunlight. In one study, Zeng, et al. 2017 [31,62] investigated solar pyrolysis on a vertical solar furnace, and their device was constructed at CNRS, France, and allowed them to control the plateau temperature and heating rate using a dedicated shutter. In this device, solar radiation was first directed to a parabolic mirror by a movable heliostat and then focused on the reactor surface. In the presented study, the summary areas of the collector and concentrator were significantly higher than the surface of the reactor. The presented experimental rig collected 1.5 kW of solar thermal power with a heat flux density of 12 MW/m^2, operating at 1,000 W·m^2 direct normal irradiation (DNI). The biomass sample reached temperatures up to 2 000 °C, which

classifies the experiment as flash pyrolysis. Zeng's study investigated the product yields at four final temperatures: 600, 900, 1 200, and 2 000 °C. These experiments showed that as the pyrolysis temperature increased, the bio-oil and bio-char yields decreased, for higher yields of pyrolytic gas.

S. Morales et al. 2014 [68] designed a parabolic-trough solar reactor for bio-oil production via orange peel pyrolysis. The presented design was a combination of a radiation concentrator with a thermochemical conversion system, whose final performance was evaluated by a Monte Carlo ray-tracing method. The tubular, glass reactor was placed in a focal line of a parabolic trough solar concentrator, reaching average temperature of 290 °C, with a peak temperature of 465 °C, along with an average and peak heat flux of 12,553 W/m^2 and 27 088 W/m^2, respectively. Experiments were carried out at 965 W/m^2 DNI. Morales' work highlighted a potential problem for industrial application of solar pyrolysis. A 79 wt.% biomass sample was converted to 77.64 wt.% liquid, 20.93 wt.% char, and 1.43 wt.% gas. This study showed that the operating temperature of a highly-transparent parabolic-trough reactor significantly drops as the reactor's length increases. A second problem was heat loss from high biomass reflectance.

The study by H. Grassman et al 2015 [69] addressed the solar pyrolysis of agro-waste biomass using Linear Mirror II. The constructed reactor reached operating temperatures of 350-500 °C after approximately 90 minutes, gathering up to 50 kWh of solar energy. The retort pyrolytic reactor was filled with 5 kg of straw and exposed to the concentrated solar radiation. The authors focused on solar bio-char production, whose yields were investigated as a function of temperature at 300, 400, and 500 °C. The experiment resulted in solid residual mass yields of 51.5%, 39.6%, and 31.2% with bio-coal HHV of 22.6, 27.5, and 28.5 $MJ \cdot kg^{-1}$, respectively.

Another study by M. Sánchez, et al. 2017 [49] focused on the precise evaluation of ideal operating parameters of a pyrolytic reactor for maximized char production. The proposed computational model integrated pyrolysis kinetics, sun-earth geometry relations, and solar-thermal performance calculations. Using this model and Linear Fresnel Technology for solar radiation concentration, the authors predicted the ideal parameters to be a temperature of 308 °C and a heating rate of 4 $K \cdot min^{-1}$ with 149 minutes of process time. The authors reported a maximum char yield of 40.8 wt.% being in good agreement with other yield values reported in the literature for slow pyrolysis.

V. Chintala et al. 2017 [70] presented a study focused on the conversion of non-edible Jatropha seeds biomass to biofuels i.e., liquid, solid, and gaseous fuels via a solar pyrolysis process. A circular fixed bed reactor was prepared for a batch pyrolysis process with a maximum biomass intake of 15 kg. Solar radiation was concentrated by a 16 m^2 parabolic dish on the reactor surface. The incident solar flux was in the range varying from 0.03–0.07 $MW \cdot (m^2)^{-1}$ with an average reactor temperature of 250–320 °C. The maximum bio-oil yield was about 20%, along with 51% biochar, and 29% pyrolytic gas, which are typical values for slow pyrolysis.

H. Weldekidan et al. 2018 [71] published study in which pyrolysis of rice husk was performed at different temperatures using concentrated solar radiation. The system consisted of a parabolic dish with an aperture diameter of 1.8 m, coated with an 88%

aluminium reflective material. The reactor, a silica glass tube with a length of 35 cm and a diameter of 13 mm, was loaded with a sample of 100 mg of biomass. The solar pyrolysis of rice husk mainly yielded bio-oils (20.6–43.13 wt.%), followed by bio-char, and pyrolysis gases. The pyrolysis gas was observed to increase with temperature from 14 wt.% at 500 °C to a maximum yield of 25.48 wt.% at 800 °C. The study noted that the highest bio-char yield was found to be 43 wt.% at 500 °C.

Solar pyrolytic reactors powered by an artificial light source

For researchers willing to study solar pyrolysis in regions that lack an abundance of natural solar-thermal potential, adapted artificial light sources can serve as sunlight simulators. The main reason for using an artificial light source is independence from natural, adverse conditions that may occur during experiments using natural sunlight. The second reason is to compensate for the lack of natural irradiance in locations like Poland. The sun emits radiation with a spectral wavelengths between 300 to 2,500 nm, with a relative spectral irradiance distribution maximum in the visible light (VL) range (400-700 nm) and a colour temperature of 5 900 K [72,73]. In order to simulate solar light in laboratory conditions, the artificial light source should match the mentioned parameters with the closest approximation possible. V. Esen et al. 2017 [74] presented a way to comprehensively classify solar simulators based on their light sources and their history and technological development. Among the history (starting from 1960s), the most popular light sources adapted for solar simulation were: carbon arc lamps, sodium vapour lamps, argon lamps, quartz-tungsten halogen (QTH) lamps, mercury xenon lamps, xenon arc and flash lamps, metal halide lamps, light emitting diodes (LED), and finally super continuum lasers. The presented study showed that as light technology developed, the efficiency of light sources increased, as well as life cycle of simulators, which are becoming more economical and effective. The final choice of the light source match would be determined by the goal of the study, as well as desirable characteristics and parameters of the light source, with regards to the final cost of the device. In the present study, the authors would like to focus on xenon-arc and QTH lamps as the most commercially-available light sources that possess good thermal power and desirable spectral characteristics.

1.3.2. Solar pyrolysis studies based on artificial light sources

O. Boutin et al 2002 [51] used a 5 000 W xenon lamp and a set of elliptical mirrors to generate up to $7.4 \cdot 10^6$ W/m^2 incident radiant heat flux. In their presented image furnace, a quartz-made cylindrical reactor contained pelletized cellulose powder. The sample was located in the furnace focal zone, where radiation was concentrated at the circular target area with a diameter of $5 \cdot 10^{-3}$ m. The incident heat flux heated the reactor to 800-1 000 °C with enormous heating rates around approximately 4 000 K/s.
Rony et al. 2018 [66] presented a novel pyrolysis reaction system, based on a concentrated solar simulator powered by a modified 5 000 W xenon arc cinema projector, along with

supporting components. Modelling and testing for the generation of bio-based materials, including fuels and chemicals in a quartz glass reactor, was investigated. The lamp radiation was collected and focused on a single pine sawdust sample with two parabolic dishes, generating an available heat flux from 2-7 $\cdot 10^3$ W/m^2, reaching operating temperatures from 750 to 900 °C. Researchers showed that for the presented experimental setup, the optimal temperature for bio-oil production was 750 °C.

In 2000, Grønli and Melaaen [75] published results of experimental and modelling work on the solar pyrolysis of wood under regimes controlled by heat and mass transfer. In a single-particle, bell-shaped Pyrex reactor, one face of a uniform and well-characterized Norwegian spruce cylinder was one-dimensionally heated using a xenon-arc lamp as the radiant heat source. In the work, the effect of applied heat flux on the product yield distributions were investigated.

In 2013, O. Authier et al. [76] presented an image furnace as an efficient laboratory device to study the fundamental aspects of high temperature reactions involving a solid. The basic principle relies on solid heating by concentrated 5 000 W xenon-arc lamp radiation in very clean conditions. The experimental section consisted of a single cylindrical pellet placed inside a transparent quartz reactor with an adjusted focal point of an elliptical mirror. Under these conditions, the values of available heat fluxes varied between 80 and $850 \cdot 10^3$ W/m^2 over a surface of $78.5 \cdot 10^{-6}$ m^2. The study included the values of heat flux densities 200–$900 \cdot 10^3$ W/m^2 which are typically available at the surface of a wood pellet entering a pilot dual fluidized bed (DFB) operating at a temperature of about 850 °C. Pozzobon et al. 2014 [77] presented an image furnace that was developed to study the radiative properties of solids at high temperatures. The proposed furnace consisted of an elliptical mirror which directs every ray coming from the 750 W tungsten halogen lamp at first focus to the sample at second focus. The heat flux on the sample surface is theoretically not uniform because the elliptical reflector is a non-imaging optical device. The presented device could reach average heat flux values as high as $1.8 \cdot 10^5$ W/m^2 on single 5 mm diameter samples, at temperatures up to 800 °C.

Table 2: Summary of recently-developed solar pyrolysis reactors based on artificial light sources with an emphasis on the operating parameters, i.d. – inside diameter, o.d.- outside diameter, h- height, a, b-semi-major and semi-minor ellipse axis, l – length, h – height, w – width.

Reactor			*Radiation source*		Concentration method	Heat flux, MW/m^2	*T*, °C	*β*, *K/time*	Ref.
Material	Shape	Dim., mm	Type	*P*, W					
Quartz	Cylinder	i.d. 30· h 50	Xenon-arc lamp	5 000	Two elliptical mirrors	1.0-7.4	800-1000	~4000 K/s	O. Boutin et al. 2002 [51]
Quartz	Cylinder	o.d. 10	Xenon-arc lamp	5 000	Deep-dish parabolic mirror	0.2-0.7	750-900	-	A.H. Rony et al. 2018 [66]
Pyrex	Bell shaped	i.d. 20	Xenon-arc lamp	-	Lamp reflector	0.08-0.13	300-550	-	M. Grønli 2000 [75]
Quartz	Cylinder	o.d. 30 h 50	Xenon-arc lamp	5 000	Parabolic dish mirror	0.2-0.9	550-850	-	O. Authier et al. 2013 [76]
-	Ellipsoidal	a 150 b 50	Tungsten lamp	750	Two elliptical mirror	0.06-0.18	700-800	25 K/s	V. Pozzobon et al. 2014 [77]
Copper	Rectangular *(4 drilled channels)*	l 180 h 80 w 20	Xenon-arc lamp	1 600	Elliptical reflector	0.17-0.20	700-900	3.9-5.5 K/min	*This study*

Table 2 presents the operating parameters of recently-published solar pyrolytic reactors based on artificial light sources. Researchers chose xenon arc and tungsten halogen lamps as the radiation sources for the pyrolysis reactors. As it can be seen, despite the same nominal power, total reactor performance depends on the method of radiation concentration. The highest temperatures 800-1 000 °C, and heating rate 4 000 K·s- 1, was shown for an image furnace using two elliptical mirrors to concentrate the radiation. For the same lamp power and basic radiation through the lens, the reported temperatures were almost twice as low, reaching 300-550 °C. All the listed reactors are made of highly transparent and transmissive materials, designed to decompose a single particle of biomass. In this study, the authors would like to propose a multi-particle solar pyrolytic reactor. Transparent reactors are problematic in terms of thermal insulation and biomass reflectance losses, what has the dealt with in order to design bigger scale installations. Thermal insulation is crucial to stabilize thermal conditions of decomposition, which in case of slow pyrolysis can lasts for 30-60 minutes. None of presented reactors have investigated multi-particle pyrolysis. A multi-particle device should highlight the issues of parallel pyrolysis in a biomass bed, what is crucial to increase the final product amount, and thus final technology implementation.

1.4. Theses and objectives of the doctoral study

Having in mind literature presented on solar pyrolysis so far, focusing mainly on fast and flash pyrolysis, a basic research on slow solar pyrolysis of different waste biomass feedstock is presented. The first objective of the dissertation is presentation and discussion of the main solar pyrolysis principles, evolving into experimental bench-scale reactor design. Next, the complex evaluation of the process kinetics is presented, with emphasis on universality and wide range of the kinetic approaches chosen. The feedstock decomposition kinetics are evaluated using latest isoconversional techniques as well as traditional model-based kinetics and deconvolution methods. At last, results of the bench-scale solar pyrolysis experimental campaign are discussed. Experimental investigation of the process is aimed for precise recognition of the feedstock behavior during the decomposition, and complex analysis of the solar pyrolysis products.

Doctoral dissertation hypotheses

1) Solar pyrolysis process conditions favors uniform solar pyrolysis products distribution.
2) Carbonization and repolymerization reactions occurring during charring process of biomass during solar pyrolysis can produce hydrogen-rich dry gas.
3) Solar pyrolysis is a method for highly porous biochar production with specifications depending on the feedstock type and process conditions.
4) Model-free kinetic predictions can provide information about the actual process behavior on bench-scale experimental solar pyrolysis reactor.

2. Feedstock characterization

Materials chosen for the solar pyrolysis study are designated as the key-representatives of highest waste biomass potential in Poland, namely: wood industry, agriculture, and municipal economies. In Poland, the annual biomass energy potential is equal to >20 million Mg of waste straw, approx. 4 million Mg of waste wood, and approx. 6 million Mg of sewage sludge [8]. The feedstock collected was prepared for the experimental investigation as pellets, due to several reasons: (1) to provide uniform particle size distribution for the CFD modelling purposes, (2) to increase equality of the thermal diffusivity of the samples, and (3) to increase homogeneity of the biomass within the samples.

Fig. 2.1. Feedsock selected for the study (from left to right) pelletized WS, WW, and SS.

2.1. Characterization of the investigated feedstock

6.1.1. Experimental techniques and standards applied for feedstock properties determination

Ultimate and proximate analysis of ash composition was performed using plasma spectrometer Thermo iCAP 6500 Duo ICP. Investigated fuel properties and elements were determined according to norms: ISO 18134-2:2017-03 for moisture, ISO 18122:2016-01 for ash and volatile matter content, ISO 16948:2015-07 for carbon, hydrogen, and nitrogen, ISO 16994:2016-10 for sulfur and chlorine, IB TL 53 02 from 27.05.2015 for fluor, and EPA Method 7473:2007 for mercury. Ash mineral composition with heavy metals content

was determined according to IB TL 21 07 from 28.05.2013 standard. Lignocelluloses, namely: cellulose, hemicelluloses, and lignin, were recognized with the extraction system Ankom A200 and FOSS Fibertec 2010 and 2011 according to application note FOSS 3434 – AOAC 2002:04/ISO 16472:2005.

2.1.2. C, H, N analysis of solid and liquid products

Simple ultimate analysis of collected char samples and averaged bio-oil samples for each feedstock type was conducted. The weight fraction of carbon *C*, hydrogen *H*, and nitrogen *N* were determined using Truspec CHN628 Leco analyzer. The simultaneous determination of *C*, *H*, *N* was based on Dumas method, also known as the high-temperature oxygen combustion method. The high temperature (950 °C) combined with the flow of pure oxygen provided fast and efficient combustion of the analyzed fuel. The contents of the individual elements were marked using infrared absorption detectors for *C* and *H*, and thermoconductive detector for *N*, where oxygen content *O* was calculated from the balance. Based on experimentally determined elemental composition of the liquid and solid products, a higher heating value (HHV), MJ/kg, was calculated according to *Jenkins-Ebeling* empirical formula:

$$HHV = -0.763 + 0.301 \cdot C + 0.525 \cdot H + 0.064 \cdot O \tag{1.5}$$

2.2. Fuel properties of the investigated biomass types

Investigated feedstock was extensively analyzed in terms of the fuel properties as well as chemical composition concerning lignocellulosic components shares, namely: cellulose, hemicellulose and lignin. Beside obvious characteristics *e.g.*, moisture (M), volatile matter (VM), ash content (AC), elemental composition, or fixed carbon (FC), shares of different lignocellulosic components can give valuable information about expected feedstock behavior during pyrolysis. Numerous studies reported kinetic behavior of specific lignocelluloses with recognition of the Arrhenius parameters and decomposition temperatures, usually as a single-step reaction. Having in mind data presented in Table 2, three pseudo-components model for kinetic analysis of the WW and WS analysis seems reasonable as significant shares of the cellulose, hemicellulose and lignin are denoted. In case of the SS, this theory do not apply, due to the total shares of the lignocelluloses less than 10 wt.%, and requires different kind of approach for kinetics evaluation.

2.2.1. Ultimate and proximate analysis with lignocellulosic components recognition

Basic proximate analysis with elemental composition and lignocellulosic components shares for WW, WS, and SS are presented in Table 3. Regarding proximate analysis results, analyzed feedstock presented typical characteristics among its species reported in the literature. WW pellets, with 9.0 wt.% of moisture, <1 wt.% of ash and up to 83.3 wt.% of volatiles well related with pinewood samples presented by Hu et al. [78] on a study investigating lignocellulosic biomass pyrolysis kinetics. WW lignocellulosic components share were denoted as follows: 54.8 wt.% of cellulose, 11.8 wt% of hemicellulose, and 27.9 wt.% of lignin, with a high content of the latter comparing to other reported wood- derived samples [79,80]. WS elemental composition is well correlated to wheat straw composition published in interesting study on waste tire additive impact on pyrolysis bio-oil yields [81]. Attention drawing is a high content of Cl, 0.234 wt.% what can cause devastation in low-temperature flue gas convective parts of boilers during its combustion for power generation. SS fuel properties are differing significantly from presented lignocellulosic biomass samples. The first difference occurs in much higher ash content, 33.44 wt.%, significantly higher comparing to 0.75 wt.% and 6.69 wt.% for the WW and WS respectively. This phenomenon can be explained by the high content of inorganic matter (CaO, Fe_2O_3) present in the sludge listed in Table 4, consisting on the final ash. Regarding elemental composition, SS contains less *C*, with increased content of the *O*, and *N*, possibly coming from organic matter like proteins or lipids. A significant amount of phosphorus, in the form of P_2O_5, 24.5 mg/kg, being one of the most valuable minerals now, proves priority in its recovery from SS [82,83]. What's more, heavy metals present in ash (Table 5), in the case of lignocellulosic biomass, proved to influence thermal decomposition behavior: shifting cellulose peaks towards lower temperatures [84,85].

Table 3: Fuel properties of the investigated feedstock.

	Proximate analysis, wt.%				Elemental composition, wt.%^{d}					Lignocelluloses, wt%^{d}			HHV$^{a.r.}$, MJ/kg	BET, m^2/g
	$M^{a.r.}$	AC^{d}	VM^{d}	FC^{d}	C	H	$O^{diff.}$	N	S	c	h	l		
WW	9.0	0.8	83.3	15.9	49.6	5.9	44.4	0.06	0.02	54.8	11.8	27.9	18.19	0.224
WS	7.8	6.7	75.1	18.2	47.0	5.7	46.6	0.6	0.2	49.7	31.6	6.0	16.81	0.522
SS	16.6	33.4	60.6	5.9	35.9	5.0	51.5	5.6	2.0	2.1	4.1	1.5	13.02	0.552

Table 4: Mineral ash composition of the investigated feedstock.

Ash mineral comp., wt.%															
	SiO_2	Fe_2O_3	Al_2O_3	Mn_3O_4	TiO_2	CaO	MgO	SO_3	P_2O_5	Na_2O	K_2O	BaO	SrO	Cl	CO_2
WW	39.5	2.56	4.8	2.42	0.35	18.4	2.94	6.23	1.01	1.21	7.39	0.34	0.06	0.5	11.98
WS	50.6	0.23	0.4	0.07	0.03	9.66	2.18	3.16	2.93	0.53	24.1	0.09	0.03	2.6	3.31
SS	20.4	20.9	5.0	0.19	0.87	14.8	3.55	3.28	24.5	0.61	1.32	0.14	0.07	0.01	3.45

Table 5: Heavy metals present in ash samples.

Heavy metals present in ash (mg/kg)										
	Zn	Cu	Pb	Ni	Cr	Cd	As	Hg	Se	W
WW	11.0	0.978	<0.7	0.783	2.45	0.069	<1.0	0.011	<1.0	<1.0
WS	10.3	3.0	0.74	0.94	2.35	0.069	<1.0	0.013	<1.0	<1.0
SS	880.0	517.0	121.0	33.3	51.2	1.22	25.6	1.56	<1.0	7.67

3. Experimental investigation of the solar pyrolysis of waste biomass

Within the Chapter, focused on Research Task II of the presented doctoral dissertation, all the efforts of design and construction of the solar pyrolysis laboratory reactor are presented and discussed. First, the motivation of the reactor design is discussed with emphasis on the interdisciplinary goals of the whole project. Second, the light sources diverse range and availability on the market is presented, with a conclusion of the final xenon-arc lamp choice for the study. As last, the comprehensive presentation of the solar pyrolysis reactor is described along with measurement techniques and data acquisition system.

3.1. The need to develop a bench-scale, slow solar pyrolysis reactor

During the very first project meeting with the research group, the need to develop a reliable bench-scale solar pyrolysis setup was intensely discussed. The need of the new and original design originated as an outcome of the recent published studies on solar pyrolysis, focusing mainly on the fast and flash pyrolysis reactors, with minimum insight into reacting feedstock. During fast and flash pyrolysis the reacting particle, being usually very small <1 mm, reacts in a matter of second into almost solely dry-gas, thus chances to capture decomposition nature or insight into process mechanism are limited. Within the thesis, slow solar pyrolysis is studied as a sustainable method for waste biomass conversion into diversified products. As slow solar pyrolysis reaction times are much higher, a possibility to capture complex pyrolysis nature during extensive measurements opens up. Besides, as designated heating rates, aimed for couple of *Kelvines per minute*, provide decomposition slow enough to form complex measured temperature profiles of the reacting feedstock, and related heating rates profiles, allowing to form temperature correlations to gaseous compounds formation, and even thermoanalytical measurements of the pyrolysis kinetic behavior. On the one hand, the reactor should provide reliable experimental conditions *i.e.*, temperatures, heating rates, ease to collect the products, with simultaneous demand for reliable measurements techniques implementation. One the other hand, having in mind CFD modelling tasks within the project, the setup should also provide reliable data for numerical model validation. Comprising demands on both sides *i.e.*, experimental convenience as well as CFD modelling, the final design emphasizes artificial sunlight as a

light source with a constant, pre-defined and variable intensity, ease of product collection and feeding of the reactor, multi-thermocouple temperature measurement of the bed, with thermocouples located inside the reacting particles, rapid quenching of the bio-oil vapors and infra-red analysis of the dry-pyrolysis gas composition. Material adapted for the reactor body, copper, allows to uniformly distribute heat across the bed, where reacting pellets are formed, allowing axis-symmetrical model implementation for the modeling, reducing computational effort.

3.2. Review of the artificial light sources for solar-thermal applications

3.2.1. Solar simulator versus artificial light source

The application and design of solar radiation sources falls into two main classifications, non-concentrating, uniformly distributed solar simulators used mainly in the testing of photovoltaic cells and solar hot water collectors and high flux concentrators used to generate high temperatures exceeding 1000 °C [86].

The *solar simulators* used for simulation of daily normal irradiation (DNI) are classified in order to spectral distribution, beam uniformity and temporal stability (according to the IEC 60904-9, ASTM E927 & JIS C8912 standards) [87]. The grades are awarded in presented order for each parameter, based on the deviation of offered parameters from standardized values. Solar radiation emissive spectrum consist of wavelength from 250 to 2500 nm with spectral distribution maximum in visible light regime [88]. The best match is awarded with grade *A*, while the poorest is granted with grade *C*. The better the match, the higher the grade e.g. best match is granted with *AAA*, for simulators with worse beam uniformity *ABA* or *ACA* accordingly. Proper terrestrial solar simulators are designed to produce stable 1000 $W \cdot m^{-2}$ radiant flux, which is internationally standardized as 1 sun [89].

Solar devices used for studies that demand high temperatures at the target area and high radiant fluxes, are usually called *light sources*. The differentiation has been made due to omission of American Society for Testing and Materials (ASTM) standards, mainly because of intense radiation concentration, high output power, poor beam uniformity, and secondary approach to spectral match. The output power of artificial light sources, depending on design, can vary from 2 to 10 000 suns [2,50,90]. In mentioned devices, the lamps are crucial factor influencing final device performance [90].

3.2.2. Light sources characterization

Commercially available light sources consists of the lamp, being the heart of whole device, housing containing reflector, optics and cooling system, and finally the power supply [91]. The aim of this paragraph is comparative review of popular lamp types for high-powered light sources with secondary approach to the rest of the equipment. In this paragraph, the comparison of xenon, metal halide lamps and tungsten halogen will be presented. Each of mentioned lamps differs in terms of emissive spectrum, irradiance distribution, luminous efficiency and operational issues (Fig. 3.1.). Choice of final lamp type for declared research goal is crucial part of whole planning progress. Besides technical aspects, lamp type determines final cost of device, which can exceed 11 000 $ in case of xenon light source [92].

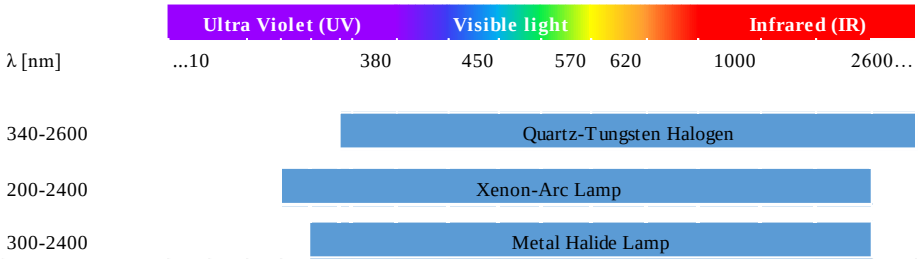

Fig. 3.1. Emissive spectrum range for three presented lamp types: Quartz-tungsten halogen, metal halide and xenon-arc lamps.

3.2.3. Quartz-tungsten halogen

Quartz-tungsten halogen is much cheaper than arc-type and efficient lamp, with spectral characteristics quite similar to natural sunlight, however, with maximum emissive power significantly shifted towards IR [74,93]. Halogen lamps were widely popular in commercial use of the last decades *e.g.*, for domestic and urban illumination or in the car industry. Nominal power of commercially available tungsten halogen lamps varies from 1, 10 to 1 000 W. Despite some of the spectral differences with natural sunlight, tungsten halogen found use in numerous solar thermal research applications [2,73,74,77,90]. Pozzobon et al. [77] presented study of experiments and modelling of wet wood decomposition. Proposed image furnace was powered by 750 W Tungsten halogen with two parabolic mirrors.

Lamp construction

A halogen lamp is a type of incandescent lamp, where a tungsten filament is surrounded by halogen gas in the form of bromine or iodine, heated with an electric current (Fig. 3.2.). [90]

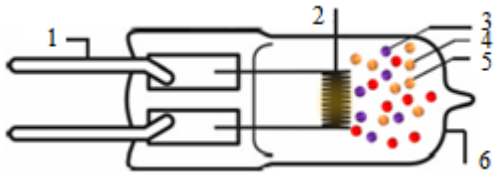

Fig. 3.2. Tungsten halogen lamp structure (1-base, 2-tungsten filament, 3-tungsten atoms, 4-halogen atoms, 5-oxygen atoms, 6-quartz bulb).

Burning of tungsten filament is simple and stable process, the lower the electric current, the lower the filament temperature and its emissive power. This fact provides major advantage of halogen-type lamps over arc lamps, being the simplicity of emissive power control in wide range, just with adjustment of the power supply. Simplicity of construction and low requirements for power supply, allow to easily arrange halogen lamps in multi-filament light sources to provide more output power. Kongtragool et al. [94] arranged 4·1000 W Tungsten halogen lamps to power gamma-configured Stirling engine. Total maximum solar input power has been estimated at 1378 W, with heater temperature of 439 K.

Tungsten halogen emissive spectrum

Tungsten halogen lamps provide smooth emissive power distribution with color temperature of 3400 K, with emissive maximum shifted towards infra-red (IR) regime, with lower ultra-violet (UV) range [73,90,95]. Quartz-tungsten halogen, presents smooth and stable spectrum in visible and near IR with very little UV regime. It can be said, that the lower the halogen nominal power, the shorter the UV emissive range.

3.2.4. Xenon arc lamp

Xenon arc lamps can be found in most of today's high-power light sources for biomass conversion research reactors, due to close matching natural sunlight with intensity and spectrum [31]. Boutin et al. [96] and Authier et al. [76] presented image furnaces for flash pyrolysis of biomass, powered by 5 kW xenon-arc lamp with two parabolic mirrors. Grønli [75] investigated intermediate pyrolysis of single biomass pellet with direct sample heating by xenon arc lamp radiation. Lédé [97] investigated ablative pyrolysis of biomass particles with xenon arc lamp, as a source of high-density heat flux in image furnace. With

proper arrangements and concentration method, xenon lamps can easily produce incident heat fluxes as high as 10^6-10^7 W/m^2 at the focal point.

Lamp construction

Xenon-arc lamp is typical example of discharge lamp. In presented lamp type, the source of radiation is the ionized xenon arc. Quartz bulb contains xenon gas under very high pressure, up to 4 MPa (Fig. 3.3.) [90]. Ignition of xenon arc demands very high direct current (DC) impulse (20 000 to 50 000 V), with continuous care for stable power supply, in order to stabilize the arc and prevent any flicking or gleams. Once arc is formed, the lamp operates at lower voltages with higher electric current, reaching up to 50 A, emitting bright light with significant amount of emitted heat, so the need of cooling occurs. Cooling is usually carried out by forced convection of air or with cooling liquid system. Xenon arc lamps are highly energy-consuming, and demand stable and smooth characteristic of the supplied power, what leads to conclusion, that almost 50% of total device cost stands for power supply only. Due to fragility of plasma arc, adjusting power supply parameters in order to regulate output power can vary between 70-100% in order to provide stable plasma arc. Further regulation must be done with regulation of the focal point position, external shutters or AM filters to cut out some of the power from emitted spectrum.

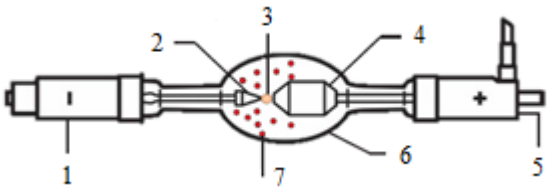

Fig. 3.3. Construction scheme of xenon-arc lamp (1- positive terminal, 2- cathode, 3-discharge arc, 4-anode, 5-negative terminal, 6-quartz bulb, 7-xenon).

Xenon arc lamp spectrum

Xenon arc emits bright radiative flux (3 000 cd for 1 000 W lamp), that shows a good spectral fit with the natural sunlight, with color temperature reaching 6200 K [74]. Presented lamps benefit from an excellent quality and stable spectrum in the UV and visible regimes. Their emission peaks in the IR range can be filtered if required [90].

3.2.5. Metal halide lamp

In a metal halide lamp, the light is produced by an electric arc which is generated through a gaseous mixture of vaporized mercury and metal halide compounds under a high

pressure, ranging from 1 to 3.5 MPa [90]. Metal halide lamps are commonly used in industrial illumination and they are still under development as light sources in high-powered light sources instead of xenon arc lights, whose tend to have high power consumption and high electronic driver costs [74]. Presented lamps has been a subject of numerous studies on solar simulators for photovoltaic studies, yet hardly powered any reactor for biomass conversion [86,88,98].

Lamp construction

The construction of metal halide lamp is somehow similar to halogen and xenon-arc lamp as well (Fig. 3.4.). The idea is based on arc-lamp enclosed in outer bulb, mounted in one socket with two electrodes. Metal halide lamps are perceived as efficient radiation source with long lifetime and low-risk exploitation.

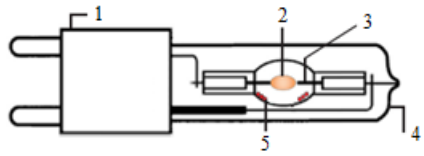

Fig. 3.4.. Construction scheme of metal halide lamp (1-base, 2-discharge arc, 3-electrode, 4-quartz bulb, 5-metal halides).

Metal halide lamps spectrum

The metal halide lamp is an artificial light source that emits a radiation spectrum that closely mimics that of natural sunlight. Metal halide emissive spectrum yields very close matching with natural sunlight in UV and near visible light regions, with color temperature varying from 4 000-6 000 K, depending on the lamp construction [90]. The intense infrared energy spikes that xenon lamps emit require either forced air cooling for low wattage lamps or water cooling for higher powered lamps [86,88].

3.2.6. Comparison of the lamps technical data

Table 6 lists technical parameters of presented lamp types. From operators point of view, the crucial parameters are average life time of the burner, internal pressure, as the safety issue, color temperature and finally conversion efficiency. Tawfik et al. [90] presented a comprehensive review of lamp types for solar-thermal applications. In his work conversion efficiency was expressed as a percentage ratio between radiant output power and nominal electrical power of the lamp.

Table 6: Comparison of technical parameters for the tungsten halogen, metal halide and xenon-arc lamps [90]

Criterion	Tungsten halogen	Metal halide	Xenon arc
Average life time, h	35-480	1000-6100	400-3500
Internal pressure, MPa	0.7-1.0	1.0-3.5	1.0-4.0
Color temperaturę, K	2100-3350	4000-6000	6000
Average conversion efficency, %	10.2	24.6	18.8

Table 7 lists some of the recently developed solar pyrolytic reactors, based on artificial light sources. Undeniably the most popular lamp type chosen by researchers is xenon-arc lamp, with no denoted studies using metal halide lamps so far. Both tungsten halogen and xenon arc lamps provide good thermal performance for the biomass conversion process. In case of pyrolysis, presented artificial solar reactors proved reaching wide range of temperatures and heating rates covering slow, intermediate and flash pyrolysis technology requirements [51,66,75]. Incident heat fluxes listed in are the product of lamp radiant power and radiation concentration method. The highest incident heat fluxes has been denoted for using elliptical mirrors concentrating radiation on a very small target area [51,96].

Table 7: Summary of the recently developed solar pyrolysis reactors based on artificial light sources with emphasis on the operating parameters

Lamp type	Nominal power, W	Concentration method	Incident heat flux [W/m^2] ·10^3	Process temperature [°C]	References
Xenon arc lamp	5 000	Two elliptical mirrors	1 000-7 400	800-100	[36]
Xenon arc lamp	5 000	Parabolic dish	200-700	750-900	[43]
Xenon arc lamp	-	Lamp reflector	80-130	300-550	[35]
Xenon arc lamp	5 000	Parabolic dish	200-900	550-850	[39]
Tungsten lamp	750	Two elliptical mirrors	60-180	700-800	[32]
Xenon arc lamp	*1 600*	*Single elliptical reflector*	*2 200 (absorbed 170-200)*	*800-900*	*This study*

Fig. 3.6. presents a summarizing diagram of the decisive actions taken during the choosing process of the light source for the solar pyrolysis study. The most crucial part for the different lamp types evaluation were criteria's of: (i) sufficient heat supply and (ii) match of the lamp emissive spectra and spectral power distribution with natural sunlight. Based on the presented assumptions, the QTH lamps, despite great aspects of low price and high availability on the market, had to be disqualified due to the highest emissive power in the IR. The only lamp types that were able to provide stable radiant heat flux with maximum emissive power in VL were xenon arc and metal halide light sources. As no metal halides were available on the Polish/European and even American and Asian markets, the choice of the lamp was narrowed to the xenon arc lamp suppliers offers. Among numerous offers

of the different xenon-based light sources suppliers, comprising Canadian, German, American, Polish, and Japanese suppliers, the final choice was a Canadian 1.6 kW (XLH-E-1600X® by Sciencetech-Inc.) light source with a single elliptical reflector radiation concentration method. Chosen offer provided the best ratio of emissive power to price, and as the only company that have had experience with biomass solar-thermal conversion applications. According to the documentation, the lamp provides a highly-focused beam with an estimated power of 288 W and a heat flux density of up to 2.2 MW/m^2 based on the average xenon arc lamp efficiency [90].

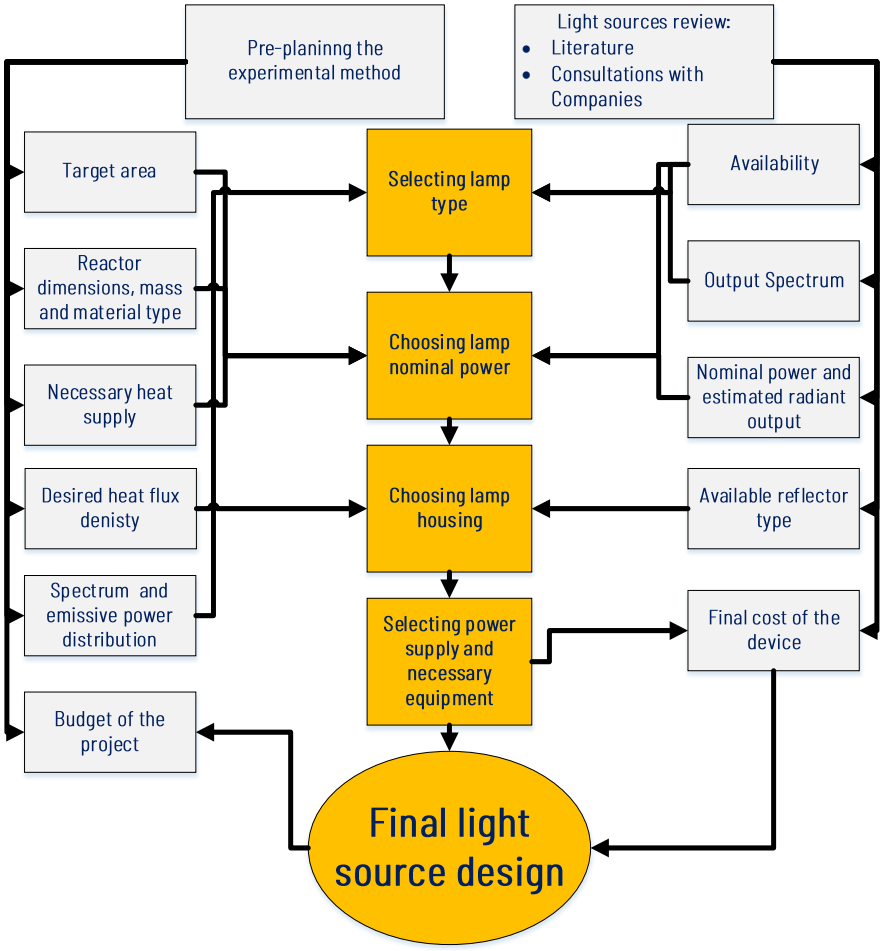

Fig. 3.6. Course of decisions taken during the selection light source for the study of solar pyrolysis of waste biomass.

3.3. Bench-scale solar pyrolysis reactor project

Fig. 3.7. presents the experimental setup of the laboratory-scale solar pyrolysis reactor. The general idea of the reactor is to provide indirect heating of biomass with xenon arc lamp radiation through the opaque, highly-conductive reactor wall. Indirect heating is innovative approach to solar pyrolysis, as previous studies reported on transparent reactors, with denoted severe heat losses from the biomass reflective surface. Another factor favoring opaque reactor wall is potential contamination of the transparent wall during the process, impeding a radiative heat supply to the feed. General idea of the reactor setup is to heat the biomass located inside the copper reactor (Fig 3.7. 2) with xenon-arc lamp radiation (Fig 3.7. 1), and direct the volatile pyrolysis products to the condenser system (Fig 3.7. 4), where the bio-oil is trapped. Simultaneously, online measurements of the process parameters are carried out with the programmable logic controller (PLC) controller placed in the sealed and secured from lamp radiation locket (Fig 3.7. 3). Crucial for the stable xenon-arc lamp operation during experimental operation, as well as its power regulation is a dedicated power supply providing stable DC power, preventing xenon arc from any instabilities (Fig 3.7. 5).

Fig. 3.7. Research stand for a study on the solar pyrolysis of waste biomass (1- xenon arc lamp, 2- insulated copper reactor, 3- data acquisition system container, 4- reactor outlet, liquid fraction condenser, 5- arc lamp power supply).

3.3.1. Reactor bed design

To ensure a uniform temperature field on the reactor walls, and thus uniform heating of biomass pellets, copper has been adopted as a highly-conductive material. An untreated shiny copper surface may cause significant losses of incident heat flux due to the high reflectivity of copper. To provide better black body parameters for the reactor surface, a highly-absorptive coating for commercial solar application has been implemented. Heat losses caused by the high temperature of the reactor walls involved using commercial thermal insulation on the outer reactor wall as well as a reactor copper slab with 4 channels with inner diameters of 10 mm. The reactor outer dimensions are: 160 x 69 x 18 mm (*length, width, height*) as presented in Fig 3.8.a. Due to the anticipated high temperature of the reactor surface, thermal insulation needs to be applied to provide a uniform temperature of the reactor during the experiments. Porogel Plus Pyrogel® (PPP) is an insulation mat, which is manufactured by a nanotechnology process and mainly used in power engineering and industry. PPP is used at temperatures from -40 °C to 650 °C, with a heat transfer coefficient 0.014 W/(mK) at a thickness of 5 mm.

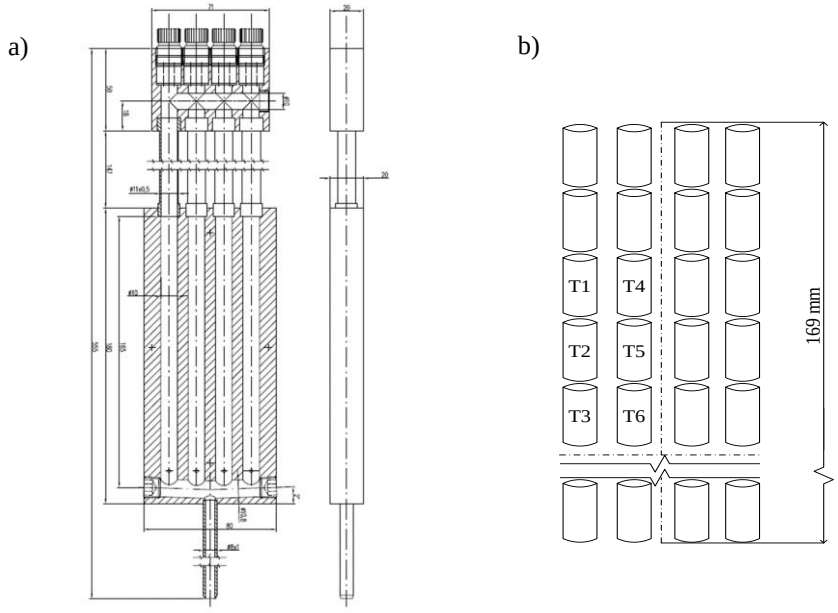

Fig. 3.8. a) Solar pyrolysis reactor cross section with b) illustrated feedstock thermocouples location (T1-T6).

3.3.2. Temperature measurement

Temperature measurement is vital for the study, and is executed by a set of 6 from 16 total k-type thermocouples inside the 6 biomass pellets located in the first two reactor channels (Fig 3.8.b). The actual process temperature recognition is crucial to build conclusion of temperature influence on final product yields. Copper net with a wire diameter of 0.5 mm and quadratic spacing of 0.5 mm was adopted to form and inline pellets, as well as firmly locate thermocouples inside the particles. Due to the uniform dimensions of the pellets and their precise arrangements, the temperature will be repeatedly measured at previously-selected points in a series of experiments. Temperature measurements were conducted with a set of 6 thermocouple connections located within the pellet bed (Fig.3.8b). K-type thermocouples, with a measurement range of 0-1200 °C, uncertainty ±1.5 K, and outer diameter of 0.5 mm, were located in precisely drilled holes in 6 feedstock pellets. Temperatures of the reactor were measured with 4 identical K-type thermocouples located (axially-symmetrical) between the non-irradiated reactor wall and insulation. The thermocouples signal was recorded by two 8 socket WAGO thermocouple *750-458* module and recorded with WAGO PFC100 PLC with the sampling interval of 1 s. The temperature distribution among 6 uniform pellets within the same feedstock was perceived as a random test population being heated under uniform conditions. Expected feedstock temperature and its standard deviation were estimated with *Student's t distribution* for n=6 random temperature observations for 90% confidence interval and degree of freedom v=n-1, for every second. The confidence interval (CI) Eq. (3.1) of measured temperature was calculated as:

$$CI = (\bar{T} \pm t_{\alpha,v} \frac{S_n}{\sqrt{n}}) \tag{3.1}$$

$$S_n^2 = \frac{\sum_{i=1}^{n=6} (T_n - \bar{T})^2}{n-1} \tag{3.2}$$

Having determined unbiased estimate of the sample variance, S^2, one can easily determine the standard deviation estimate, s, with square rooting of the Eq. (3.2), which will be further presented as a temperature measurement accuracy criteria.

3.3.3. Pressure measurement

In order to determine pressure drop in a fixed bed, the smart pressure transmitter APC-2000G ALW has been adapted. Pressure measurement is carried out between static pressure points at the reactor inlet and outlet of pyrolysis gasses.

3.3.4. Data acquisition system and methods

For the purpose of measurements data acquisition the WAGO Programmable logic controller (PLC) equipped with dedicated 2 modules for thermocouples and 1 universal analog input module were adapted. The heart of the system was WAGO PLC-PFC1000 (*series number* 750-8100) providing a link between signal gathering modules from thermocouples (750-458) and analog devices (750-496): pressure transducer and the El-Flow flow meter. Process data were collected by the laptop with installed WAGO e!Cockpit software, where own-implemented script based on WAGO DataLogger function block was directing data to the .csv files each second, while WAGO DataPlotter web-application was plotting momentary values of the measured quantities onto the computer screen.

3.3.5. Liquid products separation and cooling system

Heavy and condensable bio-oil vapors are naturally directed to the set of 5 quartz-glass spiral coolers, supplied with cold water from the cryostat. Cooling water temperature was compromised between the vapor cooling effectiveness and freezing point of the cryostat evaporator, resulting in a 2.0-3.0 °C dependent on ambient conditions. Cooling water flow through the spirals was kept at a maximum flow-rate in order to maximize the forced cooling of the vapors. The cryostat outlet with the lowest water temperature was connected to the spiral farthest from the reactor outlet (closest to the analyzers), creating counter-current heat exchange between the cooling water and a process gas. Effective cooling of the pyrolysis process gas is crucial from the two points: (i) vapors must be condensed in a 100% in order to determine the mass balance of the process, (ii) IR analyzers must be protected from any condensation inside the measurement cell. Condensation of any liquid (especially heavy bio-oil compounds) can damage the reflective surface of the cell and cause error in the measurement or even damage the device.

3.3.6. Infrared gas analyzers setup

The unit consists of ABB URAS 2020 and SIEMENS Ultramat 6 gas analysers, an additional gas cooler, and a heated hose for sampling. The analysers allow for the measurement of CO_2 content (range: 0 - 20%), O_2 (range: 0 - 25%), SO_2 (range: 0 - 1%), NO (range: 0 - 2500 ppm), and CO (range: 0 - 30%). The measurement signals are sent to the automation system via radio using Satel radio modems, and data acquisition system. The gas analyzer setup consisted of 4 analyzers based on NDIR technique. Two ABB Uras 14 modules were responsible for CO, CO_2, and O_2 detection, while two Siemens Ultramat 6 analyzers measured CH_4 and H_2 formation. Gases measurement range was 0-30 vol.% for CO and CO_2, 0-25 vol.% for O_2, 0-10 vol.% for CH_4, and 0-5 vol.% for H_2. The sampling interval of the analyzers was 1 s.

3.3.7. Solar pyrolysis experimental setup

The reactor *inlet* was connected to the inert gas pressurized bottle through the pressure reducing valve. After pressure reduction, the inert gas path was divided into two routes, one supplying the reactor and the second providing a controlled leak of nitrogen to the atmosphere, whose rate was controlled by another rotameter without affecting the main inert gas flow. This setup provided a safe outlet for excess pressure to the system that could be initiated during experiment failure, which otherwise could damage the analyzer cells. The main inert gas stream was directed into 4 channels through a main inert gas rotameter, passing through the bed. The reactor outlet was collected gases and vapors passing them to a condenser consisting of a set of 5 quartz spiral coolers supplied with cold water provided by the cryostat. Next, the dry, cooled gas was directed through gas analyzers for evolving species recognition during the process. The gas path was kept as short as possible to provide quick response of the analyzers to feedstock behavior during the solar pyrolysis process.

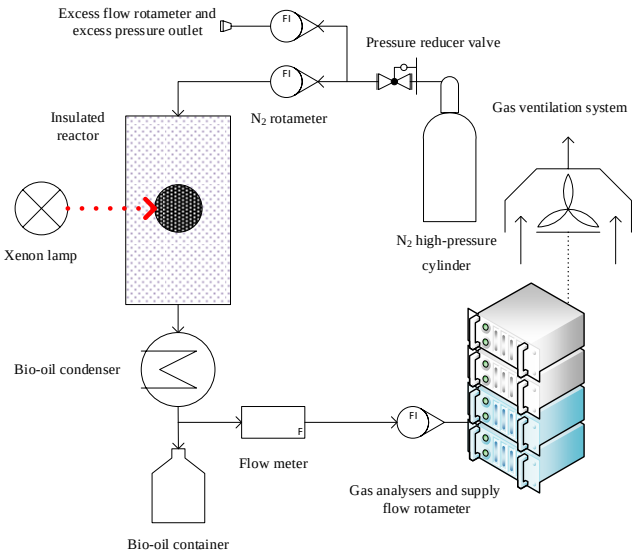

Fig. 3.9. Solar pyrolysis reactor setup.

Measurement uncertainties and errors

Precise recognition of experimental uncertainties and errors was crucial reliable and worthy experimental data, which could be used for validation of numerical CFD models [99,100]. The highest uncertainty within this study was expected to arise from pyrolysis gas yield calculations using Eq. (9.3). According to ABB and Siemens NDIR analyzer manuals, even after calibration, they possess an error of 0.2 and 0.5 % of the maximum measured range value, respectively. This deviation was taken into account for calibrated ranges of measured species, in which the maximum deviation of gas yield was calculated. The temperature measurement uncertainty was ±1.5 K according to thermocouple specification, while the uncertainty of laboratory precision balance used to weight the chars and feedstock was ±1 mg.

Table 8: Uncertainties of key measurement instruments.

Measured parameters	Uncertainity
Temperature (K-type thermocouple 0-1100°C, 1st class accuracy)	±1.5 K
N_2 flow rate (Bronkhorst El-Flow Prestige, FG-111B 0-300 Nl/h)	±0.40%
Gas composition (ABB AO2020 Uras 14 CO, CO_2, O_2)	±0.20%
Gas composition (Siemens Ultramat 6 CH_4, H_2)	±0.50%
Mass balance	±1 mg

3.4. Experimental procedure for the solar pyrolysis experiments

3.4.1. Sample preparation

For a single experiment a total mass of 20 g of specific biomass type was decomposed. Feedstock pellets with an outer diameter of 6 mm and total length of 10±0.5 mm, were placed inside the thin copper net, with a wire diameter of 0.25 mm and space size of 0.5 mm. Six holes with 0.5 mm diameters were drilled (Fig. 3.7.) in centrally located pellets for thermocouple location. Packing pellets with copper net inside the reactor was adapted to firmly locate the thermocouples as well as providing easy char collection after the process. During the process, thermocouple connectors and wires were kept away from the radiation source to prevent any false heating of the temperature signal path.

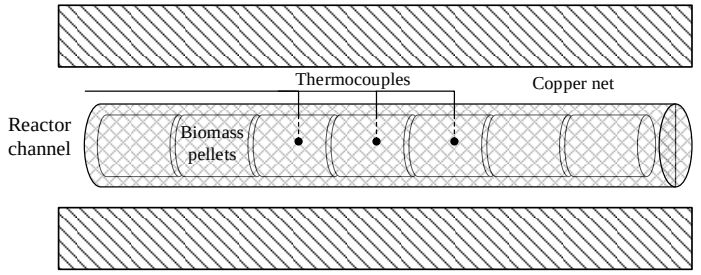

Fig. 3.10. Scheme of biomass samples location inside the solar pyrolysis reactor, with denoted thermocouples joints placement.

3.4.2. Investigated variables

For the study, waste biomass behavior during solar pyrolysis is investigated for the variable xenon arc lamp power. Due to the technical limitations of the xenon arc lamp technology, mainly due to the stability of the arc, selected power levels of 90, 95, and 100% of total 1.6 kW power were adapted.

3.4.3. Main stages of the solar pyrolysis experiments

1) Feedstock preparation: cutting of the biomass pellets to a uniform length, and uniform distribution of the samples across four reactor channels.

2) Drilling of the thermocouple ports in 6 selected pellets, and careful placing of the thermocouple joints inside the drilled samples.
3) Feeding of the biomass pellets with thermocouples into the reactor channels. Sealing the screw connection with silicone seal-cylinder.
4) Assembly of the gas path line from nitrogen pressurized tank through the reactor, cooling system and the gas analysers. After the connection is set, a pressure tightness test is performed.
5) Establishing a steady state: launching a data acquisition system, setting nitrogen flow rate, 1 l/min, and gas analysers. Steady state is established when thermocouples, pressure, and flow rate values reach stable level. Purging of the reactor system is complete, when oxygen indication on the gas analyser drops below 0.01 vol.%.
6) Ignition of the xenon-arc lamp. Beginning of the of the measured variables record on PLC.
7) Experiment is finished when gas analysers indications reach initial steady state values.
8) After cooling the reactor is opened, and solid residue is weighted and stored. Bio-oil condenser is disassembled and collected liquid is washed out with acetone, and stored. Recorded data are downloaded from the PLC and stored at the computer's memory.

3.4.4. Products collection and yields calculation

Solar pyrolysis products were collected upon cooling of the reactor to room temperature after the process. Biochars were collected from the reactor in the copper net and weighted, and then the solid product yield was calculated (g_{char}) using Eq. (3.3). Liquid products were collected from the first dripping condenser and preserved in dark glass for further chemical and environmental analysis. Gaseous products were released into the atmosphere via the ventilation system, after passing it through the gas analyzer system. The pyrolysis gas yield (g_{gas}) calculation was based on the gas analyzer results and partial densities of the specific species, calculated for the measured temperature of the gas, which throughout the experiments was kept at ambient temperature, according to Eq. (3.4.). Volumetric shares were determined by the analyzer in combination with the actual density of the mixture (ρ_{gas}), which in turn allowed the mass of released gas to be calculated. This was conducted under known analyzer sampling flow rate $\dot{V}$, determined by both analyzer rotameter and Bronkhorst El-flow flow-meter that was mounted after the bio-oil condenser system (Fig. 3.9.). Bio-oil share (g_{oil}) was calculated as the difference obtained from the balance Eq. (3.5). The formulas for product yield calculation are given below.

$$g_{char} = \frac{m_{char}}{m_{feed}} \tag{3.3}$$

$$g_{gas} = \frac{1}{m_{feed}} \cdot \dot{V} \cdot \int_{t} \rho_{gas}(t,T)dt \tag{3.4}$$

$$g_{oil} = 1 - g_{gas} - g_{char} \tag{3.5}$$

Together with product yields, as well as its energy content based on calculated empirical correlation for HHV (1.3), it is possible to calculate energy upgrade factor (EUF), which was the ratio of the useful chemical energy difference between solar pyrolysis products and feedstock, related to the initial chemical energy of feedstock:

$$EUF = \frac{\sum_{i=1}^{3} g_i HHV_i - HHV_{feed}}{HHV_{feed}} \tag{3.6}$$

4. Thermogravimetric analysis of the feedstock behavior during pyrolysis

Thermogravimetric analysis (TGA) is a thermo-analytical method used to determine the rate of the decomposition process of the specified material under various atmospheres. The main investigated variable is the mass loss of the sample during isothermal or non-isothermal conditions. At isothermal conditions, the measurement starts with pre-heating ramp of the apparatus with the sample to designated temperature, and later, the balance measures the sample mass loss as a function of time. During non-isothermal (or dynamic) TGA, the mass loss is determined at a constant heating rate, and the measurement is terminated at specified temperature. Historically-wise in biomass conversion field, non-isothermal measurements are leading in terms of reliability over isothermal ones, due to omission of unavoidable non-isothermal behavior of the sample during pre-heating, and ability to investigate process rate at a wide temperature range within a single run. In general, TGA provides information about physical phenomena, such as phase transitions, absorption, adsorption and desorption; as well as chemical phenomena including chemisorption, thermal decomposition, and solid-gas reactions (*e.g.*, oxidation or reduction). The whole process is conducted on an instrument referred to as a thermogravimetric analyzer. A thermogravimetric analyzer during the measurement continuously records mass while the temperature of a furnace, and sample is changed over time. A typical thermogravimetric analyzer consists of a precision balance with a sample pan located inside a furnace with a programmable temperature control device. During dynamic measurements, the temperature is generally increased at constant heating rate (or for some applications the temperature is controlled for a constant mass loss) to incur a thermal reaction. The thermal reaction may occur under a variety of atmospheres including: ambient air, vacuum, inert gas, oxidizing/reducing gases, corrosive gases, carburizing gases, vapors of liquids or "self-generated atmosphere". For the pyrolysis TGA measurements, the sample decomposition is investigated usually under a nitrogen atmosphere, rarely using other inert gasses *e.g.*, argon. The thermogravimetric data collected from a thermal reaction are compiled into a plot of mass or percentage of initial mass profile over temperature.

4.1. Obtaining computational-worthy data

Extensive work on recommendations and advice for kinetic data gathering and further computations was published by International Confederation for Thermal Analysis and Calorimetry (ICTAC) Kinetics Committee in a series of publications [101–104]. Within this section, only a summary of the ICTAC input will be presented and discussed, addressing key-issues of the task consisting of the doctoral dissertation.

The most crucial part of the measurement accuracy is to provide an accurate temperature of the reacting sample. Thermal analysis instruments control precisely the reference *i.e.*, furnace temperature, while the sample temperature can deviate from it due to its limited thermal conductivity or due to the thermal effect of the process that may lead to self-heating/cooling. The severity of this problem increases with larger sample masses and faster heating rates (or higher temperatures), so the need for preliminary tests to demonstrate that there is no sample mass dependence is highly advised. This can be easily executed with a few runs on samples of two markedly different masses, *e.g.*, 10 and 5 mg, and making sure that the obtained data give rise to the kinetic curves that can be superposed or, in other words, are identical within the experimental error. Otherwise, the sample mass needs to be decreased until the superposition is accomplished. Sometimes within the literature, a tendency can be denoted to favor extremely small sample mass investigated at TGA, even less than 1 mg. This practice is motivated by the desire to minimize the diffusion effects on the recorded signal. The diffusion of the reactants through the solid-state sample is especially crucial for the processes carried out under a reactive atmosphere *e.g.*, oxy-combustion. In that case, the effort must be focused on obtaining kinetic data not limited by the diffusion of the oxygen through the sample, by minimizing diffusion resistance, usually by decreasing the sample mass or increasing the crucible area. However, for such a small sample mass, some extra non-diffusion deviations or *floating* of the signal can occur, caused by strictly technical issues of the insufficient balance resolution or dynamic effect of the carrier gas flow through the crucible. Luckily, the diffusion effect usually has minimal impact on the kinetics of the pyrolysis process for samples within 5-10 mg under an inert atmosphere, where the process is not limited by the inert gas. However, the higher the particle size and general mass of the investigated sample, temperature errors may occur caused by thermal conductive resistance, which combined with self-heating can cause thermal-lag of the sample to reference temperature, causing problems in later kinetic data interpretation.

4.2. Thermogravimetric analysis setup

Waste biomass behavior during pyrolysis was investigated on STARe System TGA/DSC3 HT 1600 manufactured by Mettler Tolledo. Main conditions of the non-isothermal (dynamic) TGA analysis are listed below.

- Single experiment was carried out for the 5 mg of the milled, non-sieved biomass samples in Al_2O_3 crucible pans.
- Pyrolysis conditions were provided by the 50 ml/min nitrogen flow.
- Biomass decomposition was investigated at heating rates from 5-40 K/min.
- Each heating rate was investigated at temperature range 25-700 °C, without repetitions.

5. Kinetic analysis of the solar pyrolysis process of the waste biomass

In this Chapter all the kinetic computations carried out during the Ph.D. are summarized and presented. For the purpose of the study, the latest techniques were adapted from the relevant literature comprising model-based and model-free, isoconversional kinetics. In the forthcoming paragraphs basic principles of the kinetic analysis of the solid-state reactions are presented with further presentation of the techniques used for pyrolysis kinetic modeling of the waste biomass.

5.1. Condensed-phase kinetic analysis principles

Kinetics deals with measurement and parameterization of the process rates. Thermal analysis is concerned with thermally stimulated processes, *i.e.*, the processes that can be initiated by a change in temperature. The rate can be parameterized in terms of three major variables: the temperature, T; the extent of conversion, α; the pressure, p as follows [105]:

$$\frac{d\alpha}{d\tau} = k(T)f(\alpha)h(P) \tag{5.1}$$

The pressure dependence, *h(P)* is ignored in most of kinetic computational methods used in the area of thermal analysis. It should, however, be remembered that the pressure may have a profound effect on the kinetics of processes, whose reactants and/or products are gases. However, as pyrolysis and gasification is usually carried out at atmospheric pressure, the pressure addend *h(P)* can be neglected. A satisfactory understanding of biomass pyrolysis can result in the dramatic development of a biomass conversion process [106]. The energy balance present in Eq. (1) does not consider phenomena such as heat conduction in solids, heterogeneity of reactions, secondary reactions and diffusion, or density changes in the sample, etc. Over the years, researchers have attempted to solve the mystery of the pyrolysis mechanism by proposing new reaction models. There are two main approaches for the calculation of kinetic parameters, depending on whether the reaction mechanism (model) is known or not. John E. White et al. 2011

[107] presented a comprehensive review of recently used kinetics estimation methods, comparing the reaction model approach with iso-conversion. The model-based approach assumes a known reaction mechanism and is the correlation between the equations of decomposition functions (models). In case of kinetic modelling of pyrolysis choice of reaction type and mechanism is crucial. Moukhina [108] presented comprehensive study on determination of reaction mechanism based on TGA data showing how to recognize system of consecutive, independent or competitive reactions. In this approach, the appropriate reaction model is selected on the basis of a best regression fit, or master plot method described and discussed elsewhere [78]. In the case where the reaction mechanism is fairly unknown, Vyazovkin et al. [104] reviewed computational methods to estimate kinetic parameters based on isoconversional assumptions. The model-free kinetics originated from an iso-conversional principle that allows the reaction model to be eliminated from kinetic computations. This principle states that the reaction rate at a constant extent of conversion is only a function of temperature.

5.1.1. Canonic solid-state rate equation

The rate of virtually any thermally-driven processes can be expressed as a function of temperature, T, and rate of conversion, α:

$$\frac{d\alpha}{d\tau} = k(T)f(\alpha) \tag{5.2}$$

The rate of decomposition, sometimes referred to as the extent of reaction, is defined as the mass loss of a biomass sample during the decomposition at a certain time, in relation to the initial feedstock mass:

$$\alpha = \frac{m_0 - m_\tau}{m_0 - m_f} \tag{5.3}$$

5.1.2. Arrhenius formula for the rate constant

In theory, every thermally-driven chemical reaction obeys the Arrhenius equation, expressing the formula for homogenous reaction constant. When the Arrhenius equation is applied to Eq. (5.2), a kinetic equation for the isothermal single-step canonical reaction is obtained:

$$\frac{d\alpha}{d\tau} = A\exp\left(\frac{-E}{RT}\right)f(\alpha) \tag{5.4}$$

In kinetic theory, the activation energy is defined as the amount of energy needed for the formation of products by closing the distance between the reactant molecules or increasing their kinetic energy, and *A* is pre-exponential factor, which is defined in kinetic theory as reaction rate at infinite temperature, or the probability of a successful collision between two reacting molecules, whose units are the same as the reaction constant.

5.2. Model-free, *isoconversional* and model-based kinetics

Within this paragraph, a brief presentation of the model-based and model-free, isoconversional kinetics is presented. Along basic introduction, some latest techniques listing deconvolution and master plot are presented as a supplementary material to enrich the spectra of the kinetic computations of the dissertation.

5.2.1. Model-based kinetics

In solid-state kinetics, especially for the non-isothermal degradation of complex materials, the Arrhenius parameters are highly dependent on the *f(α)* chosen [109]. When a thermoanalytical experiment e.g. TGA is conducted under a heating rate, *β*, K/min, (5.5) both *k(T)* and *f(a)* change simultaneously during the measurement, hence a single run contains highly correlated information about both the temperature and conversion dependencies of the process rate [110], Eq. (5.4 and 5.7). During inverse kinetic analysis, this correlation reveals itself with a drastic change of Arrhenius parameters values with an assumption of different *f(α)*.

$$\beta = \frac{dT}{d\tau} \tag{5.5}$$

$$\frac{d\alpha}{d\tau} = \beta\frac{d\alpha}{dT} \tag{5.6}$$

$$\frac{d\alpha}{dT} = \frac{A}{\beta}\exp\left(\frac{-E}{RT}\right)f(\alpha) \tag{5.7}$$

In model-fitting kinetics the applicability of specific *f(α)* chosen is determined based on statistical fit to experimental data [109] or master-plot methods [78,109,111–115].

The principle equation for the elementary reaction step Eq. (5.7), states that kinetic parameters are constant for the reaction extent. All the conversion dependency is encrypted in reaction model, $f(\alpha)$, being a mathematical expression of the conversion function. Big advantage of model-fitting kinetics is ability to create complex kinetic models, with number of elementary kinetic steps, having the specific kinetic triplet, bounded by independent, consecutive or parallel mechanisms [34,108,112,116–118].

The various pyrolysis models can be divided into three principal categories: single-step global reaction models, multiple-step models, and semi-global models [107]. The proposed models comprise a pyrolysis reaction as a set of processes that occur globally, discretely, along, independently, competitively, consecutively, or some combination thereof, described by non-linear regression fit. The single-step model assumes one global activation energy for the entire process. The semi-global models assume that the pyrolysis of biomass can be divided into two or three independent reactions, each with its own rate of product formation (volatiles and char). This method allows the consideration of secondary reactions and a lumped analysis of the system, without considering the biomass structure, where the products are produced through single-step or multi-step reactions. The most complex multi-step models consider various numbers of formation reactions during pyrolysis. The final computational effort involves several reaction models, each with its own kinetic parameters and a known correlation between them (reaction mechanism), which is still not entirely known for pyrolysis. Researchers investigating lignocellulosic biomass pyrolysis have proposed a distributed activation energy (DEAM) model, as originally proposed by Vand. This model, developed over several years, distinguishes biomass structure for three main components: cellulose, hemicellulose, and lignin. The decomposition of each component is described by their own pseudo-nth-order rate integral form, which leads to a final non-isothermal reaction rate equation through derivation, where the activation energy is described by Gaussian or Weibull distribution with a specified standard deviation [119]. Trinth et al. 2019 [84] investigated pyrolysis kinetics of two energy crops collected from phytoremediated soils. Study established three-pseudocomponent kinetic model adressing biomass components with activation energies within 20-103.55 kJ/mol and reaction orders within 1.01-1.99. Mangut et al. 2006 [33] published kinetic data from the pyrolysis of waste biomass from a tomato processing factory, and his model consisted of 12 reactions identified from the DTG curves. While useful in some cases, multi-step models are still limited by the incorporation of several independent serial reactions [107] which are vulnerable to cascade error from inaccuracies in single reactions.

Main assumptions of the model-based kinetics

The model-based calculation approach is usually based on selection of the reaction model *a priori*. The first assumption for the model-based method is stated that the reaction

consists of several elementary reaction steps, and the reaction rate of each step can be described by an own kinetic Eq. (5.8), depending on the concentration of the initial reactant a_j, the concentration of product b_j, the pre-exponential factor A_j and the activation energy E_j, specific only for this step with number j.
Within this thesis, a kinetic computations were performed using a licensed software *Netzsch Kinetics Neo*. In this software, reaction models are expressed as $f_j(a_j,b_j)$, where a_j and b_j stand for normalized concentrations of reactant and product respectively, where the latter is usually presented in the literature as $(1-a_j)$. According to this manner some examples of known reaction models are: nth order based reaction $f = b^n$, Šesták–Berggren $f = a^m b^n$ or one-dimensional diffusion $f = 0.5/a$. At first sight this notation may seem misleading, however it is extremely convenient during the calculation of multi-step kinetic models, where each elementary step species has its own reactants extents, $a,b,c,d,\ldots$

The second assumption for model-based analysis states that all kinetic parameters like activation energy, pre-exponential factor, reaction orders, and reaction models are assumed constant during the reaction progress for every individual reaction step.

The third assumption for model-based analysis: total thermoanalytical signal, Eq.(5.9) is the sum of the signals of the single reaction steps. The effect of each step is calculated as the reaction rate multiplied by the effect of this step (for example enthalpy change or mass loss).

$$\left(\frac{d\alpha}{d\tau}\right)_j = \left[\frac{d\left(a_j \rightarrow b_j\right)}{d\tau}\right]_j = A_j \exp\left(\frac{-E_j}{RT}\right) f(a_j, b_j) \tag{5.8}$$

$$m = m_0 - \Delta m \cdot \left[\sum_{j=1}^{n} c_j \int \left(\frac{d(a_j, b_j)}{d\tau}\right)_j d\tau\right] \tag{5.9}$$

In the case of single-step reactions, where the reaction model remains constant for the duration of the process, both model-based and model-free should provide results with the same kinetic parameters, which are fixed (for model-based) or almost constant (for isoconversional) during the reaction. For complex processes, where the kinetic mechanism is changing, a big difference appears in the interpretation of the two methods results, provided by different approaches. For isoconversional methods, change of the model is described by the continuous change of kinetic parameters with the increase of reaction extent. For model-based methods, the change of the kinetic mechanism is simulated by several reaction steps, with own kinetic triplets, ranked in a specific order.

5.2.2. Numerical techniques for the deconvolution of the overlapped signal

Multi-step kinetics commonly manifest themselves in the form of overlapped rate peaks as measured by differential TGA. In the present context "deconvolution" means resolution of the overlapped rate peaks into individual rate peaks that can be expected to represent individual reaction steps [103]. Deconvolution methods are numerical procedures based on multiparametric optimization procedure of fitting the root function to a designated signal, usually expressed as dα/dτ. Lately, an elegant *Matlab* self-containing function *peakfit.m* was provided by the Tom O'Haver (2021) containing a set of functions ready to treat very complex overlaps in a different kinds of signals. The following various deconvolution root functions are used in the latest literature [120]:

$$\textit{Gasussian: } y = a_0 \exp\left[-\frac{1}{2}\left(\frac{x-a_1}{a_2}\right)^2\right] \tag{5.10}$$

$$\textit{Lorentzian: } y = \frac{a_0}{1+\left(\frac{x-a_1}{a_2}\right)^2} \tag{5.11}$$

Weibull:

$$y = a_0\left(\frac{a_3-1}{a_3}\right)^{(1-a_3)/a_3}\left[\frac{x-a_1}{a_2}+\left(\frac{a_3-1}{a_3}\right)^{1/a_3}\right]^{a_3-1}\exp\left\{-\left[\frac{x-a_1}{a_2}+\left(\frac{a_3-1}{a_3}\right)^{1/a_3}\right]^{a_3}+\frac{a_3-1}{a_3}\right\} \tag{5.12}$$

$$\textit{Fraser-Suzuki: } y = a_0 \exp\left\{-\ln 2\left[\frac{\ln(1+2a_3\frac{x-a_1}{a_2})}{a_3}\right]^2\right\} \tag{5.13}$$

The last function presented, Fraser-Suzuki function, gains considerable interest in the latest kinetic literature. M. Hu et al. [78] presented excellent study on lignocellulosic biomass pyrolysis kinetics with implementation of the Fraser-Suzuki deconvolution. The special ability of the mentioned function lays in additional parameter, dimensionless asymmetry, a_3, and providing excellent fitting ability to complex and overlapped profiles in multi-step models. However, inverse fitting of the rate equation with traditional reaction models to the latter is problematic, and usually sets the need to evaluate the most probable

f(α) functions for separated pseudo-components. This can be done by secondary isoconversional analysis of the reintegrated pseudo-components conversion profiles forming pseudo-TGA mass loss profiles of the specific pseudo-components. In the mentioned study the pyrolysis mechanism of bamboo pseudo components after deconvolution obeyed the theoretical models, random scission model $f(\alpha)=2(\alpha^{1/2} - \alpha)$ for cellulose and third-order model $f(\alpha)=(1-\alpha)^3$ for hemicellulose and lignin.

5.2.3. Isoconversional principle

Thanks to the development and popularization of isoconversional kinetic methods, conversion dependency of E_α can be well estimated without *f(α)* assumption, previously assumed arbitrary [84,121] or identified using master-plot methods [78,112]. The latest work of Vyazovkin [110] showed, that isoconversional kinetics are well capable of predicting not only activation energy, yet frequency factors as well as yield information about the actual reaction models, thus arguably whole kinetic triplets normalized for the conversion extent, $\alpha=(0,\ldots,1)$.

The isoconversional kinetics takes its origin in the isoconversional principle that allows one to eliminate the reaction model from kinetic computations. The principle states that the process rate at constant extent of conversion is only a function of temperature [105]. For the $\alpha=const$, the following assumptions are easy to derive from Eq. (5.7) by taking the first logarithmic derivative.

$$\left[\frac{\partial \ln(d\alpha/d\tau)}{\partial T^{-1}}\right]_{\alpha=const} = \left[\frac{\partial \ln k(T)}{\partial T^{-1}}\right]_{\alpha=const} + \left[\frac{\partial \ln f(\alpha)}{\partial T^{-1}}\right]_{\alpha=const} \tag{5.14}$$

Further investigation of Eq. (5.14) with $\alpha=const$ assumption leads to a conclusion that addend consisting reaction model *f(α)* is zeroed, and the rest reduces to an elegant Eq. (5.15), revealing the isoconversional (apparent) activation energy specific for corresponding α.

$$\left[\frac{\partial \ln(d\alpha/d\tau)}{\partial T^{-1}}\right]_{\alpha=const} = \frac{-E_\alpha}{R} \tag{5.15}$$

It follows from Eq. (5.15) that the temperature dependence of the isoconversional rate can be utilized to determine the isoconversional values of the activation energy, E_α without identifying or assuming any form of the reaction model. That is why isoconversional

methods are frequently called as "model-free" methods. While catchy, this term is not to be taken literally. It should be kept in mind that although the methods do not have to identify explicitly the model, they still assume implicitly that there is some $f(\alpha)$ that defines the conversion dependence of the process rate. The temperature dependence of the isoconversional rate is obtained experimentally by performing a series of runs at different heating rates. It usually takes three to five runs at different heating rates or at different temperatures to determine such dependence.

5.2.4. Model-free, isoconverisonal kinetic methods

Friedman method

Henry L. Friedman in 1963 proposed a method description devised for obtaining rate laws and kinetic parameters which describe the thermal degradation of plastics from TGA data [122]. The differential Friedman method formula Eq. (5.16) is rearranged from Eq. (5.4):

$$ln\left(\frac{d\alpha}{d\tau}\right)_{\alpha} = ln\left[Af(\alpha)\right]_{\alpha} - \frac{E_{\alpha}}{RT_{\alpha,i}} \tag{5.16}$$

where the subscript i stands for the *i-th* heating rate; $T_{\alpha,i}$ is a temperature corresponding to given (constant) α of *i-th* heating rate; E_{α}, denotes the apparent activation energy, kJ/mol. In the linear fittings of $\ln(d\alpha/d\tau)$ versus $-1/T$, E_{α} can be determined from the slope of the left side of Eq.(5.16) against the reciprocal temperature for constant values of α; while the $A_{\alpha}f(\alpha)$ (sometimes called *modified* pre-exponential factor [123]) can be calculated from the intercept values. For kinetic computations, the crucial part is the experimental determination of computational-worthy data, conversion rate profiles $d\alpha/d\tau$, and accurate temperatures corresponding to specific conversion points α. Despite being one of the earliest methods, Friedman formula is very popular and reliable estimate of the E_{α}, due to its ability to evaluate isothermal and non-isothermal data, and the lowest errors, laying only within the thermoanalytical measurement quality [124–128].

Apart from differential methods, also integral methods are equally popular within the literature [80,129–131]. Integral isoconversional method originated from a different approach to E_{α} determination with the integration of equation (5) after simple separation of variables with respect to α.

$$g(\alpha) \equiv \int_0^{\alpha} \frac{d\alpha}{f(\alpha)} = A\int_o^{\tau} exp\left(\frac{-E}{RT}\right)dt \tag{5.17}$$

Where *g(α)* is integral form of the reaction model *f(α)*. Simple application of isoconversional principle (4.15) to Eq. (5.17) results in:

$$ln\,\tau_{\alpha,i} = ln\left[\frac{g(\alpha)}{A_\alpha}\right] + \frac{E_\alpha}{RT_{\alpha,i}} \tag{5.18}$$

Where $\tau_{\alpha,i}$, represents the time to reach given reaction extent at different temperature T_i. Eq.(5.18) presents also isoconversional integral method for isothermal conditions, where is determined from the slope of $\ln t_{\alpha,i}$ versus reciprocal temperature, *1/T*, plot. For linear heating rate introduction, the equation (5.17) unfortunately does not have any analytical solution due to the arising of problematic temperature integral *P(E,T)*.

$$g(\alpha) = \frac{A}{\beta}\int_o^{T} exp\left(\frac{-E}{RT}\right)dT = \frac{A}{\beta}\cdot P(E,T) \tag{5.19}$$

Many of the temperature integral approximations resulted in linear equations of the general form:

$$ln\left(\frac{\beta_i}{T^B_{\alpha,i}}\right) = ln\left(\frac{AR}{E_\alpha g(\alpha)}\right) - C\frac{E_\alpha}{RT_\alpha} \tag{5.20}$$

Where *C* and *B* are parameters determined by temperature integral approximation. Solving the temperature integral issue resulted in many approximation formulas, giving birth popular integral isoconversional methods:

Ozawa-Flynn-Wall (OFW)

$$ln\left(\beta_i\right) = ln\left(\frac{AE_\alpha}{Rg(\alpha)}\right) - 5.3305 - 1.052\frac{E_\alpha}{RT_\alpha} \tag{5.21}$$

Where Doyle approximation was implemented with $B = 0$ and $C = 1.052$ and intercept value -5.3305 [132].

Kissinger-Akahira-Sunose (KAS)

KAS method offered another popular approximation of *P(E,T)* with Murray and White formulas, with $B = 2$ and $C = 1$ [110].

$$ln\left(\frac{\beta_i}{T_{\alpha,i}^{\ 2}}\right) = ln\left(\frac{AR}{E_\alpha g(\alpha)}\right) - \frac{E_\alpha}{RT_\alpha} \tag{5.22}$$

Pre-exponential factor estimation

The accurate way to determine the values of actual pre-exponential factors A_α without the assumption of any reaction model was developed based on the use of the compensation effect [110,133,134]. The kinetic compensation effect is a linear correlation that is known to exist between any set of Arrhenius parameters $\ln A_j$ and E_j. Fitting the calculated values of $\ln A_j$ and E_j *e.g.*, by a Friedman method, to a straight line (5.16) allows to estimate compensation parameters values, *a* and *b*:

$$ln\, A_j = aE_j + b \tag{5.23}$$

Even if the set of $\ln A_j$ and E_j values does not include the correct values, the latter still lies on the straight compensation line. As isoconversional methods are known to give correct values of the apparent activation energy, substitution of E_α into Eq.(5.23) returns accurate values of $\ln A_\alpha$ [133,134].

Isoconversional reaction model

When both A_α and E_α are known one can simply reconstruct actual reaction model profile governing investigated process by introduction of E_α and A_α to Eq.(5.24), what is a significant novelty within the field of biomass pyrolysis (or even combustion) kinetics [110].

$$f(\alpha) = \frac{\left(\frac{d\alpha}{d\tau}\right)_\alpha}{A_\alpha \exp\left(\frac{-E_\alpha}{RT}\right)} \tag{5.24}$$

Isoconversional approach to pyrolysis rate modelling

Having isoconversional kinetic triplets, specific for each feedstock pyrolysis and oxy-fuel combustion, one can approach modelling the rate of the investigated processes, being the main hypothesis of the proposed research summarized by the Eq.(5.25).

$$\frac{d\alpha}{d\tau} = A_{\alpha} \exp\left(\frac{-E_{\alpha}}{RT}\right) f(\alpha) \tag{5.25}$$

Fit quality of the modelled dα/dτ to experimental values can be evaluated with non-linear R^2. Besides that, each of the isoconversional methods rate model will be compared using the Fisher-Snedecor test, comparing models standard deviation estimates in comparison to critical F-distribution at selected confidence interval, usually >90%. Fisher-Snedecor test already proved to be a popular tool for comparison of different kinetic models established by the least square method [109,112]. For a brief review, F-distribution is a non-symmetrical distribution that compares the two estimates of models standard deviations, σ^2. F value for tested models is a ratio of its variance estimates related to minimum variance estimate denoted within the tested.

$$F = \frac{S_i^2}{S_{\min}^2} \tag{5.26}$$

where S^2_j and S^2_{min} represent the variance estimates for each model and minimum value from population respectively. Models presenting F value higher than critical F-distribution are rejected from further calculations, as their variance is unacceptable, too high to fulfill the zero-hypothesis at selected confidence interval. Finally, the selected statistical methods will help to answer the question: are isoconversional methods competitive in rate modelling compared to model-fitting methods, and which method provides the lowest deviations from experimental data?

5.2.5. Understanding variable activation energy E_{α}

Variable activation energy, *i.e.*, the activation energy that varies with temperature and/or conversion, would be much easier to appreciate, if it were not for that popular graph *of the ball on the hill* found in undergraduate general or physical chemistry texts in sections dealing with kinetics or, more specifically, with the activated-complex theory [105]. Provided simplification may be appropriate only for homogenous gas-phase reactions and unfortunately is of little relevance to solid-phase and heterogeneous kinetics. Regarding

solid-phase kinetics, the processes take place in the solid medium. In this situation, the energy barrier becomes dependent on the properties of the medium, thus the size of the barrier may thus change as the properties of the medium change with either temperature or reaction progress. An appropriate illustration was given by S. Vyazovkin, with an example of a single-step reaction A → B such as isomerization. In general, the energetic state of the reactant A is affected by the molecules that surround it. At the early stage of the reaction, when α is close to 0, the reactant is surrounded by other molecules of A. As the reaction nears completion, *i.e.*, α is close to 1, the reactant will be predominantly surrounded by the product molecules B. If intermolecular forces between A and A are stronger than the forces between A and B, the molar enthalpy of A will be lower in initial ($\alpha = 0$) than in final ($\alpha = 1$) stages of the reaction. By similar argument, in the final stages ($\alpha = 1$) when the product B is surrounded by the molecules B, its molar enthalpy is lower than in the initial stages of reaction ($\alpha = 0$). Obviously, as this reaction progresses from $\alpha = 0$ to $\alpha = 1$, its exothermal character should increase and its energy barrier should decrease. In other words, the observed activation energy should progressively decrease as a function of conversion, α. In case of pyrolysis, and biomass thermochemical conversion in general, differentiation of specific reactants as A or B is cumbersome. First, the biomass represents a variety of different organic materials, highly heterogenic, and often non-lignocellulosic. This complexity led to the widely accepted conclusion that during thermal decomposition biomass components decompose separately, according to the independent reaction mechanism [34,135]. Having that in mind, the E_α profile obtained for complex material decomposition can give valuable information about the process behavior and even process mechanism [108].

5.2.6. Comparing the model-free, isoconversional and model-based kinetics

During numerous occasions including discussions, conferences, papers reviews and presentations the one thing that especially often occurs is misunderstanding of the terms model-free and isoconversional kinetics. The difference can be misleading for any audience, and further can lead to misunderstandings or even more unpleasant repercussions addressing experienced chemical-engineering society. The term *model-free* relates to any kinetic method that allows to estimate the activation energy E without reaction model assumptions $f(\alpha)$. Kissinger method is a good representative of the model-free kinetics, whereas the E is estimated from the regression parameters of the straight line led trough the maximum conversion rate points (peaks) over reciprocal temperature $1/T$, for several heating runs. Simplicity of implementation, and ease to obtain straight-forward value of E led this method to popularity in kinetic literature of the waste biomass. However, due to the limitation of calculation to only $d\alpha/d\tau$ peak-points, the Kissinger method generally should be avoided in complex bio-material pyrolysis modelling due to significant deviations in the

obtained results. *Isoconversional* kinetics principle is based on analyzing the whole conversion range, not only conversion rate peaks, so the outcome of the computations is complex profile of the activation energy as a function of α, thus the isoconversional (or apparent) activation energy E_α. Having accurate profile of the E_α allows to gain insight into the process mechanism, reaction model or even attempt to model the process rate with adequately decrypted pre-exponential factor *A*. *Model-based* kinetics are based on the reaction model assumed beforehand. Of course, the choice of the $f(\alpha)$ function strongly influences the rest of the kinetic parameters. On the one hand, variety of the reaction models chosen results in ambiguities of the kinetic parameters describing biomass pyrolysis in the literature, on the other hand, model-based allows to determine elementary reactions of the investigated process, providing arguable superiority over isoconversional methods in that case. For model-free approaches, the change of the kinetic mechanism is described by the continuous changing of the activation energy and the pre-exponential factor with the progress of the reaction. For model-based approaches, the change of the kinetic mechanism is described by appearing of several reaction steps with own activation energy and with own reaction model functions. Interestingly, superiorities and inferiorities of the model-based and isoconversional methods seems to be a subject of discussion, where one tries to prove or justify a better or more appropriate (or traditional) method to evaluate processes kinetics. Within presented dissertation, rather than promote pros and cons of different kinetic approaches, a supplementary value of both model-free, isoconversional and model-based methods combined is presented. Isoconversional parameters determination is much more than "*art for art's sake*", what can be sometimes concluded from scientific papers presenting isoconversional results for specific biomass decomposition motivated by "enriching pyrolysis kinetic parameters database". Isoconversional profiles of E_α, and A_α can provide initial values for the model-based computations, where starting values of *E*, *A*, and $f(\alpha)$ functions are usually assumed arbitrary. Average values of the E_α, and A_α profiles can well substitute traditional Arrhenius parameters in model-based analysis, and usually are in well agreement with each other. Regarding reaction model functions, simple methods were developed to determine the most probable $f(\alpha)$ for the investigated process based only on E_α and experimental process rate $d\alpha/d\tau$, the master-lot (generalized-plot) methods.

5.2.7. Master-plot methods and problems with pyrolysis reaction models identification

The generalized master plot, $\lambda(\alpha)$, is an analytical method of theoretical reaction model plots fitting to thermoanalytical data. However, some assumptions should be stated beforehand: the reaction or process is perceived as a single-step process; isoconversional activation energy must be known and should not deviate significantly across the reaction extent to provide meaningful conclusions. The idea of the presented method is a comparison

of experimental generalized rate plot, being the results of the simple transformation of kinetic rate equation Eq. (5.4), referred to rate at α=0.5 to theoretical reaction model plots (Fig. 5.1).

$$\lambda(\alpha)=\frac{f(\alpha)}{f(0.5)}=\frac{\left(\frac{d\alpha}{dt}\right)_{\alpha}}{\left(\frac{d\alpha}{dt}\right)_{\alpha=0.5}}\cdot\frac{\exp\left[\frac{(E_{\alpha})_{avg.}}{RT_{\alpha}}\right]}{\exp\left[\frac{(E_{\alpha})_{avg.}}{RT_{\alpha=0.5}}\right]} \tag{5.27}$$

Eq. (5.27) presents a procedure for generalized reaction rate calculation, where variables are experimental conversion profiles and temperature. Literature data proves that biomass pyrolysis presents deaccelerating behavior during decomposition with *e.g.*, diffusion-controlled models for the lignocellulosic biomass [34,78,112] or n^{th} order models for the sewage sludge [121,136]. More and more popular are empirical and combined reaction models [137], with a high degree of freedom within an *f(α)*, however, despite excellent fit to experimental data, Arrhenius parameters physical meaning is highly arguable due to significant correlations during optimization with empirical *f(α)* parameters.

Fig. 5.1 presents *λ(α)* and *f(α)* profiles for the most widely used reaction models in solid-state decomposition kinetics. In theory, experimental generalized rate of the process obeying a specific reaction model *e.g.*, contracting sphere model (R2) or three-dimensional diffusion (D3), should present exemplary and unambiguous fit to its theoretical master plot, what unfortunately rarely happens for biomass pyrolysis. Exact formulas for *f(α)* profiles with model names and codes are presented in Table 9.

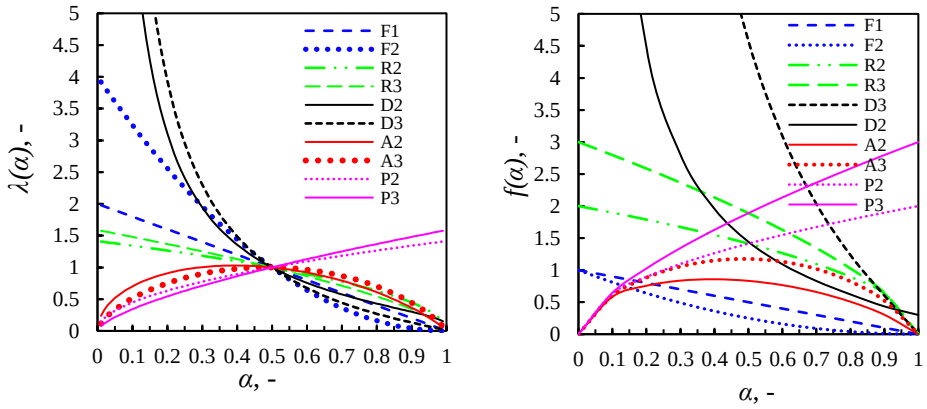

Fig. 5.1. λ(α) and f(α) profiles for known reaction models.

Table 9: List of the selected reaction models *f(α)* used in the solid-state kinetics.

Code	Model name	*f(α)*
F1	1st order reaction model	$(1-\alpha)$
F2	2nd order reaction model	$(1-\alpha)^2$
R2	Contracting cylinder	$2(1-\alpha)^{1/2}$
R3	Contracting sphere	$3(1-\alpha)^{2/3}$
D3	Three-dimensional diffusion	$3/2(1-\alpha)^{2/3}[1-(1-\alpha)^{1/3}]^{-1}$
D2	Two-dimenstional diffusion	$[-ln(1-\alpha)]^{-1}$
A2	Avrami-Erofeev	$2(1-\alpha)[-ln(1-\alpha)]^{1/2}$
A3	Avrami-Erofeev	$3(1-\alpha)[-ln(1-\alpha)]^{2/3}$
P2	Power law	$2\alpha^{1/2}$
P3	Power law	$3\alpha^{2/3}$

5.2.8. Current trends in kinetic modelling of the solid-phase reactions and importance of the kinetic parameters determination.

Biomass and waste thermal conversion kinetics are a subject of heated debates, mainly due to numerous adaptations of homogenous kinetic theory to highly heterogenic and diversified feedstock degradation modelling [138]. A traditional approach to kinetic analysis is based on the determination of Arrhenius parameters i.e., activation energy, *E*, and pre-exponential (frequency) factor, *A*, biased with pre-assumption of the reaction model function *f(α)* [118,139]. Based on experimental conversion rate profiles, dα/dt, obtained for several heating or temperature programs, Arrhenius parameters can be determined using numerical fitting techniques involving least squares method, genetic and neural algorithms [140–142]. However, assumptions of different *f(α),* for kinetic computations result in different sets of Arrhenius parameters, even for the very same investigated process [107,109].

These discrepancies ad contradictions are particularly evident in biomass and waste thermal degradation kinetics studies, where researchers investigating highly overlapped conversion profiles lean towards *f(α)* with a high degree of freedom, compensating kinetic parameters even more, yet provide a satisfactory fit to experimental data [78]. Second popular route is to assume a high number of elementary reaction steps "filling" somehow the complex profiles [126,129]. The inability of known *f(α)* to explicitly describe the more and more complex feedstock degradation led the researchers to

investigate new kinetic approaches and methods. This issue seems to be overcome with the introduction of isoconversional kinetics for pyrolysis kinetic modelling [131,143,144]. Isoconversional kinetics allow avoiding the huge uncertainty due to omission of *f(α)* assumptions, yielding the conversion dependent profiles of activation energy, and even the information about pre-exponential factors and reaction models [110].

Implementation of the isoconversional principle in practice, originated a number of isoconversional methods, ready to yield profiles of apparent activation energies, E_α, as a function of reaction extent (or converted fraction) α. Originally, the isoconversional kinetics were successfully used in applied physical chemistry, to study and recognize complex processes *e.g.* crystallization, polymerization and polymers degradation, glass transition, or curing [125,145–149]. According to latest work of S. Vyazovkin, isoconversional methods are merely a part of wide isoconversional methodology, ready to provide more kinetic answers [110]. Bedoić [123] and Sobek [112] published the results of isoconversional rate modelling of roadside grass and waste wood pyrolysis respectively, however with the implementation of so-called modified pre-exponential factors, being a correlated product of *A* and *f(α)*, obtained by isoconversional Friedman method. Isoconversional kinetics proved to be a great support for model-fitting kinetics, where the apparent profiles of E_α contain kinetic information about the reaction mechanism or even a specific number of elementary steps [108]. Mean values of E_α are successfully used as initial guess values for optimization of kinetic models in model-fitting kinetics [112,124,126], proving another example of isoconversional kinetics supplementary value. In another work of Sobek and Werle [112] took this approach to assist model-fitting method with isoconversional kinetics, taking into consideration actual gas evolving species during solar pyrolysis experiments for elementary pyrolysis steps modelling, detected on a gas analyser, modelling waste wood pyrolysis. This experience was transduced to another example isoconversionally-assisted modelling of sewage sludge pyrolysis rate by Sobek and Werle, and resulted in excellent fit to experimental data, where Friedman method gave even better kinetic predictions comparing to 10 independent reactions kinetic model based on n^{th} order reaction *f(α)* [121]. Regarding combustion processes, Lopes et al. [117] presented a study on kinetics of guarana seed residue applying isoconversional methods, resulting in a recognition and creation of consecutive reaction scheme with first-order (F1) and two-dimensional diffusion models (D2). Nevertheless, in most of the studies, researchers publishing isoconversional results usually provide information about apparent activation energies, and its interpretation for pyrolysis [132,150–153], leaving behind a 2/3 of the potential kinetic triplet. Based on knowledge of apparent activation energy profiles, the apparent pre-exponential factors can be determined using linear compensation effect, happening between the two Arrhenius parameters [133,134,145]. Not only that, a concept of determination of derivative reaction models is proposed within this project, being a theoretical profile of actual, resultant *f(α)* values occurring throughout the conversion, therefore a whole kinetic triplets, what best to Authors knowledge, has not been published for pyrolysis process of waste yet [110].

In terms of kinetic modeling of lignocellulosic biomass pyrolysis, researchers usually lean towards three pseudo-component models [84] and more extend reaction schemes [154]. This approach correctly assumes that pyrolysis reaction is a decomposition of three main plant components: cellulose, hemicellulose, and lignin [106]. In this model, the kinetic parameters are established using different optimization methods to provide the best statistical model fit to experimental data, without actual consideration of the products, where the kinetic parameters describe the kinetics of substrates decomposition. According to Li et al. [155], cellulose during pyrolysis decomposes in the temperature range 240-350 °C while hemicellulose decomposes earlier, in the range 200-260 °C, resulting in the characteristic shoulder of differential TGA peak. Lignin is more difficult to dehydrate due to its physical and chemical properties, it decomposes in the temperature range 280-500 °C. R. Li et al. in 2016 [155] established, that on the one hand, cellulose turns generally into condensable vapor (oil) during pyrolysis, whereas in contrast, hemicellulose produces more non-condensable gas and fewer tars. On the other hand, lignin degrades slowly and forms char, the carbon-rich residue. Charring reaction is especially an interesting reaction in terms of kinetic parameters and overall thermodynamic behavior. At temperatures above primary pyrolysis (250-400 °C), a mass drop of samples drastically slows down and even flattens to a constant level corresponding to a final solid residue yield. In order to get information about actual reactions occurring during the char formation period, one should analyze gaseous products released from the reaction zone at this specific time and temperature.

Regarding already published studies, in 1997 G.Vatirhegyi [85] presented paper on kinetic modeling of biomass pyrolysis addressing issues, that are still present today. Highlighted issues were *e.g.*, least square method optimization, biomass component impact on decomposition, pseudo-order component models, the effect of mineral catalysts or the Boido-Shafizadech model for cellulose decompositions. Especially interesting conclusion was that the presence of minerals salts in biomass ashes directs cellulose decomposition towards lower temperatures, overlapping its peaks with hemicelluloses profiles, what is especially visible in today's studies, with soils contamination progress [36]. Another example of heavy metals impact on plant behavior during pyrolysis was the topic of Trinh phytoremediation study in 2019 [84], where results showed that samples collected from different presented different TGA profiles at same temperatures regarding peak areas and overlapping intensity. Also, investigated samples pyrolysis kinetics were modeled in three pseudo-component manners, adapting n^{th} order reaction model $f(\alpha)=(1-\alpha)^n$ with reasonable reaction orders within 1.01-1.99 and activation energies 20-103.55 kJ/mol, however rather poor fit to experimental data was achieved. On the other hand X. Wang [137] et al. in 2016 studied agricultural residue biomass pyrolysis with an adaptation of combined kinetics. Combined kinetics are based on empirical reaction model (modified Šesták-Berggren) $f(\alpha)= \alpha^m(1- \alpha)^n [1-ln(\alpha)]^p$ determination using isoconversional analysis results. Despite arguable physical meaning and rather surprising mechanistic conclusions, authors achieved spectacular fit to experimental data, optimizing the model parameters (*n*, *m*, *p*) and kinetic

parameters by maximizing the Pearson's *r* of linear regression for single-step approach, later used as initial parameters for three-component model optimized by nonlinear least squares. Again, study did not evaluate pyrolysis products. In 2015 Z. Ma et al. [156] investigated lignocellulosic biomass pyrolysis (palm kernel shell) using TGA-FTIR and FWO and KAS integral methods. E_α conversion dependency was associated with temperature regiemes of biomass components pyrolysis. T Study was supported with separated TGA analysis of each of biomass components. Two-step decompositon of cellulose was highlighted, simmilarily to [85]. The major volatile components produced during pyrolysis of palm kernell shells were CO_2, ketones, alkanes, aldehydes, phenols and organic acids, however no reaction model describing species reaction rates was establised.

Regarding sewage sludge pyrolysis kinetics, Naqvi et al. [157] investigated high-ash SS pyrolysis at different heating rates 5,10 and 20 K/min, using an arguable Coats-Redfern integral method. The mentioned study divided sewage sludge pyrolysis into three zones that were described best by the first-order reaction model. The study reported a high dependence of sewage sludge mass loss on the heating rate, which despite well-separated reaction peaks disqualified model-free, isoconversional approach. Another study published by Naqvi et al. [141] was aimed for high-ash SS pyrolysis as well, addressing thermodynamic parameter estimation based on model-free, isoconversional kinetics using Friedman, KAS, OFW and Popescu methods. Results were compared to literature data and an artificial neural network model was created to make mass-loss predictions under different thermal conditions. Shahbeig and Nosrati [158] presented a study of municipal sewage sludge for bioenergy production. In their paper, sewage sludge samples were examined during TGA at four different heating rates 5, 10, 30 and 50 K/min. Sludge pyrolysis kinetics were evaluated using FWO, KAS and Starnik methods. Furthermore, Pyrolysis–Gas Chromatography/Mass Spectroscopy (Py-GC/MS) at 700 °C to determine the chemical products, indicated the presence of a wide range of aromatic and aliphatic hydrocarbons, furans, alcohols, and sulfur-derived compounds. Hernández et al. [34] studied behavior of 25 mg sewage sludge samples during thermochemical conversion, under different atmospheres (N_2, CO_2 and air), using TGA-FTIR methods. Addressing inert gas experiments, denoted sewage sludge mass loss profiles were again separated into three stages, however sludge presented different behavior during pyrolysis than previously cited, and one investigated in the present study. Examined sewage sludge was sampled from the East Rand Water Care Association (ERWAT) Hartebeestfontein WWTP.

5.2.9. Kinetic predictions

ICTAC Kinetics Committee recommendations advise to validate kinetic computations via isothermal lifetime predictions being the predicted time dependence of feedstock converted fraction $\alpha(\tau)$ based on non-isothermal data [104,105,110]. Eq. (5.28)

presents the formula for model-free, isoconversional predictions, which for prediction of time needed to convert a specific fraction of fuel at specific heating conditions specified by the investigator $\underline{T'(\tau)}$, with corresponding specified heating rate β'. To calculated time needed to reach specific conversion level one needs only to calculate isoconversional activation energy, E_α, and time necessary to reach that same fraction determined at previous experimental runs, τ^* [109]. The model-free term originated from cancellation of the integral reaction model form $g(\alpha)$ from the nominator. Main justification of the mentioned action is the assumption that the isoconversional kinetic triplets do not change over the extrapolation range.

$$\tau'_{\alpha,i} = \frac{\int_{\tau^*_{\alpha,i-1}}^{\tau^*_{\alpha,i}} \exp\left(\frac{-E_{\alpha,i}}{RT(\tau)}\right) d\tau}{\beta' \exp\left(\frac{-E_{\alpha,i}}{RT(\tau)}\right)} \tag{5.28}$$

5.2.10. Calculation details and chosen statistical methods for models evaluation

Kinetic computations were conducted using Netzsch Kinetics Neo (v. 2.4.4.6.) software. First, isoconversional analysis was performed using TGA results presented in each specific part of the dissertation. Kinetics Neo uses decimal logarithm in isoconverisonal analysis instead of the standard natural logarithm, so it has to be taken into account when calculating kinetic parameters from slope and intercept of isoconversional lines. No data smoothing was used during TGA data preparation. During kinetic analysis moisture evaporation was skipped, and pyrolysis range from 150 to 700°C was analyzed. Next, the reaction model analysis using a generalized master-plot method was conducted.. Netzsch Kinetics Neo uses, least squares method to search for optimization of kinetic parameters to get the best coefficient of determination, R^2 of calculation to experiment results. Kinetic parameters range of variation was set to $E \in (0;300)$ kJ/mol, $\log(A) \in (0;30)$. As the least-squares method was adapted for kinetic models optimization *F-test* (Fisher-Snedecor) was chosen as a statistical test amongst the models and additionally to test model-free methods.

Within the statistical analysis, coefficient of determination R^2, residual sum of squares, S^2, and *F-test* were calculated and tested against critical *F*-distribution for a right tail *p-value* of 0.05. The coefficient of determination definition is well known. The S^2 is calculated as the sum of deviation squares Eq. (5.29) between experimental and calculated data. If the experimental data y_j measured at the points x_j for the curve i, and the model function $f(x)$ is calculated at these points, then the regression values are $f(x_j)$. The residual

between the experimental value and model value for i^{th} curve is $y_{i,j} - f(x_{i,j})$, therefore S^2 can be expressed as:

$$S^2 = \sum_{i}^{Curves} \sum_{j}^{Points} \left[y_{i,j} - f(x_{i,j}) \right]^2 \tag{5.29}$$

F-test proved to be a good tool for comparison of different models established by the least square method [109]. F distribution is a sampling, non-symmetrical distribution that describes the distribution of the ratio of two estimates of standard deviations, σ_2 [159]. *F* value for each analyzed model presents a ratio of its variance estimates (or variance if it's known) related to minimum variance estimate denoted in the tested population as Eq.(5.30). Only models with *F-test* values within the range of critical *F distribution* should be taken into consideration as presenting S^2_j adequate for assumed 95% confidence interval for the study. Models with higher values of *F* give a reason to reject the null hypothesis, stating about equality of standard deviations between *j* and $_{min}$ model, thus such models should be rejected. With the introduction of S^2, the formula for Fisher-Snedecor test, or simply *F-test*, can be expressed as:

$$F = \frac{S^2_{\ j}}{S^2_{\ \min}} \tag{5.30}$$

wherein S^2_j and S^2_{min} represent the variance estimates of $\sigma^{\ 2}_{\ j}$, $\sigma^{\ 2}_{\ min}$ for each model and minimum value from population respectively.

The Mean Residual (MR) is calculated as the average of the absolute residuals Eq. (5.31). If the experimental data y_j measured at the points x_j for the curve $_i$, and the model function $f(x)$ is calculated at these points, then the regression values are $f(x_j)$. The residual between the experimental value and model value for the i_{th} curve is $y_{i,j} - f(x_{i,j})$. The Mean Residual is given as:

$$MR = \frac{\sum_{i}^{Curves} \sum_{j}^{Points} \left| y_{i,j} - f(x_{i,j}) \right|}{\sum_{i}^{Curves} nPoints_i} \tag{5.31}$$

Where $nPoints_i$ are the number of points in the i^{th} curve.

If the model curve is drawn exactly through the experimental points, then all residuals are zero and MR is zero, too. The closer the calculated model curve is to the experimental data, the closer is MR to zero.

6. Results

6.1. Investigated feedstock pyrolysis behavior during TGA

Decomposition behavior of investigated feedstock with plotted as temperature dependency of mass loss and conversion rate is presented in Figs. 6.1-6.3. Average denoted mass loss during TGA was 83.04±0.54 %, 74.6±0.56, and 59.1±0.59 for WW, WS, and SS respectively, which low deviations under a range of heating rates favour isoconversional kinetics calculations. Fig. 6.1 presents the mass loss profile and conversion rate for SS pyrolysis, presenting similar patterns reported in SS pyrolysis literature with high peaks overlap and no clear separation between the pyrolysis steps. The first peak of the decomposition rate occurs at 100 °C identified as moisture release, being immediately followed by another overlapped peak at around 150°C. For SS the main pyrolysis decomposition starts at 200 °C with wide and noisy maximum from 300-350 °C. Later decomposition slows down as clear shoulder approaching minimum rate at 600 °C. This behavior is typical for SS is a very chemically complex and heterogenic feedstock [160]. A high number of peaks and overlapping character of conversion rate profiles is an indication of numerous reactions occurring during the pyrolysis. Usually, each reaction can be expressed by a single rate Eq. (5.4) if only the step can be identified well. Isoconversional kinetics results are popular thread amongst literature on SS pyrolysis, however with limited information about reverse-fitting to experimental conversion profiles [141,151]. Lignocellulosic biomass, on the other hand, WW (Fig. 6.2) and WS (Fig. 6.3) presents well-separated moisture release step with a high and steep peak of primary devolatilization (cellulose pyrolysis) at 329-394 °C for WW (at 5-40 K/min) and 291-351 °C for WW and WS respectively. It should be stated that both WW and WS decomposition is progressing much “faster” through the time and conversion than SS. Maximum peaks of decomposition are 44.03, 40.33, and 17.07 %/min for WS, WW, and SS respectively. Pyrolysis of WW at lower heating rates presented better separation of hemicellulose peaks with shifting towards lower temperatures. Lignocellulosic biomass pyrolysis kinetics are well explained and known by this time, however, to test proposed methods comparative evaluation of calculations according to different biomass types is crucial.

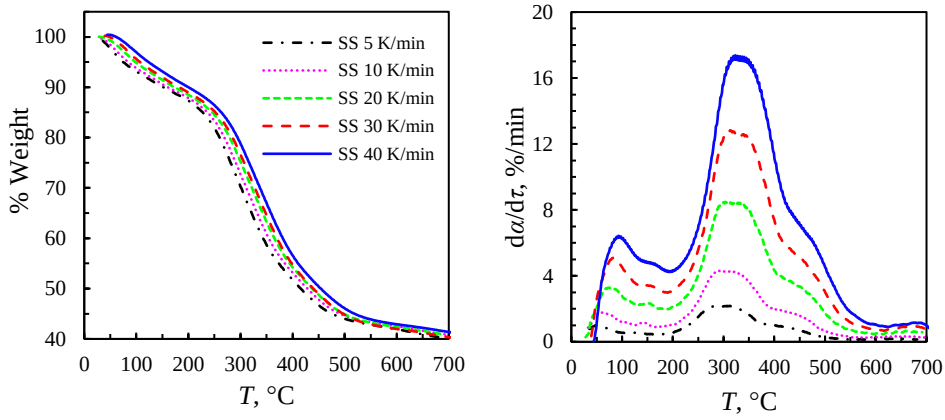

Fig. 6.1. TGA and conversion rate profiles for SS pyrolysis.

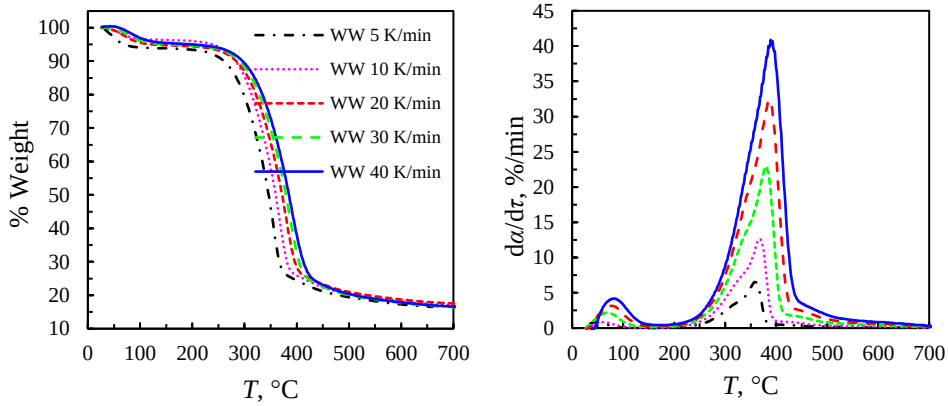

Fig. 6.2. TGA and conversion rate profiles for WW pyrolysis.

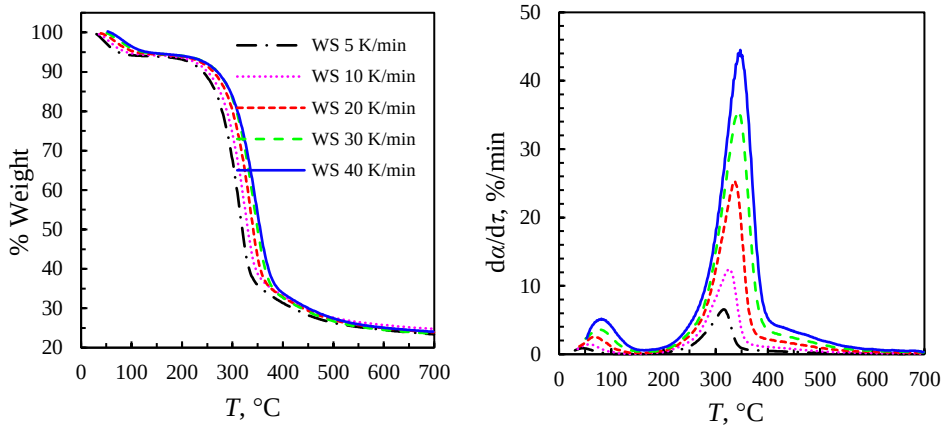

Fig. 6.3. TGA and conversion rate profiles for WS pyrolysis.

6.2. Model-based kinetics of the waste wood pyrolysis

The idea of the study originated from conclusion of the very first preliminary experiments on the solar pyrolysis reactor. Simultaneously to TGA measurements of the WW, actual composition of the dry-pyrolysis gas was determined experimentally for its general and crude recognition. Denoted similarities in obtained conversion rates and gas formation profiles gave the idea to try to construct a kinetic mechanism inversely, with assumption of the specific dry gas components formations as elementary pyrolysis steps. This *experimental* approach was later compared to the traditional *three-pseudo components* modelling calculated for the same set of TGA data, and discussed. Also, supplementary value of the isoconversional kinetics as a source of initial kinetic parameters for further model-based computations is presented.

6.2.1. Isoconversional methods as a source of initial parameters for kinetic computations

As a first step of the study, TGA profiles of the WW pyrolysis were implemented to the Netzsch Kinetics Neo software for comparative evaluation of the three isoconversional methods results: Friedman, OFW, and KAS. Starting from the three methods, to improve the calculation efficiency, the most adequate method was specified, under condition of the lowest deviations of the results from the experimental data. Solutions of each method equations resulted in series of isoconversional points (Fig. 6.4), which regression parameters *i.e.* slope and intercept, presented in Table 10, contained information about apparent kinetic parameters.

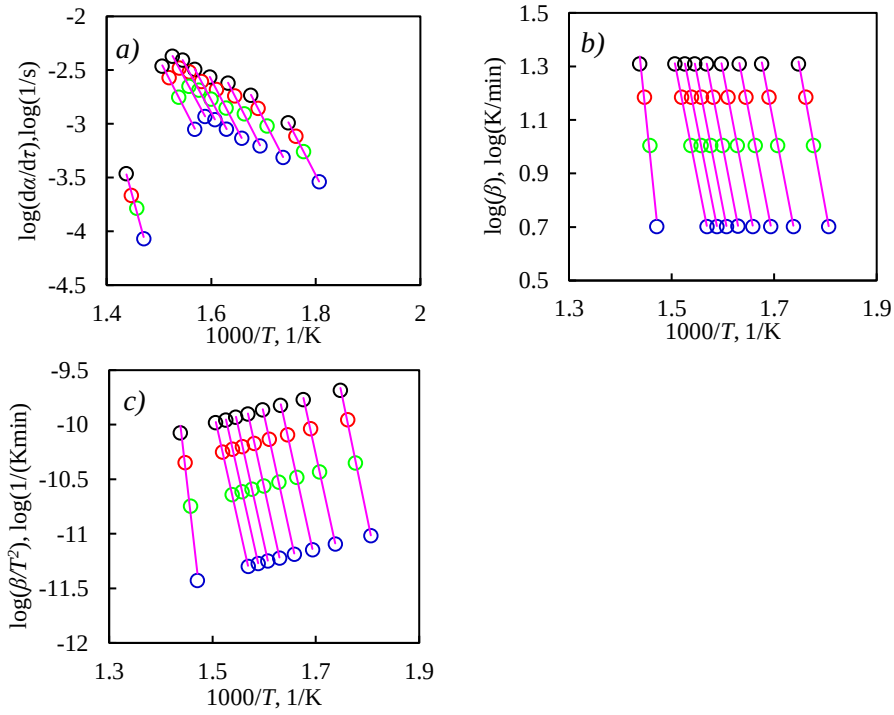

Fig. 6.4. Isoconversional analysis plots for a) Friedman, b) OFW and c) KAS methods. (5 K/min blue, 10 K/min green, 15 K/min red, 20 K/min black) orientated to the decimal logarithm.

Table 10: Selected isoconversional linear fitting results.

Friedman				OFW				KAS			
α	*Slope*	*Intercept*	R^2	*α*	*Slope*	*Intercept*	R^2	*α*	*Slope*	*Intercept*	R^2
0.1	-9.3720	13.393	0.9995	0.1	-10.472	19.619	0.9974	0.1	-22.987	30.506	0.9972
0.2	-9.4289	13.073	0.9997	0.2	-9.9332	17.963	0.9995	0.2	-21.701	26.616	0.9994
0.3	-9.5287	12.935	0.9993	0.3	-9.9415	17.539	0.9998	0.3	-21.689	25.587	0.9997
0.4	-9.3431	12.361	0.9999	0.4	-9.9736	17.143	0.9998	0.4	-21.737	24.863	0.9998
0.5	-9.1545	11.869	0.9999	0.5	-9.9457	16.911	0.9999	0.5	-21.651	24.064	0.9999
0.6	-8.9668	11.451	0.9999	0.6	-9.8521	16.536	0.9999	0.6	-21.417	23.172	0.9999
0.7	-9.0233	11.402	0.9999	0.7	-9.7518	16.193	0.9999	0.7	-21.171	22.356	0.9999
0.8	-9.4725	11.814	0.9990	0.8	-9.7540	16.006	0.9999	0.8	-21.159	21.9	0.9998
0.9	-17.720	22.010	0.9863	0.9	-18.500	27.939	0.9842	0.9	-41.222	49.266	0.9831

Isoconversional methods resulted in apparent activation energy conversion dependence, E_α, shown in Fig. 6.5. Presented conversion profile of the apparent activation energy for wood pyrolysis analyzed at full TGA profile range, including moisture evaporation and the full charring period until the end of the experiment. First activation energies are related to the moisture release process which after approaching zero values steps aside and pyrolysis effects are becoming dominant. It can be seen, that all investigated methods results reached a plateau from α=0.15 to 0.85 at around 170-180 kJ/mol value of activation energy. Enormous activation energy increase at α>0.85 can be explained by the noisy character of TGA profiles at charring period of pyrolysis experiments or reactions occurring in mineral ash residue, thus it is recommended to present model-free activation energy results at α=~0.1 to 0.85 [104], usually where the lowest standard deviations are present. Presented E_α values correlate well with recent literature data. Sonobe et al. [106] investigated biomass pyrolysis by utilizing a distributed activation energy model (DAEM). The peaks of activation energy curve for rice straw, rice husk, corncob, and cellulose were found to be 170,174,183, and 185 kJ/mol, respectively. Rueda-Ordóñez and Tannous [25] studied the kinetics of the thermal decomposition reaction of sugarcane straw. Applying the Friedman method obtained E_α varied from 154.1 kJ/mol to 177.8 kJ/mol. In the case of woody biomass, Mishra and Mohanty [129] investigated pyrolysis kinetics of three waste biomass types: pine, sal, and areca nut. Five model-free methods such as KAS, OFW, Friedman, Coats-Redfern, and distributed activation energy (DAEM) were used to calculate the kinetic parameters. The activation energy was determined to be 171.66 kJ/ mol, 148.44 kJ/mol, and 171.24 kJ/mol from KAS model; 179.29 kJ/mol, 156.58 kJ/mol, and 179.47 kJ/mol from OFW model; 168.58 kJ mol, 181.53 kJ/mol, and 184.61 kJ/mol from Friedman

model; and 206.62 kJ/mol, 171.63 kJ/mol, and 160.45 kJ/mol from DAEM model for pine, sal, areca nut respectively.

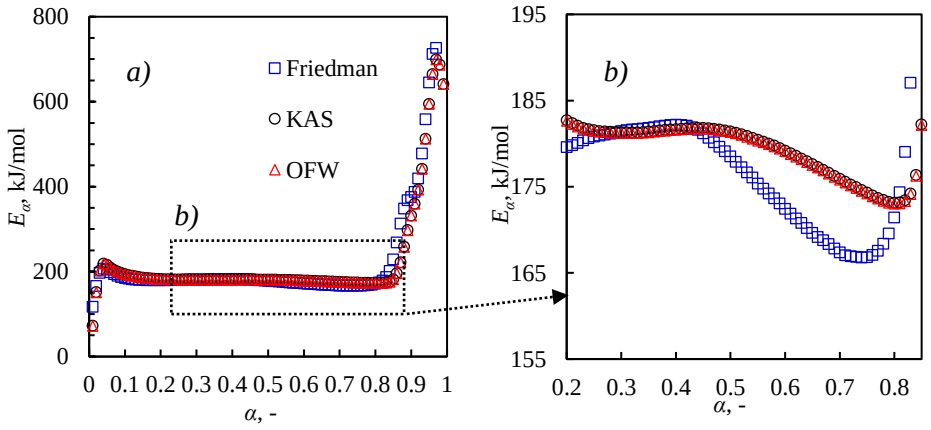

Fig. 6.5. Apparent activation energy conversion dependence for Friedman, KAS, and OFW methods for the WW pyrolysis.

Right hand-side of Fig. 6.5a shows up-close look to activation energy conversion dependence scaled to an average range of E_α at conversion α=0.2 to 0.85. Despite a plateau and almost constant values of E_α, the close look shows the complexity of the pyrolysis process and possible reaction mechanism as a variation on E_α across the conversion range.

Table 11: Apparent activation energies calculated using Friedman, KAS, and OFW methods.

Conversion	Friedman		KAS		OFW	
	E_α, kJ/mol	±Error, kJ/mol	E_α, kJ/mol	±Error, kJ/mol	E_α, kJ/mol	±Error, kJ/mol
0.1	185.37	3.95	194.35	6.32	194.29	6.63
0.2	179.61	1.61	182.74	2.56	182.66	2.72
0.3	181.46	1.58	181.31	1.81	181.23	1.94
0.4	182.20	0.76	181.69	1.44	181.60	1.56
0.5	178.54	0.28	181.43	0.83	181.34	0.92
0.6	172.45	1.50	179.20	0.54	179.11	0.61
0.7	167.37	3.53	175.91	1.15	175.81	1.26
0.8	171.45	8.75	173.14	2.86	173.04	3.08
0.9	375.56	29.69	331.75	32.19	331.69	33.26
Average (0.1-0.9)	199.33	5.74	197.95	5.52	197.86	5.77

Based on Table 11 it can be stated that all investigated model-free methods provided similar results. According to Fig 6.5, apparent activation energy presented stable plateau throughout the pyrolysis extent, with a significant increase at α=0.9, denoted by all isoconversional methods. This phenomenon is widely reported in the literature and usually commented with highly endothermic charring reactions, resulting in a high increase in apparent activation energy. Regarding fit quality to experimental data, statistical analysis results were presented at the end of the Chapter in Table 8, and the Friedman method was selected as the best description of waste wood pyrolysis in selected heating rates range amongst investigated model-free methods. Friedman method presented the lowest sum of residuals squares, resulting in the lowest value of the *F-test* compared to KAS and OFW methods. The reason why integral methods can present high deviations (residual squares) are several: first reason can be a crude approximation of temperature integral, second can be the nature of the integral methods itself. As biomass TGA profiles tend to present highly overlapping and noisy character, integral methods evaluate conversion points based on the average heating rate and temperature dependency, β and β/T^2 for OFW and KAS respectively, while differential Friedman method evaluates actual process rate, $d\alpha/d\tau$. Evaluation of process rate is possible to reason why Friedman method accurately evaluate nuances and overlaps of conversion profiles more accurately than integral methods, especially in the case of biomass pyrolysis kinetics. Pre-exponential, or frequency factor was estimated using apparent activation energy obtained through the Freidman method, as it presented the best fit to experimental data with the lowest residual squares during fitting to experimental data), resulting in the lowest F-test value among model-free methods (Table

15). In order to model the conversion rate profile $d\alpha/d\tau$ with isoconversional methodology, some reactin model assumption must be made for the elementary process step, usually 1st reaction order, what is acceptable with regards to the iscovonersional principle given by S. Vyazovkin [105]. With that in mind, the values of conversion dependent pre-exponential factors are calculated from the intercept values (Table 12) using Eq. (5.16) with the assumption of 1st reaction order.

Table 12: Pre-exponential factor conversion dependence calculateed with Friedman method.

Conversion	Log A_α, Log(1/s)	±Error, Log(1/s)	E_α, kJ/mol	±Error, kJ/mol
0.01	8.23	17.89	117.66	167.57
0.05	16.26	0.96	204.37	9.95
0.1	14.01	0.37	185.37	3.95
0.2	13.10	0.14	179.61	1.61
0.3	13.02	0.14	181.46	1.58
0.4	12.88	0.06	182.20	0.76
0.5	12.46	0.02	178.54	0.28
0.6	11.92	0.12	172.45	1.50
0.7	11.48	0.29	167.37	3.53
0.8	11.68	0.70	171.45	8.75
0.9	25.79	2.26	375.56	29.69
0.99	30.22	34.44	562.82	592.61

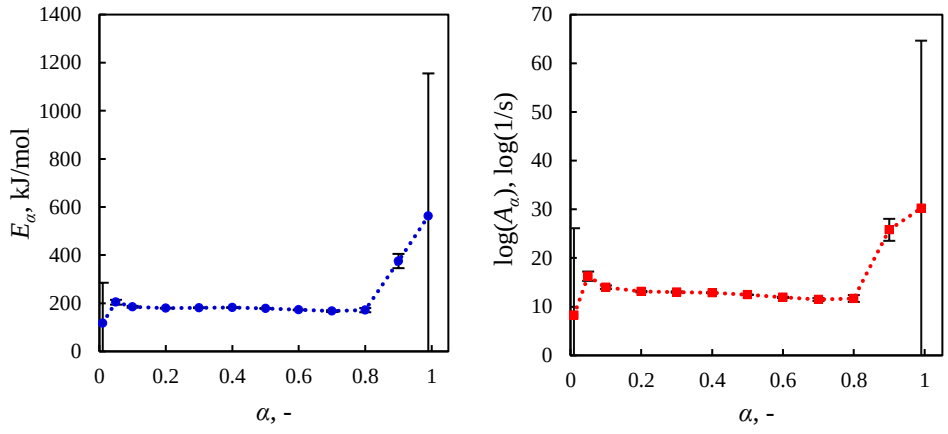

Fig. 6.6. The apparent activation energy (blue) and pre-exponential factor (red) interdependency with related standard errors calculated with Friedman method.

Fig. 6.6 presents a dependency between apparent A_α and E_α determined with the Friedman method for WW pyrolysis. With the assumption of 1st reaction order model, it is obvious that apparent pre-exponential factors will follow the activation energy trend. Sudden increase of apparent kinetic parameters, at the end of conversion, α>0.9, are usually justified as a consequence of noisy character of pyrolysis profiles TGA data at the end of conversion for, or physically as sudden appearance of energy barrier caused by interference of minerals or heavy metals contained in the WW ash along with rearrangement of ether group bonds in lignin. In theory known reaction activation energies vary from 40-50 kJ/mol to approx. 300 kJ/mol, for enzymatic reactions and explosives respectively, and values out of this range can be problematic to justify and defend.

Constant dependence of A_α and E_α means that during the process is governed by one dominant energy barrier followed by one theoretical, pre-exponential factor. In fact, according to Fig. 6.5b presenting up close E_α profile, which proves that in the case of complex materials, like biomass, some E_α fluctuations are almost always present. Changes in activation energy are the first proof that more than one reaction occurs during decomposition [108]. However during the investigated process, at α from 0.2 to 0.8, A_α and E_α reached a relative plateau with a slightly decreasing tendency throughout the selected conversion extent. Presence of model-free kinetic parameters variations the presence of multiple reaction systems. In the investigated α range kinetic parameters were 11.68-14.01 log(1/s) and 174.65- 204.37 kJ/mol for A_α and E_α respectively (Table 12), which reflects well data presented for lignocellulosic biomass in the literature [78,84,161]. Constant, or almost constant, E_α and A_α mean that in theory pyrolysis could be modeled as a single-step reaction with above mentioned kinetic parameters, however, the theoretical reaction model is still unknown. Despite that fact, Friedman's method based on apparent activation energy and pre-exponential factor is able to evaluate conversion rate (Fig. 6.7), with an assumption of 1st reaction order for narrow conversion interval. Despite excellent fit to experimental data, deviations of model-free kinetic parametres resulted in slight peaks at the beginning and end of conversion, where the highest errors were denoted resulting in decrease of the linear fitting quality (Table 10).

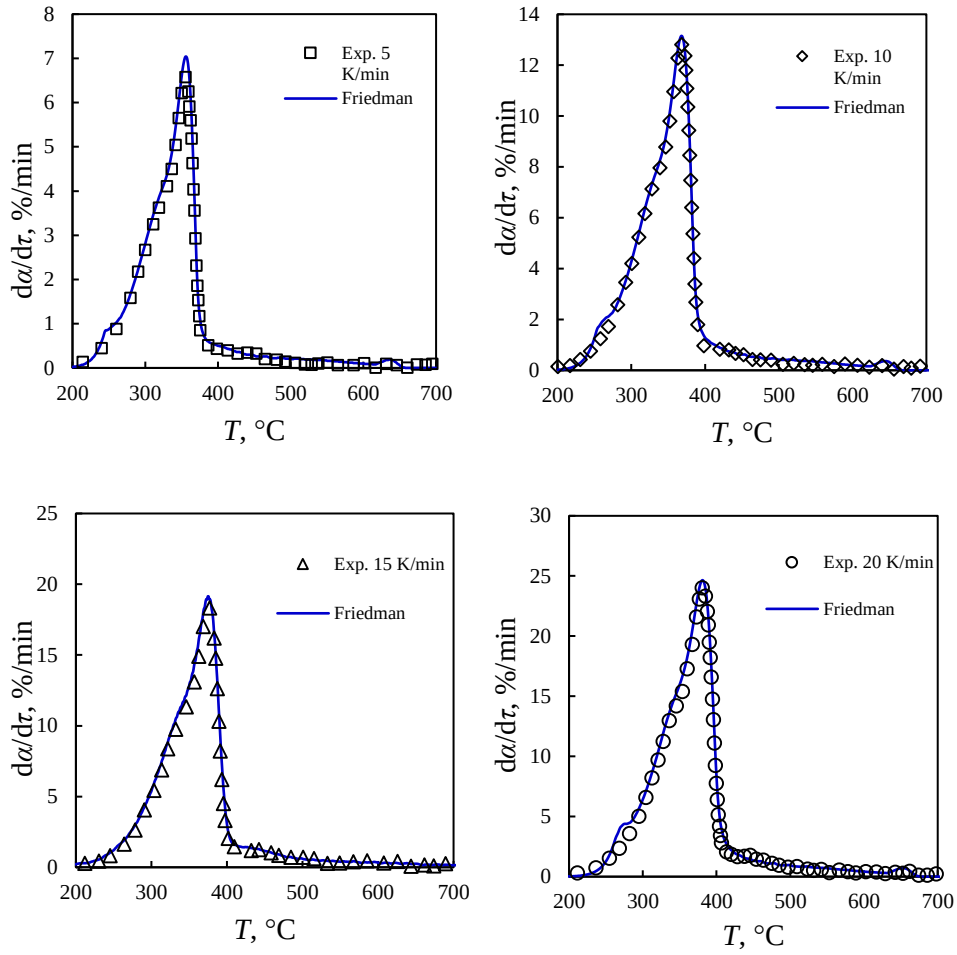

Fig 6.7. Conversion rate modeled using apparent kinetic parameters at heating rates of 5, 10, 15 and 20 K/min using Friedman method.

6.2.2. Generalized master-plot results

Following the description of generalized master-plot described earlier, Fig. 6.8 has been presented. Values of $f(\alpha)/f(\alpha)_{0.5}$ were calculated using the average Friedman model-free activation energy with experimental $d\alpha/d\tau$ and temperature profiles denoted during TGA runs at 5 and 25 K/min. In theory, the choice of reaction is made based on the best fit

of experimental $\lambda(\alpha)$ to theoretical models. Results shows, that investigated solar pyrolysis of waste wood may obey in general diffusion, phase boundary, and order based models, changing during the process, what prooves results of other woody biomass kinetic studies. M. Hu et al. (2016) [78] studied pyrolysis of pinewood, rice husk and bamboo (*Bambusa chungii*) via the TGA technique under low heating rates. The result of the model-free procedure showed that the lignocellulosic pyrolysis according to the one-step reaction model is dominated by the diffusion (D3, D4) effects. However, the complex features of variations caused by the mechanism changes caused that precise f(a) was hard to determine. Rueda-Ordóñez and Tannous [161] during the investigation the kinetics of the sugarcane straw pyrolysis also identified the reaction model. The pyrolysis experiments were conducted at four heating rates (1.25, 2.5, 5 and 10 °C/min) and the reaction model determined through master plots, corresponding to a two-dimensional diffusion (D2).

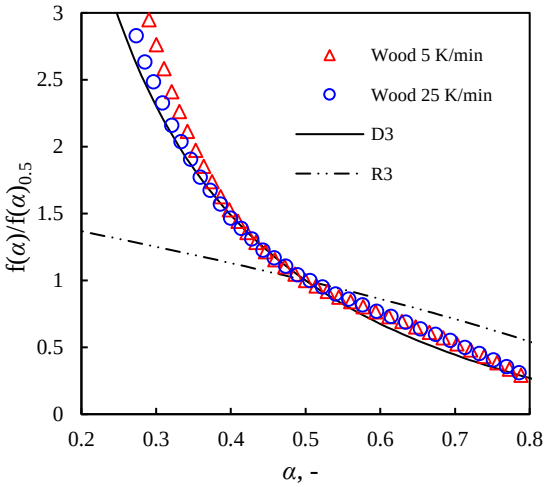

Fig. 6.8. Generalized master-plots method for pyrolysis of waste wood at 5,10,15 and 20 K/min.

It is believed that waste wood pyrolysis, according to Fig. 6.8, was governed by the D3 diffusion model, with a transition towards the R3 model at the end of conversion. Change of mechanism during the conversion can be explained by more than one reaction occurrence, where the effect of one reaction *e.g.*, D3, approaching to its end, is substituted with other reaction *e.g.*, R3 model. For pure polymers and crystals decomposition, the generalized master-plots should provide one, accurate and incontestable fit [104], what rarely happens during biomass pyrolysis.

6.2.3. Experimental master-plot based kinetic model construction

For the kinetic description of pyrolysis gas compounds formation, the proper approach to the kinetic model construction was necessary. The proposed experimental master-plot (E-MP) kinetic model based on pyrolysis gas formation profiles assumes that each of the gaseous compounds denoted at the gas analyzer (Fig. 6.9) is described by a specific reaction step (Eq. 5.4). Reaction models functions for the each step were assumed accordingly to conclusion from the master-plot presented in Fig. 6.8. As four gaseous compounds were measured during the experiment no less than 4 steps are expected in the kinetic model.

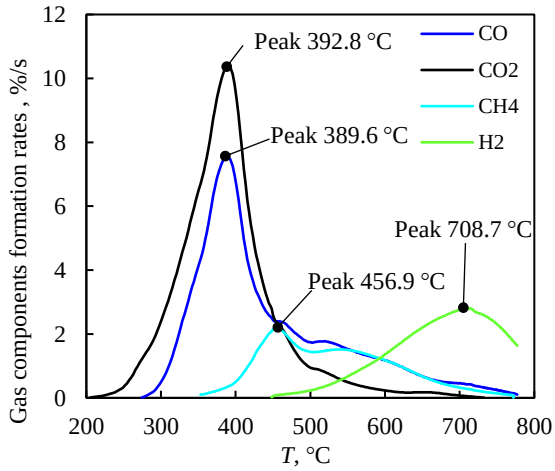

Fig. 6.9. Pyrolysis gas composition presented as a function of temperature for solar pyrolysis experiment at an average heating rate of 8.3 K/min.

The kinetic model was built gradually, first two main reactions were assumed to be CO and CO_2 formations, according to gas analyzer indications. Reaction models were chosen as D3 for CO_2 and R3 for CO. Observations of experiment allow to assume, that CO_2 release was associated with the most intensive tars formation, indicated by heavy vapors release, and intensive condensation in the spirals. Next, steps for CH_4 and H_2 formation were implemented using order based models and initial parameters were taken from isoconversional analysis at the end of the conversion, $\alpha \approx 0.8$ (Fig. 6.6). Where all the initial parameters and mechanisms were implementaed in the Kineitics Neo software, the model was optimized using least squares methods to maximize the fit quality of the calculated results to the predicted conversion rate profile of the WW at the same heating rate that was denoted during the experiments 8.3 K/min.

Table 13: Kinetic parameters of the wood pyrolysis E-MP model.

Step		Kinetic parameter value
Step: A → B		
Reaction model: D3 Equation: $\frac{d(a \to b)}{dt} = A \cdot 1.5 \frac{a^{2/3}}{1 - a^{1/3}} \cdot exp\left(\frac{-E}{RT}\right)$		
	E	159.921 kJ/mol
	Log(*A*)	10.439 Log(1/s)
	Contribution(*a*→*b*)	0.62
Step: B → C		
Reaction model: F2 Equation: $\frac{d(b \to c)}{dt} = A \cdot b^2 \cdot exp\left(\frac{-E}{RT}\right)$		
	E	256.778 kJ/mol
	Log(*A*)	19.052 Log(1/s)
	Contribution(*b*→*c*)	0.182
Step: D → E		
Reaction model: Fn Equation: $\frac{d(d \to e)}{dt} = A \cdot d^{3.463} \cdot exp\left(\frac{-E}{RT}\right)$		
	E	249.717 kJ/mol
	Log(*A*)	15.868 Log(1/s)
	n	3.463
	Contribution(*d*→*e*)	0.076
Step: E → F		
Reaction model: F1 Equation: $\frac{d(e \to f)}{dt} = A \cdot e \cdot exp\left(\frac{-E}{RT}\right)$		
	E	162.012 kJ/mol
	Log(*A*)	6.610 Log(1/s)
	Contribution(*e*→*f*)	0.018
Step: G → H		
Reaction model: R3 Equation: $\frac{d(g \to h)}{dt} = A \cdot 3\left(g^{2/3}\right) \cdot exp\left(\frac{-E}{RT}\right)$		
	E	180.997 kJ/mol
	Log(*A*)	12.165 Log(1/s)
	Contribution(*g*→*h*)	0.103

Final kinetic parameters of the E-MP model were presented in Table 13. First step A→B governed by the D3 model was expanded by second consecutive step, (F2) resulting in A→B→C step associated with CO_2 formation reaction. A consecutive mechanism in this step was chosen arbitrary, inversely, to cover the widespan of CO_2 indication. The first step having the highest contributing factor was the most dominant step in terms of kinetic apparency in the overall mass balance (Eq. 5.9) Activation energy and pre-exponential factor of step A→B being the 159.921 kJ/mol and 10.439 log(1/s) are within the range of main conversion range of isoconversional analysis presented in Fig. 6.6. CO formation was identified as R3, single-step G→H model with 180.997 kJ/mol activation energy nad 12.165 log(1/s) pre-exponential factor. The last step of conversion, charring, was described as two-step consecutive reaction, D→E→F Choice of consecutive reaction mechanism was based on gas analyzer indications after acknowleding the consecutive mechanism products formations in extensive work published by E. Moukhina on thermal decompostion kinetic mechanisms [108]. CH_4 indication started at approx. 350 °C with a peak at 456.9 °C, the same spot where H_2 indication started. This phenomenon can be roughly assigned to consecutive reaction ideas, where second product formation starts at the highest concentration of first product (by-product) with its peak at by-product minimum [108]. CH_4 was assigned to step D→E obeying nth-order model with high activation energy 249.717 kJ/mol addressing end of isconversional conversion (Fig. 6.6), pre-exponential factor 15.86 log(1/s) and reaction order equal 3.46. Reaction orders higher than 3 means that reaction is complex, which rate is probably dependable on more than 3 concentrations. Last step E→F was assigned to H_2 formation reaction obeying F1 model, with activation energy 162.012 kJ/mol and pre-exponential factor 6.610 log(1/s). Low contribution factors for last reactions D→E→F shows that despite the highest activation energies, their impact on total conversion is very low, yet quantifiable.

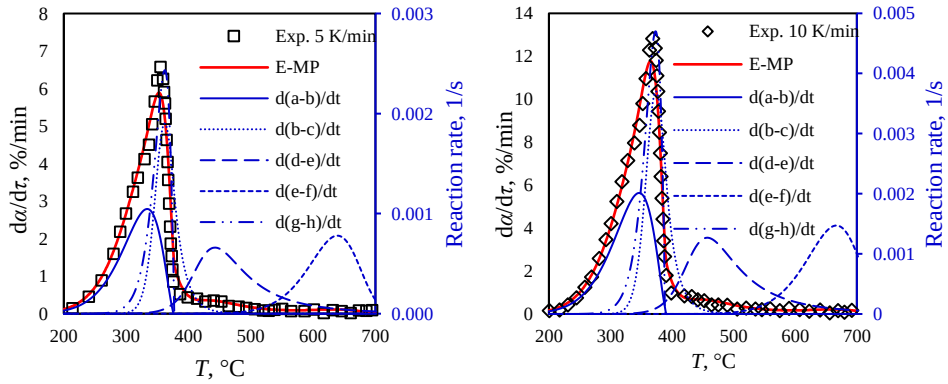

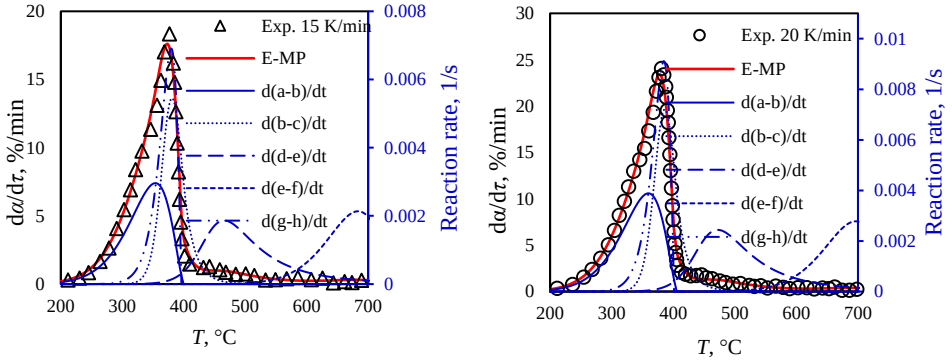

Fig. 6.10. Results of the E-MP model compared with the DTG profile at 5, 10, 15 and 20 K/min heating rates, R^2=0.99995.

Fig. 6.10 presents model results compared with the DTG profile obtained for 5, 10, 15 and 20 K/min heating rates. Regarding model fit to experimental data, the E-MP model focused on product formations, did not evaluated DTG shoulder well. In literature, the shoulder is associated with hemicellulose decomposition, which is responsible mostly for tars formations, which cannot be evaluated properly in this approach using the only dry gas analyzer. However, reaction formations of CO, CH_4, and H_2, related to the gas analyzer indications, where resembled calculated reaction rates and presented as well.

6.2.4. E-MP model predictions of solar pyrolysis experimental conditions.

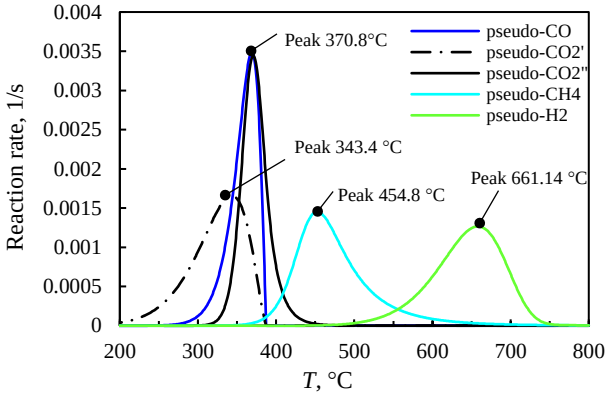

Fig. 6.11. Kinetic predictions of solar pyrolysis experimental conditions: modeled reaction rates compared to dry-gas components formation reactions, predicted for 8.3 K/min.

Kinetic predictions are used to evaluate process behavior at different thermal conditions than used for model calculation.Predicted reaction rates at a heating rate of 8.3 K/min (Fig. 6.11) were compared to gas analyzer indications during the solar pyrolysis experiment presented in Fig. 6.9, where the same average heating rate was denoted. In solar pyrolysis experiments, gaseous components peaks were denoted at temperatures 392.8°C for CO_2, 389.6 °C for CO, 456.9 °C for CH_4 and 708.7 °C for H_2. During experiments, influence on gas formation trends had reactor operation, mainly pressure drop change within the bed, the gas path through the reactor, condenser, and analyzer, and fluctuations of intert gas due to pressure change caused by tars slagging. Modeled peaks temperatures were 370.8 °C for CO and CO_2, 454.8 °C for CH_4 and 661.14 °C for H_2. CO_2 formation during experiments started at 200 °C and lasted throughout most of the experiment, ending indications at 720 °C. Two-step CO_2 model evaluated experimental peak with 22K offset, under the assumption that peak temperatures fit is comparable quantity, as reaction deacceleration shouldn't be compared with decreasing gas indications, biased with gas path interferences and phenomena. The peak for CH_4 formation was well modeled with only 2.1K offset. Due to the fact, that TGA measurement was carried out until 700°C and peak of experimental H_2 was denoted at 708.7°C, the predictions had to overscale hydrogen formation rate what resulted in a high offset of 47.6K.

6.2.5. Three pseudo-component model.

For comparative purposes, the classical three pseudo-component models (3-PC) was established. The model assumed three independent, single-step reactions obeying n^{th} order. Initial parameters for model optimization were adapted from isoconversional analysis results (Fig. 6.6). Table 14 presents the kinetic parameters of a final 3-PC kinetic model for waste wood solar pyrolysis. The presented approach analyses only biomass components decomposition, while the E-MP model analyzed product formations.

Table 14: Kinetic parameters and governing equations of the wood pyrolysis 3-PC model.

Step		Kinetic parameters value	
Step: A → B			
Reaction model: Fn			
Equation: $\frac{d(a \rightarrow b)}{dt} = A \cdot a^n \cdot exp\left(-E/RT\right)$	*E*	180.130 kJ/mol	
	Log(*A*)	13.666 Log(1/s)	
	n	2.399	
	Contribution		0.262
Step: C → D			
Reaction model: Fn			
Equation: $\frac{d(c \rightarrow d)}{dt} = A \cdot c^n \cdot exp\left(-E/RT\right)$	*E*	191.785 kJ/mol	
	Log(*A*)	13.568 Log(1/s)	
	n	0.648	
	Contribution		0.372
Step: E → F			
Reaction model: Fn			
Equation: $\frac{d(e \rightarrow f)}{dt} = A \cdot e^n \cdot exp\left(-E/RT\right)$	*E*	96.488 kJ/mol	
	Log(*A*)	6.469 Log(1/s)	
	n	5.312	
	Contribution		0.366

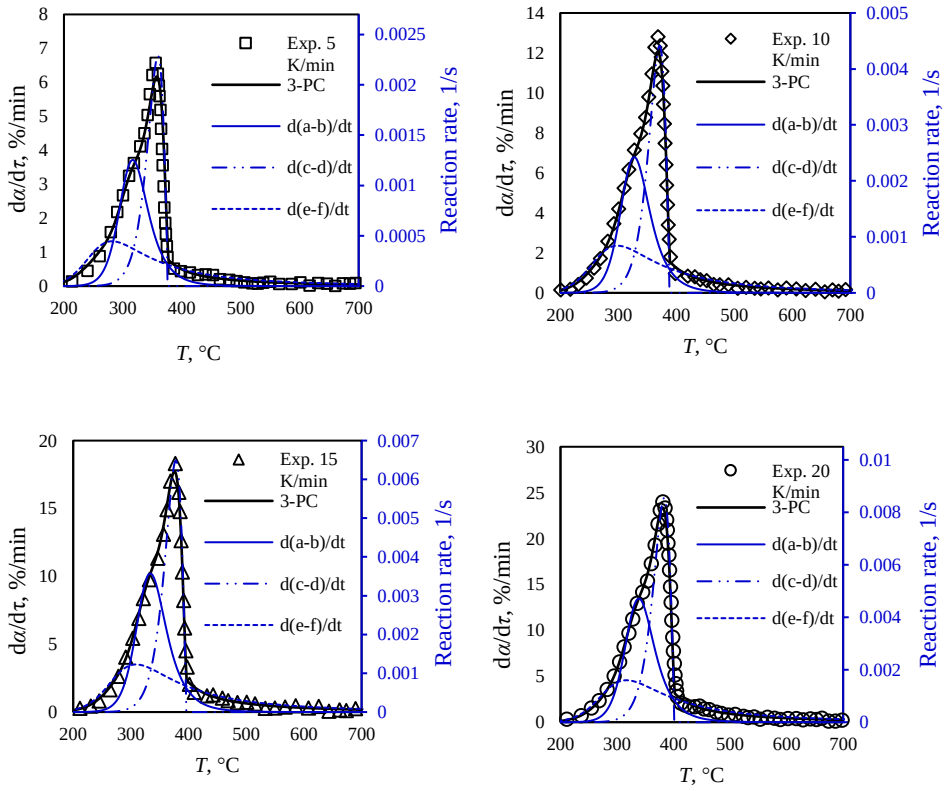

Fig. 6.12. Results of 3-PC model compared with DTG profile at 5, 10, 15 and 20 K/min heating rates, R^2=0.99994.

In Fig. 6.12, the results of the 3-PC model calculation were presented. Model calculations were compared with the same corresponding DTG profiles. The 3-PC model presented very high R^2=0.99994 and evaluated well kinetic peak and shoulder. Modeled reaction rates were compared to literature data in order to prove, that kinetic steps reflect biomass components decomposition.

Regarding biomass components cellulose, hemicellulose, and lignin, to expand information from the Introduction section, hemicellulose is constituted by sugar monomers. In contrast to cellulose, hemicellulose is composed of short-chain heteropolysaccharides and presents an amorphous and branched structure, such as xylan and its derivatives [34]. These monomers are forming shorter chains, which lowers the thermal stability of organics, while the decomposition range mainly covers 220–315°C. Lignin, the most difficult to decompose, thanks to aromatic rings constituents e.g., benzene rings connected with ether

bonds, more stable than β1,4-glycosidic bonds. Thus the rate of lignin decomposition is significantly slower than hemicelluloses and cellulose, and covers a wider temperatures regime from 160 to 900 °C. On the other hand, cellulose, a poly-crystal which is linearly formed by $(C_6H_{10}O_5)_n$ [78], with stronger thermal stability and decomposes quickly, showing steep and narrow peaks, once temperatures reaches of approx. 350°C.

According to above mentioned and literature data, first step A→B with E=180.13 kJ/mol and log$A$= 13.666 log(1/s) was associated with hemicelluloses decomposition, second step C→D, E=191.785 kJ/mol and log$A$=13.568 log(1/s) with cellulose and third step E→F with E=94.488 kJ/mol and log$A$=6.469 log(1.s) with lignin degradation. Kinetic steps for hemicellulose and lignin decomposition presented reaction orders higher than 2, 2.399 and 5.312 respectively, showing that in fact, the Fn model simplified the complex nature of the presented steps.

6.2.6. Discussion of E-MP and 3-PC models.

Despite very high R^2 in the case of both models, some significant differences can be spotted. The irony of the statistical evaluation of kinetic models was described by John E. White et al. [107] in a critical review of recent kinetic studies. Presented models follow two kinetics evaluation approaches: 3-PC model investigated wood pyrolysis kinetics addressing reactants decomposition, while the 3-MP model analyzed the product formations. Analyzing Figs 6.10 and 6.12, some minor and major flaws can be spotted. First, the 3-PC model evaluated well DTG profile shoulder and slightly undervalued cellulose peak, while the E-MP model didn't evaluate shoulder at all, from 200°C went almost straight to cellulose peak. This can be justified with laboratory station inability to record and quantify tar formation reactions, which are trapped in a condenser, what's more tars present in gas analyzer could cause serious damage to the device. At 400°C when a transition from the main devolatilization to charring occurs, the 3-PC model provided a smooth fit without deviations present in that range by the E-MP model. The fluctuation of calculated with E-MP DTG curve during devolatilization transition to charring was caused by the reaction mechanism, which was set just based on gas analyzer indications. It has to be mentioned that in reality, the charring process can be (or even is) much more complex and the kinetic model can be as accurate as identification methods of pyrolysis effects. Contribution averaged values of both model kinetic parameters present the same values, as they were established based on the same TGA profiles, resulting in the same apparent kinetic parameters and in fact described pyrolysis process, according to R^2, adequately good. Regarding the rest of the statistics, after the optimization process, the E-MP model resulted in the lowest values of MR and RSS, which states, that despite under-evaluated DTG profile peak and transition to charring, it still provided better fit to experimental data than the 3-PC model.

For both models, contribution factors were compared to experimental data, which in the case of the E-MP model were gas analyzer indications , and biomass component shares for the 3-PC model. Contributions of reactions steps assigned to product formations *i.e.*, 0.802 for CO_2, 0.103 for CO, 0.076 for CH_4 and 0.018 for H_2 were compared with gas components shares denoted in the solar pyrolysis experiment, being the 34.5% CO, 53.1% CO, 10% CH_4 and 2.4 % H_2. As contribution factors are dimensionless and sum to the 1, the can be compared with percent. Contribution factors for CO and CO_2 are mismatched, probably due to the inability of exact tars release indication, a however good match for CH_4 and H_2 was achieved. In the case of a 3-PC model, contributions of reaction steps being 0.262, 0.372 and 0.366 did not meet biomass component shares 11.8% 54.8% 27.9% for hemicellulose, cellulose, and lignin respectively.

Table 15: Statistical analysis results for Friedman method and E-MP and 3-PC models.

Model	*MR*	R^2	S^2	*F-test*	$F_{(p=0.05,v1=4,\ v2-\infty)}$
Friedman	0.232	0.9999	211.3	1.649	2.21
OFW	1.621	0.9970	12553.8	97.7	
KAS	1.726	0.9960	16760.2	130.8	
E-MP	0.0036	0.9999	124.8	1.00	
3-PC	0.2653	0.9999	258.	1.816	

Within this discussion, the choice of reaction models for both approaches was crucial. Reaction models significantly influence kinetic parameters, which poor choice can ruin whole kinetic analysis, laying the basis for false conclusions. In the E-MP approach, reaction models were established using a generalized-master plot, and in the kinetic mechanism was assigned arbitrarily to obtain the best fit. For the 3-PC approach, the reactions were assigned to n^{th} order reaction models, which are subject to debates in terms of their physical meaning. Regarding n^{th} order models, reaction order is a sum of exponentials of reactants concentrations in classical reaction constant formula. If reaction order is higher than 2, *e.g.*, 5, and reaction orders are expressed in rational, non-integer numbers (as reported in the literature) instead of classical natural numbers, than from a mathematical point of view there is an infinite combination of a number of concentrations and exponentials that sum will give 5. From a physical point of view, reaction order n=5 means that, according to cumulative 1^{st} order elementary reactions collision theory, one product molecule is a result of a collision of 5 reactants molecules that occurs at the same moment of time and space, under the assumption that molecules are currently having total energies higher than activation energy. In practice, the rate (probability of successful collision) of such reaction is very low, and gradually approaches 0 with the increase of reaction order. Thus, in terms of order based kinetics, non-order based models seems to be

safer from unwanted compensation effects of kinetic parameters values by fit-chasing adjustments of reaction orders, *if only* those models are identified well.

Statistical analysis results listed in Table 15 show, that among tested models and methods, the one model that provided the best R^2 with the lowest standard deviation, proved by lowest *F-test* was arguably the E-MP model. Critical F distribution was adapted for the level of significance 95% and corresponding for the right tail area p=0.05. Numerator degree of freedom, v_1, related to the number of models tested was equal to 4 while the degree of freedom of denominator, v_2, related to the number of observations (experimental points) was much higher than 100, thus infinity extreme value was adopted. For such a specified critical point of *F-distribution*, $F_{(p=0.05,v1=4,\ v2=\infty)}$, was equal to 2.21. Models fulfilling $F > F_{(p=0.05,v1=4,\ v2=\infty)}$ give reason to reject them from analysis. It has to be stated, that *F-distribution* does only evaluate models considered within the test population. Regarding S^2 the E-MP model was the most accurate model to describe waste wood pyrolysis, however, according to the null hypothesis, Friedman method and 3-PC model gave significantly equal results, therefore it shows that statistical elimination of kinetic methods is somehow ambiguous.

6.2.7. Validation of the kinetic models.

According to the ICTAC Kinetic Committee, each kinetic model should be properly validated. The best validation possible is to good fit between isothermal experiments and predictions based on the non-isothermal established model. In this study, non-isothermal predictions were compared with the DTG profile obtained for the same waste wood sample at 30 K/min (Fig. 38).

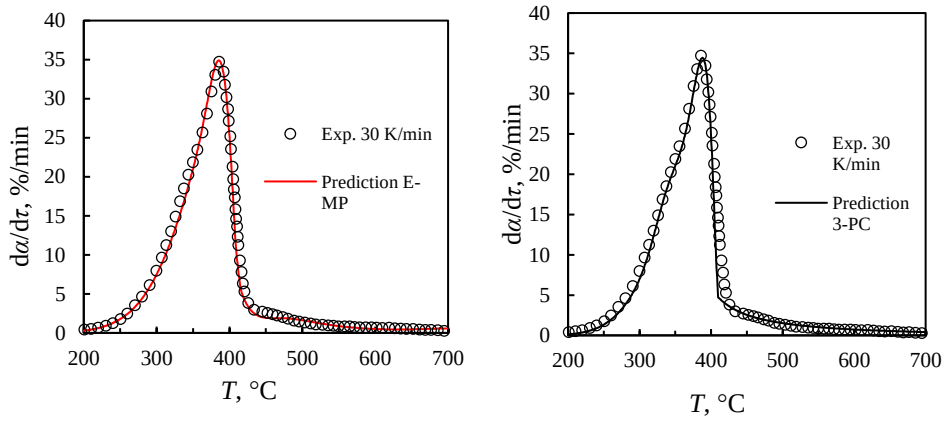

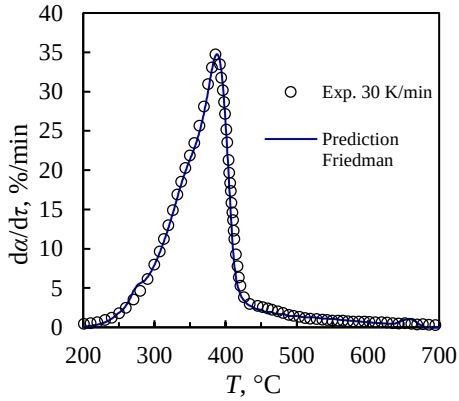

Fig. 6.13. Comparison of conversion rate profiles between kinetic predictions of models: E-MP, E-PC with Friedman method and DTG profiles at 30 K/min.

Fig. 6.13 presents three kinetic predictions calculated based on the E-MP model, 3-PC model, and model-free Friedman method. The best evaluation of experimental peak and shoulder was provided by the 3-PC model and Friedman method due to: (1) holistic approach to decomposition, without consideration of the products and (2) model assessment was based on the best fit to experimental data. E-MP model overshot profile shoulder, aiming straight for the maximum of decomposition, as only gaseous compounds were taken into consideration, without any information about heavy volatiles release. If only bio-oil vapors release could be parametrized, the E-MP model could be enhanced by additional steps, which can be a subject of future studies. As profiles in Fig. 6.13 seem to validate each model adequately, a simple statistical comparison of three kinetic predictions was established based on R^2 determination.

Table 16: Summary of fit quality parameters of kinetic predictions to experimental DTG profile at 30 K/min.

Model/method	S^2	R^2
Friedman	411.27	0.9947
E-MP	645.93	0.9918
3-PC	1506.25	0.9800

Table 16 lists basic parameters for R^2 calculation. Among validated models and methods. The best fit for experimental DTG profile at 30 K/min was provided by Friedman method prediction. Surprisingly, the second-best model was denoted for E-MP predictions, which model despite the assumption of gaseous compounds consideration provided a better fit than predictions of 3-PC.

6.3. Model-based kinetics of the sewage sludge pyrolysis

In this Chapter the kinetic modelling of the SS pyrolysis is presented, with emphasis on the development of the methodology for the kinetic parameters determination according to the Research Task III of the doctoral dissertation, based on TGA measurements. Proposed methodology based on isoconversional kinetic results resulted in determination of the 10th independent reaction model describing SS pyrolysis. Just like in the previous Chapter on WW pyrolysis kinetics, the SS kinetic modelling begins with isoconversional analysis of the non-isothermal TGA data, and the most accurate method is specified based on *F-test* criteria.

Table 17: Statistical evaluation of the different isoconversional methods results for SS pyrolysis.

Method	R^2	S^2	Degree of freedom, v	F	Critical *F-distribution*
Friedman	0.99999	9.65	1065	1.00	
FWO	0.98691	19959.9	1065	2518	
KAS	0.98688	15577.1	1065	1856	2.60
10th independent reaction model	*0.99999*	*11.725*	*1210*	*1.07*	

For sewage sludge pyrolysis, within the presented study, the best fit to experiment presented Friedman method results, which from now on will be treated as the most probable data to describe sewage sludge pyrolysis. Isoconversional integral FWO and KAS methods, despite R^2 higher than 0.98, were rejected, as their F-test results, $F >> F(p=0.05, v_1=3, v_2=\infty)$, was unacceptable (Table 17). The proposed conclusion is to always support model evaluation with an additional statistic, not only with arguable and subjective "high" R2. The reason why integral methods usually present higher inaccuracies is probably the crude expression of temperature integral, proving the superiority of differential isoconversional methods *e.g.*, Friedman method in biomass pyrolysis kinetics evaluation.

6.3.1. Friedman method results

Table 18 presents supplementary values of Freidman analysis from which slope and intercept can be easily calculated. Each α has assigned three sets of $log(d\alpha/d\tau)$ and $1000/T$ values for three hating rates in order to plot an isoconversional straight line. The deviation of experimental points from isoconversional lines is evaluated with a coefficient of linear determination R^2.

Table 18: Friedman isoconversional regression slope and intercept values with linear fit quality for each heating rate examined.

	20 K/min		30 K/min		40 K/min		R^2
α	1000/*T*, 1/K	Log(dα/dτ), Log(1/s)	1000/*T*, 1/K	Log(dα/dτ), Log(1/s)	1000/*T*, 1/K	Log(dα/dτ), Log(1/s)	
0.01	3.092	-3.481	2.971	-3.164	2.886	-3.023	0.98
0.05	2.854	-3.269	2.771	-3.051	2.684	-2.962	0.93
0.1	2.599	-3.383	2.526	-3.193	2.439	-3.083	0.96
0.15	2.330	-3.409	2.265	-3.280	2.200	-3.135	0.99
0.2	2.086	-3.434	2.033	-3.207	1.989	-3.058	0.99
0.25	1.931	-3.219	1.898	-2.995	1.867	-2.849	0.99
0.3	1.850	-3.006	1.823	-2.816	1.797	-2.679	0.99
0.35	1.798	-2.895	1.774	-2.709	1.750	-2.568	0.99
0.4	1.758	-2.857	1.735	-2.665	1.713	-2.523	0.99
0.45	1.721	-2.850	1.699	-2.668	1.678	-2.541	0.99
0.5	1.686	-2.867	1.665	-2.681	1.644	-2.544	0.99
0.55	1.651	-2.846	1.631	-2.676	1.612	-2.541	0.99
0.6	1.618	-2.864	1.599	-2.682	1.581	-2.548	0.99
0.65	1.586	-2.908	1.567	-2.720	1.549	-2.588	0.99
0.7	1.550	-2.954	1.533	-2.768	1.516	-2.642	0.99
0.75	1.509	-3.076	1.493	-2.890	1.478	-2.742	0.98
0.8	1.457	-3.172	1.443	-3.004	1.429	-2.877	0.99
0.85	1.402	-3.253	1.388	-3.062	1.376	-2.946	0.99
0.9	1.342	-3.316	1.329	-3.156	1.318	-3.005	0.99
0.99	1.075	-3.945	1.061	-3.857	1.053	-3.680	0.99

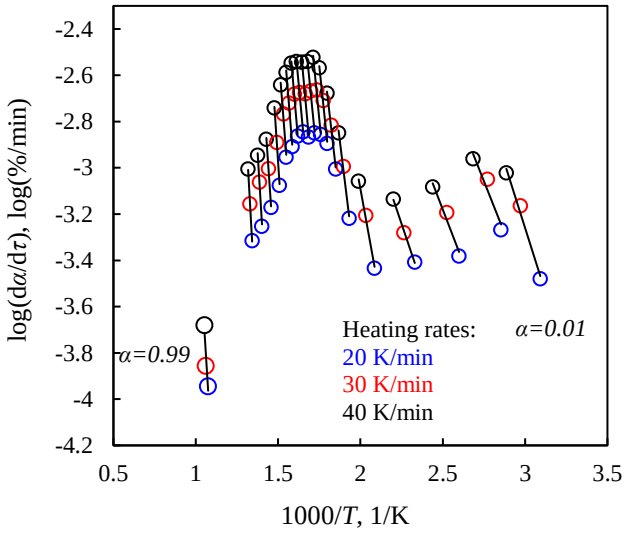

Fig. 6.14. Selected isoconversional lines obtained during Friedman analysis of TGA profiles.

Based on data presented in Table 18, Fig. 6.14 was created, illustrating methodology if isoconversional Friedman method. Conversion extent progress is inverted to reciprocal temperature increase, which has to be taken into account when reading these plots. First isoconversional lines, at the right-hand side of Fig. 6.14 are assigned to moisture evaporation, slowly turning into main pyrolysis region at 1.5-2 *1000/T*. From an isoconversional line inclination angle to the ordinate axis arguable reaction type can be decrypted. If the slope of experimental values is lower than the slope of Friedman isoconversional lines, the reaction presents deaccelerating character (Diffusion models, Contracting geometry, n^{th} order models), if the slope of experimental points is steeper than the constant conversion lines, such process is accelerating throughout the conversion *e.g.*, Avrami-Erofeev nucleation model. The case, when the inclination angle of measured points and isoconversional lines are similar or the same, reaction presents an indifferent character, usually described by 1^{st} reaction order. In order to get more intuitive insight into the above mentioned phenomenon, it should be stated that slope comparison provides information about or rate progress between constant conversion points in series of dynamic measurements, presented in differential form. In accelerating processes, distances between constant conversion points plotted at conversion rate profiles are increasing with the heating rate (accelerating), as the speed of conversion increases, while on the other hand for deaccelerating reactions, like pyrolysis, this distance is decreasing, like presented SS plots in Fig. 6.15. For indifferent processes, the distances between the constant conversion points

should be more or less the same. This information can be useful during reaction models choice for complex kinetic models.

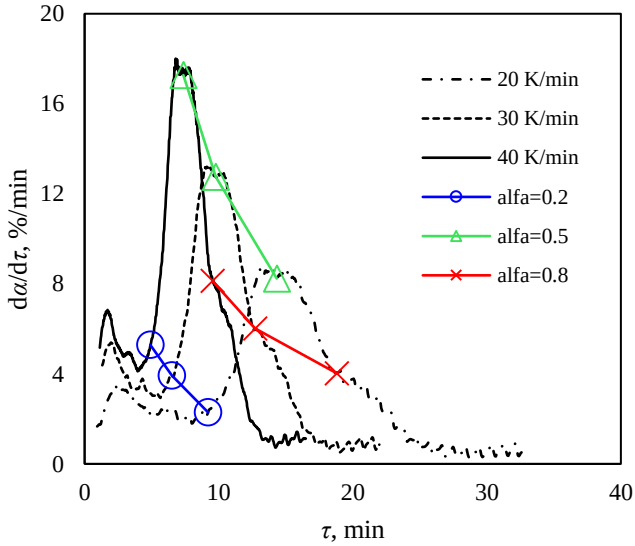

Fig. 6.15. SS pyrolysis iso conversion points compared at different heating rates.

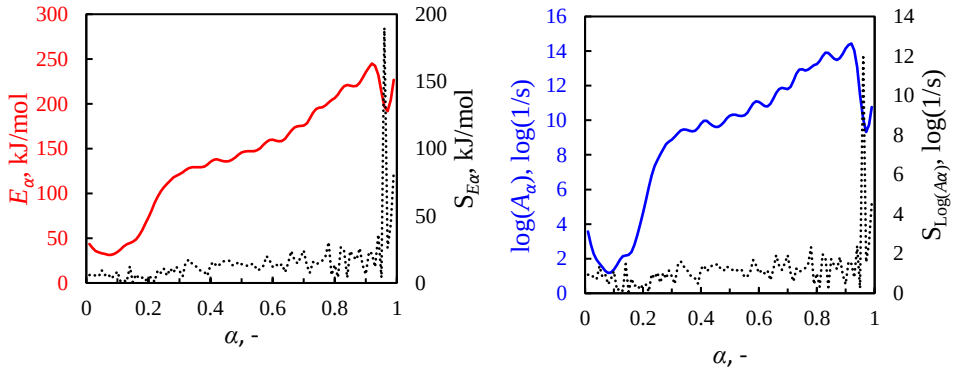

Fig. 6.16. Friedman isoconversional kinetic parameters: activation energy (red) and pre-exponential factor (blue) with standard regression errors.

Fig. 6.16 shows that both estimated kinetic parameters are strongly correlated with each other. Isoconversional kinetic parameters gradually increase during pyrolysis, from 42.1 to 250 kJ/mol and from 3.21 to 14.8 log(1/s) for activation energy and pre-exponential

factor respectively, making it really hard to distinguish plateau regions, corresponding single reaction step. However, the assumption of this methodology is to assign elementary reaction occurrence for every plateau (or rather "step") of isoconversional parameter profile, adapting E_α and A_α value specific for a plateau, and finishing kinetic triples with reaction model denoted in generalized master-plot.

Table 19: Isoconversional kinetic parameters calculated using Friedman method at selected reaction extent points.

α	E_α, kJ/mol	$S_{E\alpha}$, kJ/mol	log(A_α), log(1/s)	$S_{\log(A\alpha),}$ log(1/s)	$A_{\alpha,}$ 1/min
0.01	43.51	5.96	3.57	0.93	$2.22 \cdot 10^{5}$
0.05	33.04	9.43	1.71	1.37	$3.09 \cdot 10^{3}$
0.1	34.47	8.49	1.36	1.12	$1.38 \cdot 10^{3}$
0.15	45.81	0.61	2.22	0.07	$9.90 \cdot 10^{3}$
0.2	73.20	4.30	4.65	0.46	$2.67 \cdot 10^{6}$
0.25	106.73	10.56	7.70	1.05	$3.00 \cdot 10^{9}$
0.3	121.27	9.05	8.88	0.86	$4.53 \cdot 10^{10}$
0.35	129.34	13.31	9.46	1.23	$1.72 \cdot 10^{11}$
0.4	135.29	13.62	9.81	1.24	$3.85 \cdot 10^{11}$
0.45	135.53	16.13	9.61	1.43	$2.47 \cdot 10^{11}$
0.5	145.50	14.05	10.27	1.22	$1.12 \cdot 10^{12}$
0.55	147.97	9.39	10.28	0.80	$1.14 \cdot 10^{12}$
0.6	159.85	12.12	11.06	1.01	$6.95 \cdot 10^{12}$
0.65	165.22	14.57	11.25	1.19	$1.07 \cdot 10^{13}$
0.7	175.67	24.11	11.80	1.93	$3.77 \cdot 10^{13}$
0.75	195.49	15.12	12.95	1.18	$5.33 \cdot 10^{14}$
0.8	206.47	13.39	13.25	1.01	$1.07 \cdot 10^{15}$
0.85	220.19	23.81	13.73	1.73	$3.20 \cdot 10^{15}$
0.9	235.25	6.48	14.15	0.45	$8.44 \cdot 10^{15}$
0.99	226.65	82.47	10.77	4.58	$3.55 \cdot 10^{12}$

Table 20: Comparison of literature reports on SS properties with denoted isoconversional kinetic parameters.

Sewage sludge property	Shahbeig and Nosrati [158]	Naqvi et al. [141]	Sobek and Werle*
Origin	Urban WWTP, Teheran, Iran	Pilot-scale membrane bioreactor (MBR) in WWTP, NUST, Pakistan	Urban WWTP, Poland
Proximate analysis, wt. %			
Moisture	9.7[d]	6.5[d]	16.6[a]
VM[d]	52.7	44.6	50.54
A[d]	30.9	44.6	27.86
FC[d]	6.7	4.3	5
HHV[d], MJ/kg	16.47	11.50	15.62
LHV[d], MJ/kg	-	-	14.59
Elemental composition, wt.%			
C	47.4	40.4	37.8
H	6.9	6.2	5.3
O[diff.]	36.3	45.7	54.2
N	7.3	6.7	5.9
S	1.2	1.0	2.1
Isoconversional kinetics results, methods and TGA analysis setup			
Sample mass, mg	10	6	5
Inert gas type	N_2	N_2	N_2
Inert gas flow rate, ml/min	50	60	50
TGA heating rates, K/min	5, 10, 30, 50	5, 10, 20	20, 30, 40
Final temperature, °C	1000	800	700
α range	0.1-0.9	0.1-0.9	0.01-0.99
E_α, kJ/mol			
Friedman	-	10.6-306.2	33.0-226.7
FWO	59.3-247.4	45.6-231.7	21.8-289.3
KAS	52.4-235.5	41.4-232.1	21.4-289.0
Starink	52.4-235.9	-	-
Popescu	-	44.1-241.1	-

A_α, 1/min				
	Friedman	-	$1.03 \cdot 10^{-2}$ - $1.49 \cdot 10^{8}$	$2.22 \cdot 10^{5}$-$2.74 \cdot 10^{14}$
	FWO	$1.32 \cdot 10^{4}$ - $1.03 \cdot 10^{21}$	$1.04 \cdot 10^{9}$ - $4.39 \cdot 10^{19}$	8.04-9.14$\cdot 10^{17}$
	KAS	$2.94 \cdot 10^{3}$-$9.00 \cdot 10^{19}$	$4.95 \cdot 10^{4}$ - $4.38 \cdot 10^{8}$	13.12-1.02$\cdot 10^{18}$
	Starink	$2.93 \cdot 10^{3}$-$9.92 \cdot 10^{19}$	-	-
	Popescu	-	$2.92 \cdot 10^{8}$ - $2.96 \cdot 10^{22}$	-

When presenting isoconversional kinetic results for SS pyrolysis, a proper discussion with regards to the latest studies should be made. The results of this study were compared to the latest literature [141,158] regarding SS pyrolysis kinetics emphasizing the implementation of isoconversional methods, and presented in Table 20. The comparison included complete characterization of each SS investigated, with elemental composition and proximate analysis, calorific values as well as TGA experiment setup. All of the selected for presentation isoconversional results were determined by high-quality analysis, with R^2 very close to 1.

For comparison purposes, the elemental composition was calculated to dry-ash-free (daf) state based on reported moisture and ash content. Discussed SS samples from Iran and Poland were similar in terms of VM and A content, while SS from membrane bioreactor contained less VM in favour of ash residue. The same tendency was followed by HHV, 16.47 and 15.62 MJ/kg for Iran and Poland respectively, with 11.62 MJ/kg for SS from Pakistan. Further discussion of SS properties with respect to extraction technology, should be enhanced with detailed technology characterization and economic aspects, which are out of the scope of this study.

Isoconversional methods results for three SS samples obtained in wastewater treatment plants (WWTP) in Iran, Pakistan, and Poland seem to be in good agreement with each other. Isoconversional activation energies for presented methods *i.e.*, Friedman, FWO, KAS, Starnik and Popescu (however, the two latter described elsewhere), generally do not exceed 300 kJ/mol what can be the reasonable boundary for pyrolysis reaction [112]. The highest disproportions are observed for isoconversional pre-exponential factors, yet it has to be kept in mind that A_α values strongly depend on its estimation method i.e. $f(\alpha)$ assumption and compensation effect [110], and furthermore, are specific for each sample decomposition. Shahbeig and Nosrati stated in their work [158] that pre-exponential factor values strictly elucidate the reaction chemistry, which is crucial during the pyrolysis process optimization. It was highlighted that $A<10^9$ 1/min, on the one hand, mainly shows the surface reaction, while $A>10^9$ 1/min indicates a complex reaction, not dependent on the surface area. Addressing the above thesis to this study, pre-exponential factors listed in Table 19 would indicate that transition point from surface to complex reaction is α=0.25, which possibly corresponds with the termination of the moisture evaporation.

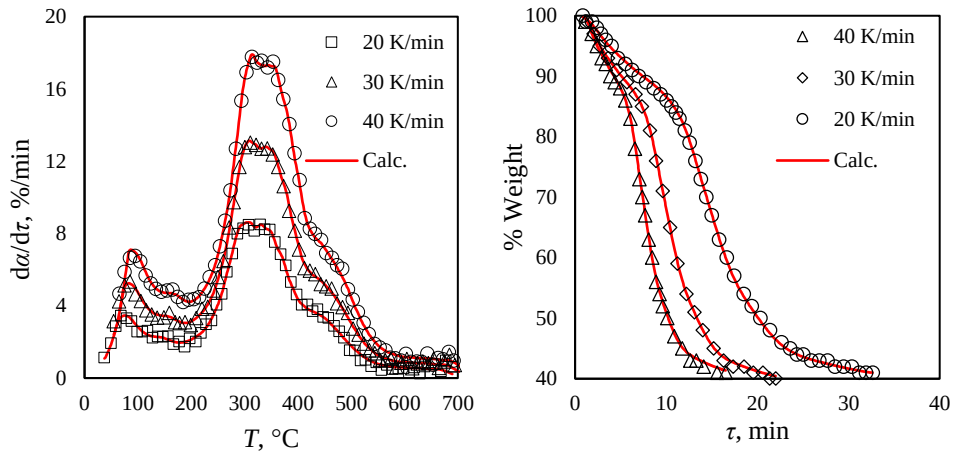

Fig. 6.17. Friedman calculation results compared with experimental data: conversion rate and mass loss profiles.

Regarding Fig. 6.17, presenting fit of modelled by Friedman conversion rate to experimental data, it can be stated that SS pyrolysis consists of a number of independent reactions, with highly overlapping peaks. Starting from 25 °C moisture evaporation occurs with a peak at 90.7 °C followed by first decomposition with a peak at 150-160 °C. Next, at the main primary pyrolysis region two overlapping reactions occur with temperature peaks 315 and 360 °C respectively. After the highest peaks slower reaction comes out in the form of curve "shoulder" between 400 and 600 °C. This reaction can be assigned to a complex carbonization process, releasing volatiles first with parallel charring lasting until the end of decomposition.

Despite a lack of reaction model assumption, Friedman method well-evaluated mass loss and conversion rate profiles. Differential approach for isoconversional kinetics matched experimental results in the most challenging regime, the flat and wide peak at highest conversion rates, where standard single-step kinetic model based on Eq. (5.4) would fail. Inability to model high and wide conversion peaks is inevitably connected to mathematical limitations of the single-step kinetic models. For constant E and A, conversion rate profile character is mapped by $f(\alpha)$ function, which at least for known models, after introduction to equation (4.4) inevitably approaches usually sharp maximum (function extreme). With that in mind, in model-fitting kinetics, wide conversion peaks can be modeled as an integral sum of elementary reaction (kinetic) steps.

6.3.2. Generalized master-plot, reaction model identification

Results of generalized rate fittings are shown in Fig. 6.18. Investigated sewage sludge decomposition once again presented deaccelerating behavior during pyrolysis. Such behavior of the processes was denoted on the basis of on very good fit to high (n>5) order based model, perceived as a typical example of deaccelerating kinetics [104]. The high reaction order reaction model is arguable from the physical point of view [112]. On the other hand, Stolarek and Ledakowicz [135] believe that high reaction orders are typical for lumped systems containing a number of first-order reactions with gradually increasing activation energies, what in case of such complex material as sewage sludge seems reasonable.

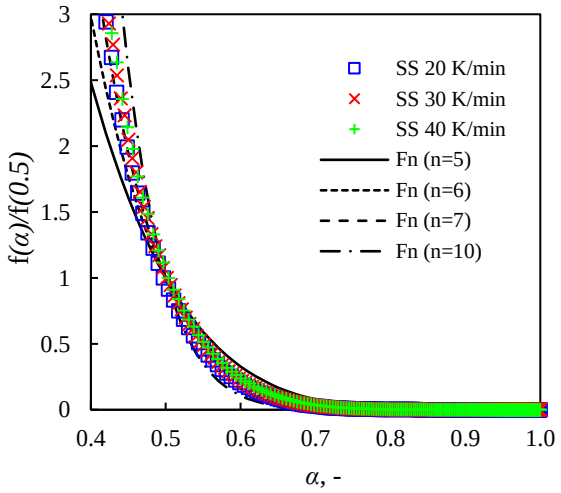

Fig. 6.18. Generalized master-plot results plotted against order based reaction models.

6.3.3. Methodology for the kinetic parameters determination, 10 independent reaction model

Once a range of heating rates, corresponding to the investigated process, is established, the proposed methodology can be applied. First, isoconversional, model-free analysis is performed in order to determine isoconversional activation energy and pre-exponential factor profiles. From isoconversional kinetic curves (Fig. 43) number of information about reaction model, a number of reaction steps, and reaction mechanism can

be decrypted [108]. In the case of complex, waste-derived substances *e.g.*, sewage sludge, each feedstock potential component *i.e.*, hydrocarbons, minerals, fatty acids, proteins, decomposes with an independent manner so independent reactions mechanism is justified and popular across the literature [157]. The presented methodology assumes that each plateau in Fig. 6.16 corresponds a single reaction step. In order to construct kinetic, model initial parameters were decrypted from plateau areas forming a set of 10 elementary reactions with own kinetic triplets. Initial guess values of E, A and assumed n^{th} reaction order models, and equally distributed contribution factors, c. After establishing initial parameters (Table 21) optimal parameters were calculated using the Netzsch least square optimization method, set to provide the best fit with the experimental data. Results of 10 independent reactions kinetic model are presented in Table 22.

Table 21: Initial guess parameters for 10 independent reactions kinetic model.

Step	*f(α)*	*E*, kJ/mol	log(*A*), log(1/s)	*n*	*c*
A → B	Fn	42.1	3.24	1	0.1
C → D		42.1	1.64	1	0.1
E → F		131	9.48	1	0.1
G → H		137	9.58	1	0.1
I → J		148	10.4	1	0.1
K → L		160	11.1	1	0.1
M → N		175	11.9	1	0.1
O → P		198	13.1	1	0.1
Q → R		223	13.9	1	0.1
S → T		250	14.8	1	0.1

Table 22: Kinetic model parameters of SS pyrolysis consisting of 10 independent elementary reactions.

Step	*f(α)*	*E*, kJ/mol	log(*A*), log(1/s)	*n*	*c*
A → B	Fn	30.34	2.28	2.34	0.102
C → D		61.46	3.97	1.93	0.225
E → F		153.46	11.31	2.34	0.102
G → H		259.67	22.49	3.00	0.092
I → J		159.99	11.99	2.53	0.119
K → L		182.23	12.98	1.48	0.062
M → N		146.52	8.94	1.89	0.058
O → P		195.03	12.61	2.06	0.05
Q → R		158.30	9.01	1.25	0.042
S → T		68.77	1.17	1.17	0.066

Kinetic parameters listed in Table 22 present kinetic triplets for 10 elementary reactions used to describe sewage sludge pyrolysis. Activation energies of elementary steps vary from 30.34 to 259.67 kJ/mol, logarithms of pre-exponential factors contain within 1.17 and 22.49 log(1/s) what shows good agreement with other studies SS pyrolysis kinetic studies [141,157]. Contribution factors, *c*, describes the total share of the elementary step in the final integral kinetic formula based on equation (4.10). Reaction orders vary from 1.17 to 3.00, which partially proves the thesis posted by the work of Stolarek and Ledakowicz [135] that high reaction orders in single-step kinetics are in fact a product of lumped approach to a system of a set of elementary reactions. In this case, 10 independent reactions, with gradually increasing activation energies (Fig. 6.19).

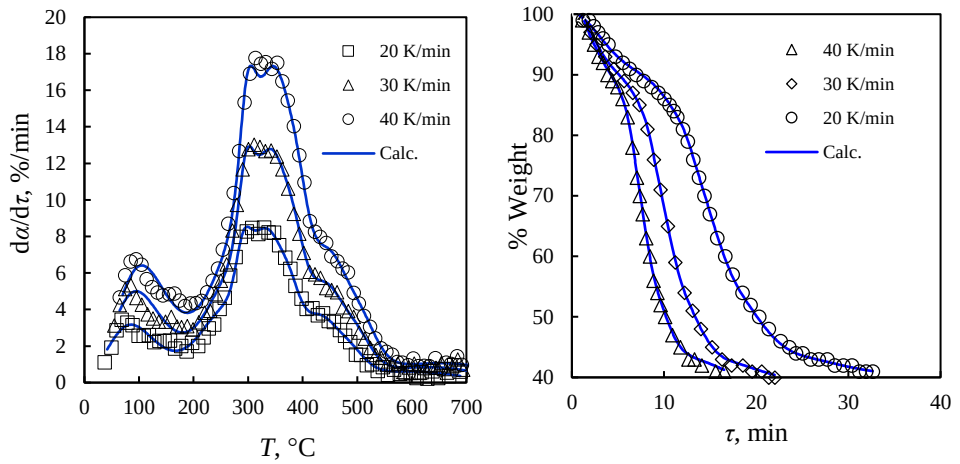

Fig. 6.19. 10 independent reaction kinetic model results plotted against TGA and DTG experimental profiles.

Fig. 6.19 presents the results of the kinetic model fit to experimental data. Besides moisture evaporation region established model presents a satisfying fit for experimental data with R^2 higher than 0.9999. If one would like to establish mass loss and conversion profiles only, isoconversional analysis would be just enough. However, if one would like to acknowledge elementary reaction rates, the creation of the well-identified kinetic model is crucial.

+6.3.4. Modelled reaction rates

The product of the kinetic model is a mathematical expression of process (reaction) rate. When isoconversional methods can evaluate conversion rates only, kinetic models based on reaction mechanism and specific reaction models can evaluate actual reaction rates. Well-evaluated kinetic triplets arranged into kinetic models allow forming a set of reaction rates, describing the decomposition process from not only mass loss perspective but product formation as well. Unfortunately, without proper analytical methods for products identification reactions, blue profiles presented in Fig. 6.20 are only theoretical rates of alleged sewage sludge components resulting in pyrolysis product formations. Despite that, a number of information can be retrieved. In order to provide good quality fit to experimental data, the presented methodology resulted in 10 independent step distinction, which resulted in 10 reaction rates. Thesis from the introduction stating that sewage sludge decomposition consists of overlapping peaks can be justified based on rates presented in Fig. 6.20. Modeled pyrolysis reaction rates align adequately to the mass loss rate curve shown as they "fill" the place underneath the red profile. First reaction rate A→B can be assigned to moisture evaporation step.

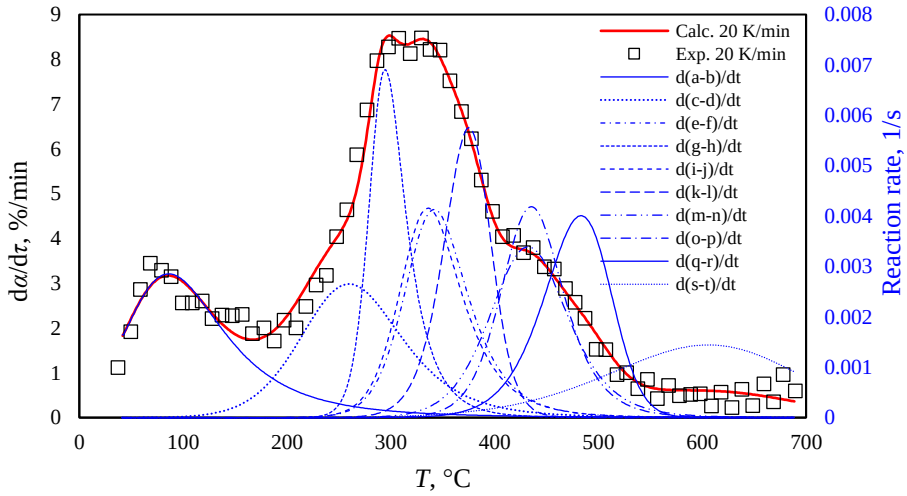

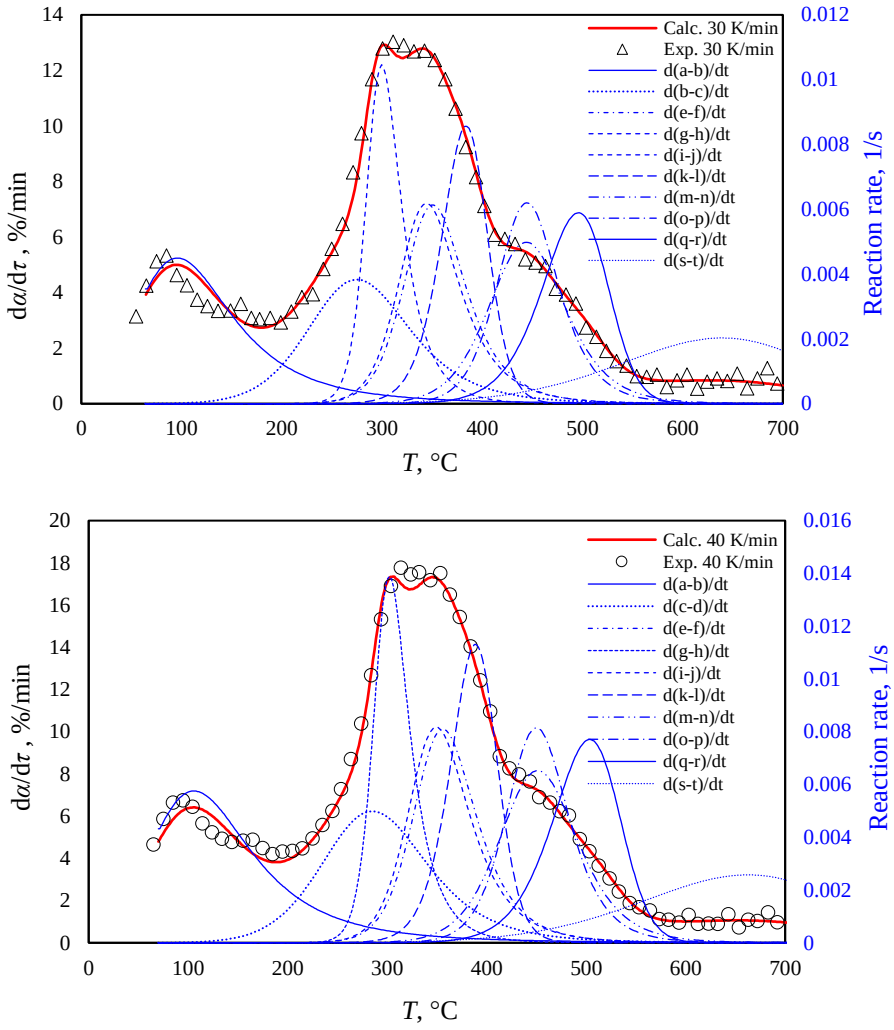

Fig. 6.20. Modelled reaction rates plotted against experimental conversion rate profiles.

6.3.5. Validation procedure

According to ICTAC Kinetic Committee recommendations [104] kinetic models ought to be validated on the basis of kinetic predictions of model behavior, at different heating rates than ones used for calculation, and compared to corresponding experimental

profiles. Within this Chapter, sewage sludge pyrolysis non-isothermal established model was compared with non-isothermal TGA profiles at slow heating rates of 1, 5 and 10 K/min.

In Fig. 6.21 model predictions were compared to experimental profiles. As can be seen, the established model, despite excellent fit at faster heating rates (Fig. 6.20), partially overestimated conversion rate profiles at heating rates used for validation procedure. This phenomenon can be explained by moving low activation energy steps towards lower temperatures at lower heating rates, which is clearly shown at temperature 200 °C. It is plausible, that one of the steps with a peak located in the main decomposition area, around 300 °C, moved back and form the visible shoulder. Another possible explanation is that at slow heating rates, less than 10 reactions are governing decomposition, as pyrolysis mechanism is dependent on heating rate, and shoulder is a result of "lack of space" in decomposition range. On the other hand, isoconversional Friedman method predictions provided an excellent fit to experimental data without reaction model assumption, where all kinetic information was encrypted in isoconversional kinetic parameters, valid for investigated SS sample.

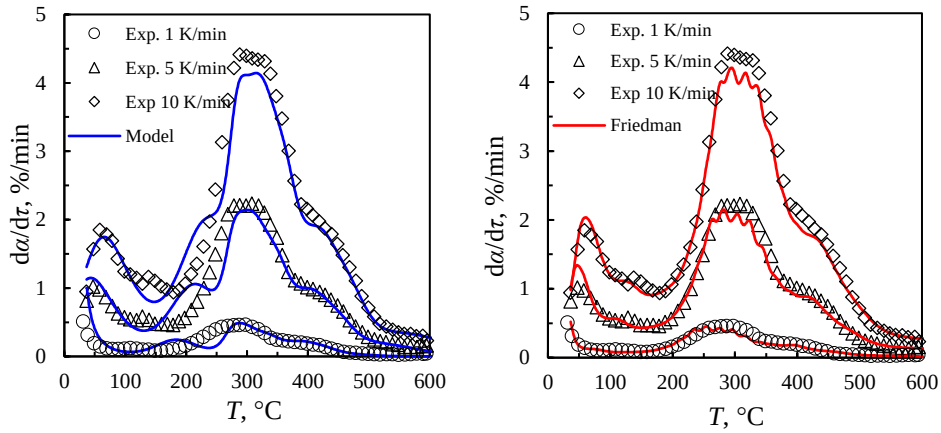

Fig. 6.21. 10 independent reaction kinetic model and Friedman method predictions compared to TGA profiles at 1, 5 and 10 K/min.

6.4. Kinetic analysis of the waste straw pyrolysis based on deconvolution techniques

Kinetics of the last biomass type pyrolysis, WS, are presented as last after the introduction to the classical theory of model-fitting kinetics and modern isoconversional kinetics. The reason for that is to provide a brief comparison of classical approach to kinetic solution and alternative one, based on solely numerical method. The difference is subtle, classical kinetic computations still need a numerical method, usually least squares method, to finally optimize Arrhenius parameters to provide the best fit to experimental data.

Nevertheless, deconvolution are gaining attention due to significant advantage of providing unambiguous elementary conversion profiles based on mathematical root functions. Obtained profiles are later mapped with Arrhenius equation with assumption of simple 1st or nth order reaction model, yielding accurate values of *E*, *A*, and reaction orders. Presented work was not published in any Journal so far, and is considered as the newest input for this dissertation.

6.4.1. Deconvolution results for 3-step Gaussian function independent model

The deconvolution algorithm used for the kinetic analysis of the WS pyrolysis was *peakfit.m* user function implemented in the Matlab environment. The first input for the deconvolution computations is a two-column array forming a conversion profile from a number of *x* experimental points of conversion rate as a function of temperature $[d\alpha/d\tau : T]_x$. Second parameters are a number of elementary steps, type of function to fit, and potential peaks positions, which can be determined numerically. The algorithm looks for the parameters fulfilling the criteria of the best fit ($R^2 \rightarrow \max$). As soon as *peakfit.m* input is provided, the function presents a deconvoluted elementary steps, which sum mimics the experimental conversion profile.

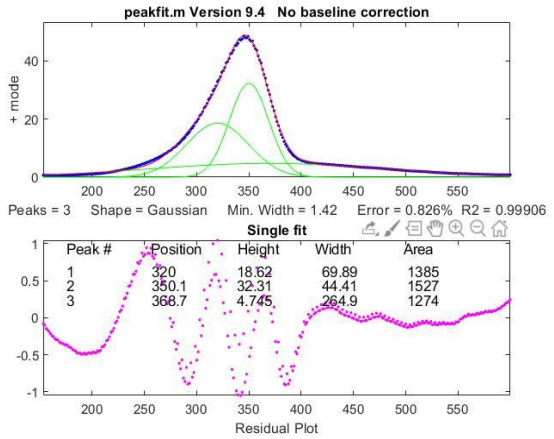

Fig. 6.22. Plot of the peakfit.m deconvolution results with 3 step Gaussian function (R^2>0.99) for WS pyrolysis at 40 K/min.

Fig. 6.22 presents the output from the *peakfit.m* function as a plot of numerical deconvoluted profiles against provided input profile, WS pyrolysis conversion rate. The results for the 3 elementary steps, namely: *position*, *height*, and *width* are a parameters of the Gaussian

function-based elementary steps, shown as the bright green profiles as a function of the temperature.

6.4.2. Inverse decryption of Arrhenius kinetic parameters based on simulated conversion profiles

Having completely determined numerical elementary profiles, once can inversely determine the actual kinetic parameters governing the process using simple procedure in any spreadsheet *e.g.*, MS Excel. Now, the plotted Gaussian profiles are the target to the fitting procedure of the elementary kinetic steps based on Arrhenius rate equation. Variables are the *E*, *A*, and *n*, while the target function for Solver is minimization of the residual sum of squares of the Gaussian profiles and modelled kinetic steps.

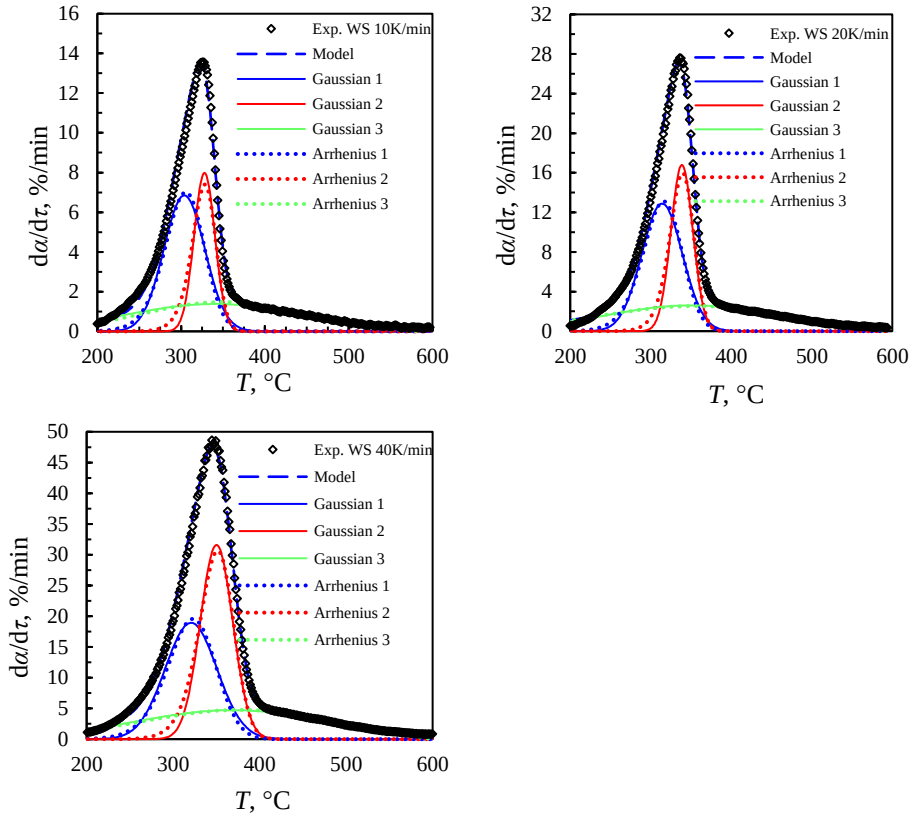

Fig. 6.23. Modelled WS pyrolysis conversion profiles based on Gaussian deconvolution procedure.

Table 10: List of deconvolution parameters and corresponding kinetic parameters describing WS pyrolysis.

β, K/min	*Step 1: p-hemicellulose*						
	Shape	Position, a_1	Height, a_0	Width, $2 \cdot a_2$	E, kJ/mol	A, min^{-1}	n, -
10 K/min	*Gaussian*	303.83	6.85	49.00	141.26	1.17E+15	1.44
20 K/min	*Gaussian*	314.11	12.88	50.52	150.02	8.47E+14	1.53
40 K/min	*Gaussian*	320.69	18.92	59.88	134.72	4.23E+13	1.60
				Mean	142.00	6.86E+14	1.52
				±	6.27	5.81E+14	0.06
β, K/min	*Step 2: p-cellulose*						
	Shape	Position, a_1	Height, a_0	Width, $2 \cdot a_2$	E, kJ/mol	A, min^{-1}	n, -
10 K/min	*Gaussian*	327.91	7.99	24.86	233.94	3.55E+22	1.11
20 K/min	*Gaussian*	338.68	16.80	27.15	251.35	1.15E+23	1.25
40 K/min	*Gaussian*	350.14	31.61	37.55	195.93	2.07E+18	1.32
				Mean	227.07	5.02E+22	1.23
				±	23.14	4.81E+22	0.09
β, K/min	*Step 3: p-lignin*						
	Shape	Position, a_1	Height, a_0	Width, $2 \cdot a_2$	E, kJ/mol	A, min^{-1}	n, -
10 K/min	*Gaussian*	339.98	1.38	213.59	25.01	3.17E+02	1.02
20 K/min	*Gaussian*	350.63	2.61	214.67	23.09	4.02E+02	0.91
40 K/min	*Gaussian*	368.28	4.71	224.01	27.75	1.69E+03	1.00
				Mean	25.28	8.02E+02	0.98
				±	1.91	6.27E+02	0.05

Table 23 lists the deconvolution functions parameters with corresponding classical Arrhenius parameters governing WS pyrolysis. Interestingly, the algorithm for pre-set 3 steps model presented elementary profiles that corresponds to decomposition regimes of the cellulose, hemicellulose and lignin, thus steps 1, 2, and 3 are assigned to pyrolysis of *p-hemicellulose* (pseudo-hemicellulose), *p-cellulose*, and *p-lignin*.

Results of Gaussian deconvolution gave foundation for three step independent reaction model describing WS pyrolysis with excellent fit quality, presented in Fig. 6.23.

Gaussian function, due to it's simplicity and unambiguity of form with minimum number of random variables, gives unambiguous kinetic results with accurate values of *E* and *A*, for reasonable values of the reaction orders *n*. What's more Gaussian function among other root functions reported in the literature (Weibull, Lorentzian or Fraser-Suzuki) due to it's symmetric-bell shape accurately resembles 1st and nth order reaction model based kinetic conversion profiles, and should be applied to kinetic deconvolution first. This similarity provides great synergy for optimization procedure, as the shape criteria is fulfilled, solver algorithm can unambiguously look only for values of *E*, *A*, and *n*. Quite the opposite situation occurs when deconvolution of overlapped conversion profile is carried out for non-symmetrical function like Lorentzian or Fraser-Suzuki. Due to higher degree of freedom of the mentioned root function, ambiguity of the results increases, and issue of stiffening of the optimization criterion occurs. Simple reaction models based on reaction orders cannot mimic highly non-symmetrical conversion profiles without arguable values of kinetic parameters. This phenomenon must be countered with adaptation of more complex *f(α)* functions e.g., Diffusion, Avrami-Erofeev (nucleation), or complex power law models. Of course, some pyrolysis cases of complex materials cannot be effectively solved with Gaussian function, so the challenge of adaptation of complex root functions is inevitable. However, if one can, one should aim for the simplest solutions based on the simplest *f(α)* functions, trying to provide as unambiguous and uncompensated with complex variables values of *E*, and *A* as possible.

6.5. Isoconversional, *model-free* pyrolysis rate modelling

6.5.1. Comparison of the isoconversional kinetic parameters of different feedstock pyrolysis

Isoconversional methodology for Friedman method calculation consisted of several steps. First, apparent activation energy E_α from the slope of isoconversional lines presented in Figs. 16, 17, and 18 for SS, WS, and WW respectively. Lines were plotted as linear regression fitting for constant α for 5 $\log(d\alpha/d\tau)$ versus reciprocal temperature for 5 examined heating rates. Apparent pre-exponential factor A_α was determined using the compensation effect [110] for A_j values calculated from the intercept of isoconversional lines with an assumption of 1st order reaction model as *f(α)* in equation (8). The choice of 1st order reaction model was based on the isoconversional methodology presented by Vyazovkin in his book [105] where despite lack of reaction model assumptions beforehand, isoconversional methods still assume that reaction obeys some *f(α)* at narrow temperature interval. Finally, A_α values were decoded from a linear equation for the E_α argument given for each feedstock at Figs. 6.27-6.29 for SS, WS and WW respectively.

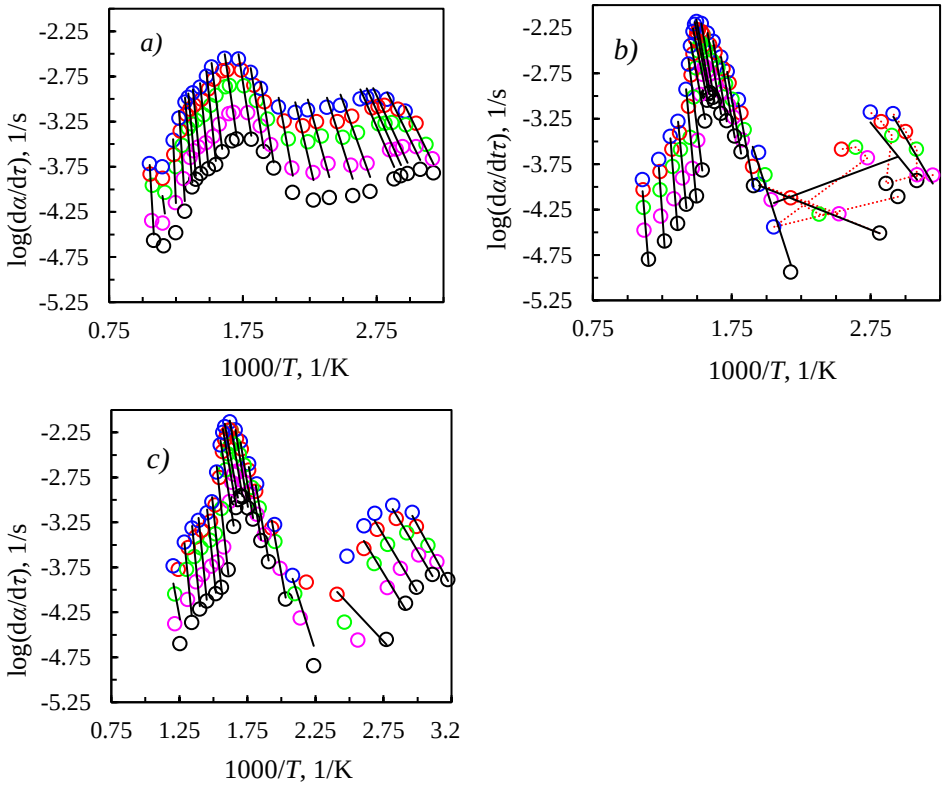

Fig. 6.24. Isoconversional lines for a) SS, b) WS, and c) WW pyrolysis for selected heating rates 5 (black), 10 (magenta), 20 (lime green), 30 (red) and 40 (blue) K/min.

Linear compensation effect

Figs. 6.25 and 6.26 presents linear compensation plots for investigated pyrolysis of SS, WS and WW respectively. First, deviations denoted in linear fitting of ln(A) and E_α for the SS resulting in R^2 not exceeding 0.97 with bulk approach are clear sign that process involves more than one step. Interestingly, 3 steps can be distinguished from the general linear compensation plot of the SS kinetic parameters, and after separation, the R^2 significantly increases for the first two pseudo-stages of the decomposition, while the last step provides the least accurate fitting with R^2=0.8689, at a level of experimental noise during TGA analysis. Still, the apparent values of pre-exponential factors A_α, assumed as the dominant, apparent frequencies governing the pyrolysis are calculated from linear fittings and presented in further Figs. 6.27-6.29.

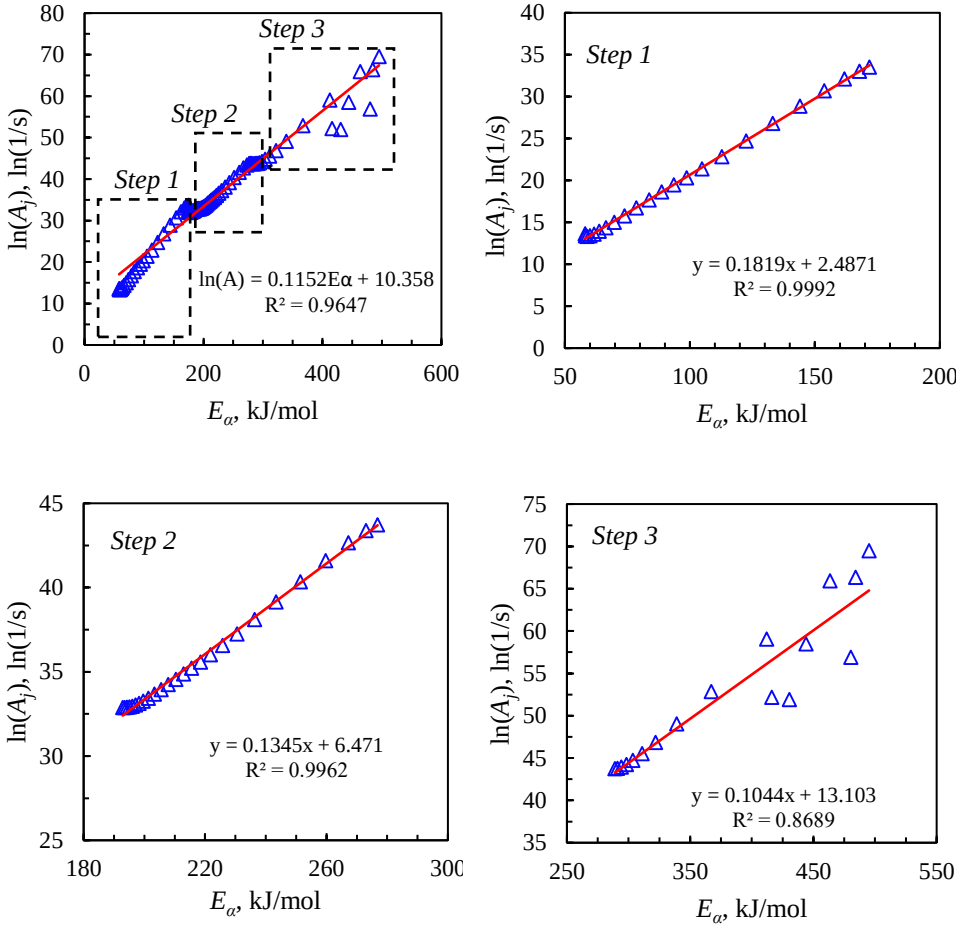

Fig. 6.25. Linear compensation plot for SS pyrolysis evaluated with Friedman method.

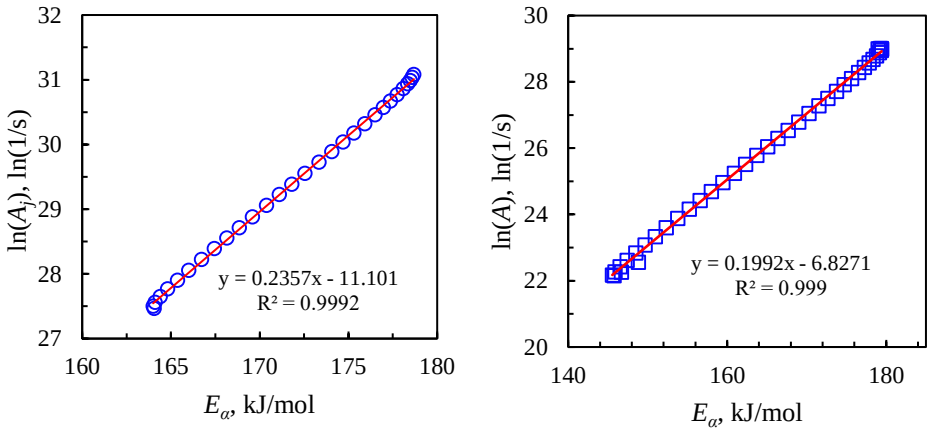

Fig. 6.26. Linear compensation plot for a) WS, and b) WW pyrolysis evaluated with Friedman method.

4.2.2. Apparent activation energies and pre-exponential factors

Based on the isoconversional methodology conversion dependency of E_α and A_α was determined for each investigated feedstock. Again, the biggest differences can be denoted comparing feedstock as lignocellulosic (WW and WS) against municipal-waste-derived SS. E_α and A_α describing SS pyrolysis are presented in Fig. 22. SS E_α profile starts with 58.1 kJ/mol for moisture evaporation and gradually starts to increase with a pyrolysis extent. Three bank points can be differentiated, first at α=0.25 profile 178.1 kJ/mol, second at α=0.77 profile 273.0 kJ/mol, and last, at arguable range α=0.95 with 495.1 kJ/mol, having a very high standard error. The standard error most likely may arise from either the change of decomposition "step" given by the drastic change of inclination angle of isoconversional lines or thermoanalytical (instrumental) noise. The following A_α profile shows a highly increasing trend. Minimum values are denoted at the beginning of the conversion, and with the further reaction extent, values of A_α are growing powerfully to a maximum at $1.12 \cdot 10^{31}$ min^{-1}. WW and WS kinetic parameters profiles presented in Figs. 23 and 24 respectively present a somewhat similar pattern. Again, both WW and WS E_α profiles start at 52.9 and 49.1 kJ/mol at moisture evaporation step, in which activation energy is similarly investigated feedstock. Both lignocellulosic biomass types E_α profiles reached relatively plateau at main decomposition, WS with values 153.6-176.1 kJ/mol at conversion range 0.1-0.8 after which E_α values drastically increase, followed by a standard error. WW pyrolysis "primary" decomposition reached a plateau between 164.7-178.3 kJ/mol at α range 0.11-0.55 with slightly decreasing linear trend dropping to 146.7 kJ/mol at α=0.88. Again, at the E_α values increases with pattern following standard error. Especially

interesting are decrypted values of actual pre-exponential factors A_α for WS and WW. Each profile presented visible maximum at mid-range of the α, with simultaneous low standard error, what may lead to a conclusion, according to kinetic collision theory, that A_α profile shown a clear maximum rate of the process, with the highest frequency of molecules collisions. As A_α calculation was strictly based on E_α values and linear compensation, the increasing trend at the end conversion is followed as well.

Having both calculated accurate E_α and A_α values one can start to evaluate the last of the kinetic triplet, the reaction model $f(\alpha)$. As both isoconversional activation energy and pre-exponential factor are presented as conversion dependent functions, the $f(\alpha)$ will be no different, calculated according to Eq.(5.24) as actual or process-resultant value for specific α for each biomass type.

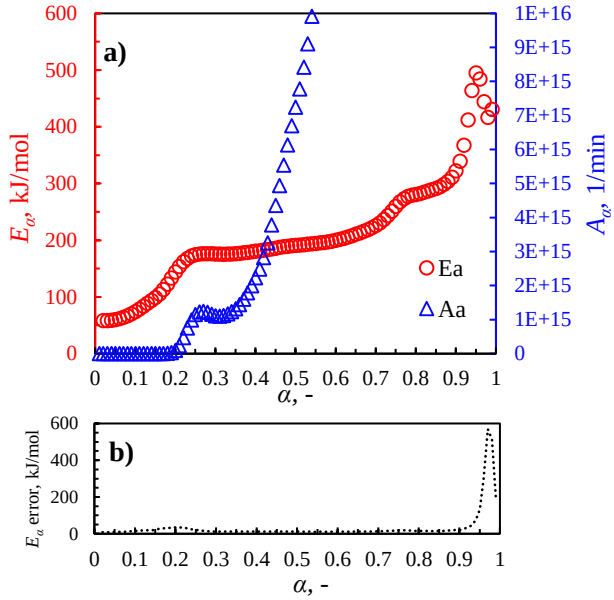

Fig. 6.27. a) E_α and A_α profiles for SS pyrolysis b) with standard regression error.

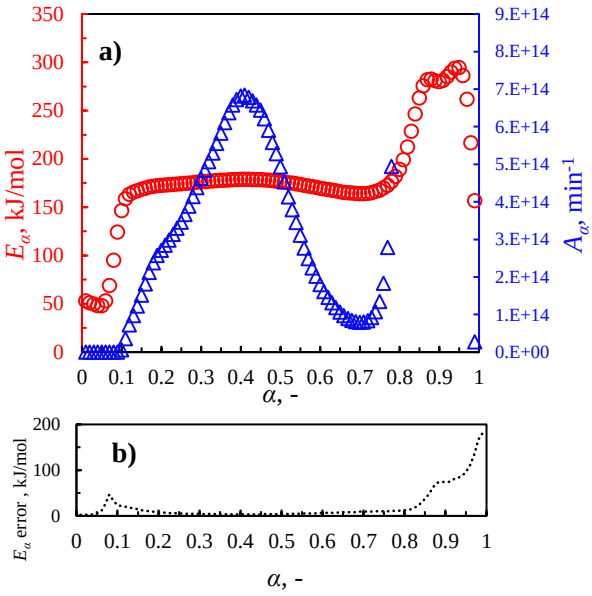

Fig. 6.28. a) E_α and A_α profiles for WS pyrolysis b) with standard regression error.

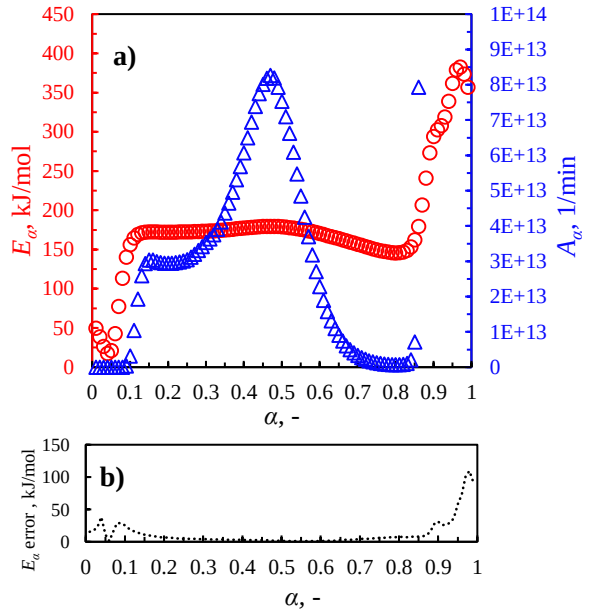

Fig. 6.29. a) E_α and A_α profiles for WW pyrolysis b) with standard regression error.

6.5.2. Master-plot methods results for the investigated feedstock pyrolysis

Calculated generalized rate plot fittings to known reaction models are presented in Fig. 6.30 for SS, WS, and WW pyrolysis. Deaccelerating behavior of the processes was denoted based on good fit to theoretical diffusion models for wood and straw, while sewage sludge theoretically obeyed order based model Fn, which both are known as a model example of deaccelerating kinetics [104], yet no unambiguous match was achieved to describe pyrolysis explicit reaction model. Both lignocellulosic biomass types pyrolysis, WS and WW, shown similarities with 3-dimensional diffusion (D3) model at the beginning of the conversion, with deviation from the theoretical profile at α>0.6. Biomass pyrolysis is widely known as a complex process, involving numerous reactions, which interactions can cause a change in the course of the master plot fittings. SS analysis resulted in fitting to controversial high reaction order model, however, Stolarek and Ledakowicz [135] believe that high-order reaction models are typical for lumped systems being a medium consisting of a number of first-order reactions, having gradually increasing activation energies, what in case of such complex material as sewage sludge seems reasonable, and was proved in previous work [121]. However, no matter high the reaction order, the physical explanation of 8 or 11 molecules collisions forming a product is rather doubtful. Even with high reaction order assumption to the complex decomposition of SS pyrolysis, the single-step kinetic approximation is rather an oversimplification.

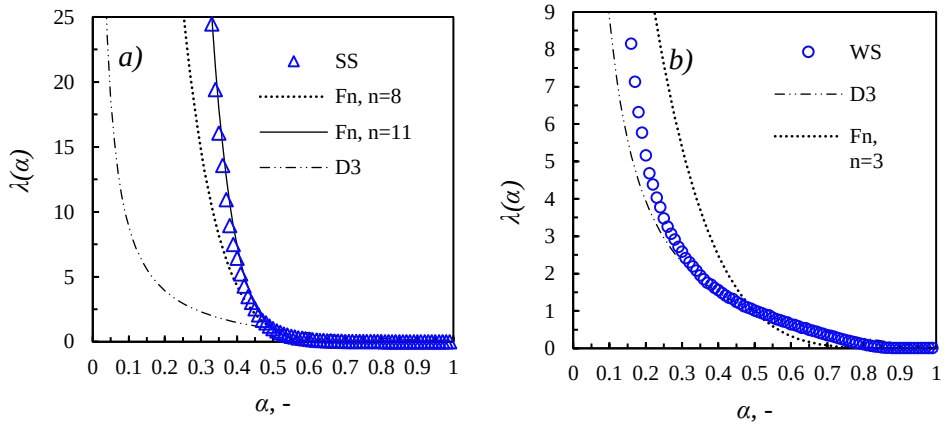

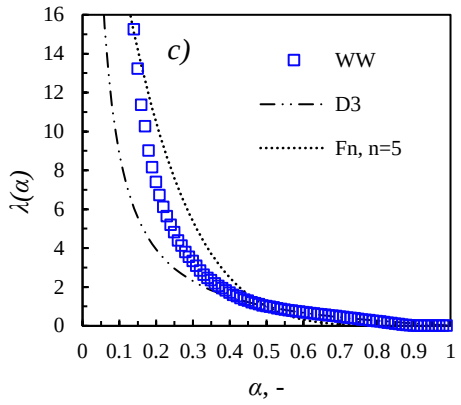

Fig. 6.30. Generalized reaction model fitting to theoretical reaction models for a) SS, b) WS, and c) WW pyrolysis.

6.5.3. Isoconversional reaction models

Denoted inconsistencies in master plot results describing selected biomass types pyrolysis led the authors to verify the usefulness of actual isoconversional reaction models [110]. Again, the *f(α)* presented in Fig. 6.31 for SS, WS, and WW respectively, were calculated according to Eq. (5.24) with E_α and A_α for each α step for specific biomass type. Virtually, each specific *f(α)* obtained for a single heating rate covers and compensates each error fulfilling the ratio of $d\alpha/d\tau$ to isoconversional *k(T)*, Eq. (5.24), providing theoretical R^2 fit equal to 1 for each single heating run. Actual *f(α)* are enhanced with an estimator of standard deviation calculated for t-Student distribution for a 95% confidence interval, based on results for each heating rate. Calculated apparent profiles of *f(α)* consists of a momentary values of the reaction models governing pyrolysis process at specific moment. Each specific value contains an information about average *f(α)* of all reactions occurring or the most dominant one, just like apparent E_α and A_α. SS derived *f(α)* presented a high peak at α=0.25 with the highest deviations, and two small peaks at the end of conversion at α=0.75 and α=0.93. WS and WW presented similar patterns with high peaks at α=0.15 and one smaller peak at the α=0.85 and α=0.89 for WS and WW respectively. Denoted peaks of isoconversional *f(α)* at the end of the conversion range strictly follows the standard errors of the E_α presented before in Figs. 6.27-6.29, presenting strong compensating ability. To verify the usefulness of obtained *f(α)* profiles, its actual values along with specific isoconversional E_α and A_α and substituted to form conversion rate and plotted against experimental $d\alpha/d\tau$ for each feedstock.

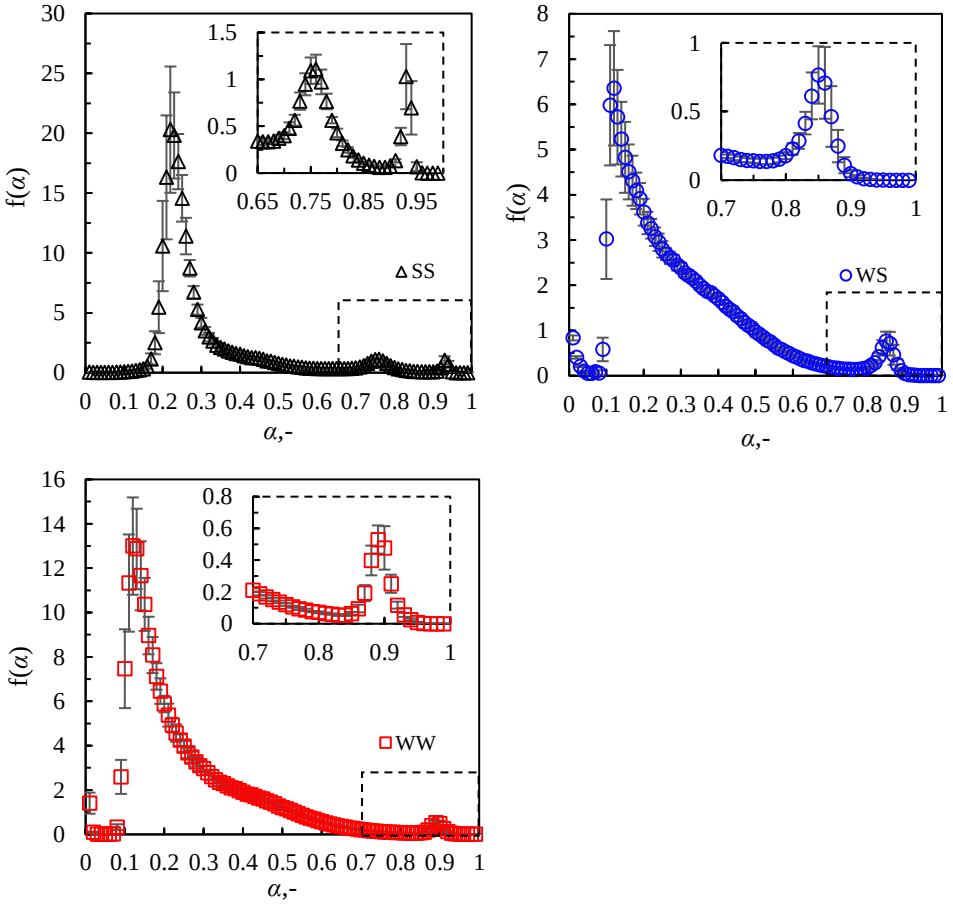

Fig. 6.31. SS, WS, and WW pyrolysis apparent f(α) profiles with standard deviation given for 95% confidence interval.

6.5.4. Isoconversional modelling of biomass conversion rate profiles

As a method of kinetic triplet verification, given in Table 23, the attempt of modelling SS, WS, and WW pyrolysis conversion rate profiles with comparison to experimental results is presented in Figs. 6.32-6.34. Each figure consists of 5 plots of calculation results plotted against experimental $d\alpha/d\tau$ for each heating rate of every feedstock type, summarized with non-linear R^2. First, Fig. 6.32 presents modelled by isoconversional kinetic triplets SS pyrolysis conversion rate profiles. Amongst selected

biomass types, SS pyrolysis modelling resulted in the highest deviations, thus the lowest R^2=0.9406, yet presented method well evaluated each of the wide and overlapped peaks and shoulders. The highest errors at the end of the conversion for the lowest heating rates, 5 and 10 K/min are a result of probable instrumental errors araised at the longest TGA experiments in terms of single run time, and the most complex nature of the feedstock consisting of fats, carbohydrates, fatty acids, and protein-derived wastes [162]. Significant overestimation of conversion rate can be observed at the highest heating rate, 40 K/min, where conversion profile at main decomposition range overcalculated experimental values by average 2.5 %/min. The excellent fit was achieved for modelled conversion rate profiles for WS (Fig. 6.33) and WW (Fig. 6.34) with R^2 0.9876 and 0.9912 respectively. Information contained in isoconversional kinetic triplets well-evaluated moisture evaporation (except high errors denoted for WW pyrolysis at 10 K/min) as well as the main decomposition range. Marked errors for WW pyrolysis at 10 K/min can be caused by inconsistent decomposition during TGA resulting with the highest deviation between the expected value of *f(α)*.

Table 23: Isoconversional kinetic triplets describing pyrolysis of investigated feedstock.

	WS			WW			SS		
α	E_α, kJ/mol	A_α, 1/min	*f(α)*	E_α, kJ/mol	A_α, 1/min	*f(α)*	E_α, kJ/mol	A_α, 1/min	*f(α)*
0.01	52.9	7.2E+06	0.836	49.6	9.1E+05	1.409	58.1	1.5E+09	0.032
0.05	48.1	3.5E+06	0.052	21.0	1.6E+04	0.001	61.7	2.3E+09	0.020
0.1	146.4	6.1E+12	3.018	156.3	3.2E+12	7.470	78.6	1.6E+10	0.063
0.15	168.4	1.5E+14	4.828	172.3	3.0E+13	10.368	104.9	3.3E+11	0.322
0.2	172.4	2.7E+14	3.616	172.1	2.9E+13	5.875	153.8	9.3E+13	10.580
0.25	174.1	3.5E+14	2.794	172.3	3.0E+13	3.970	175.6	1.1E+15	14.564
0.3	176.1	4.6E+14	2.385	173.4	3.5E+13	2.957	175.3	1.1E+15	4.158
0.35	177.6	5.8E+14	1.997	174.9	4.4E+13	2.285	176.8	1.3E+15	2.094
0.4	178.7	6.8E+14	1.700	177.2	6.1E+13	1.889	181.3	2.2E+15	1.536
0.45	178.3	6.4E+14	1.327	179.2	8.0E+13	1.587	187.1	4.4E+15	1.191
0.5	176.5	4.9E+14	0.974	178.8	7.5E+13	1.207	191.5	7.2E+15	0.772
0.55	173.3	3.1E+14	0.671	175.6	4.8E+13	0.860	195.1	1.1E+16	0.465
0.6	169.6	1.8E+14	0.437	170.3	2.3E+13	0.566	201.3	2.2E+16	0.345
0.65	166.0	1.1E+14	0.283	163.7	9.0E+12	0.356	212.9	8.5E+16	0.341
0.7	164.0	7.9E+13	0.182	156.6	3.3E+12	0.213	230.5	6.5E+17	0.399
0.75	167.6	1.3E+14	0.141	149.7	1.2E+12	0.121	267.2	4.4E+19	1.092
0.8	189.2	3.1E+15	0.179	145.6	6.9E+11	0.072	282.4	2.6E+20	0.428

0.85	263.0	1.5E+20	0.767	162.1	7.1E+12	0.065	294.2	9.9E+20	0.105
0.9	279.8	1.8E+21	0.049	293.8	8.4E+20	0.478	339.1	1.7E+23	0.073
0.95	294.3	1.4E+22	0.001	361.8	1.2E+25	0.009	484.3	3.2E+30	0.069
0.99	156.6	2.7E+13	2.4E-06	356.9	6.2E+24	3.9E-07	480.3	2.0E+30	1.5E-06

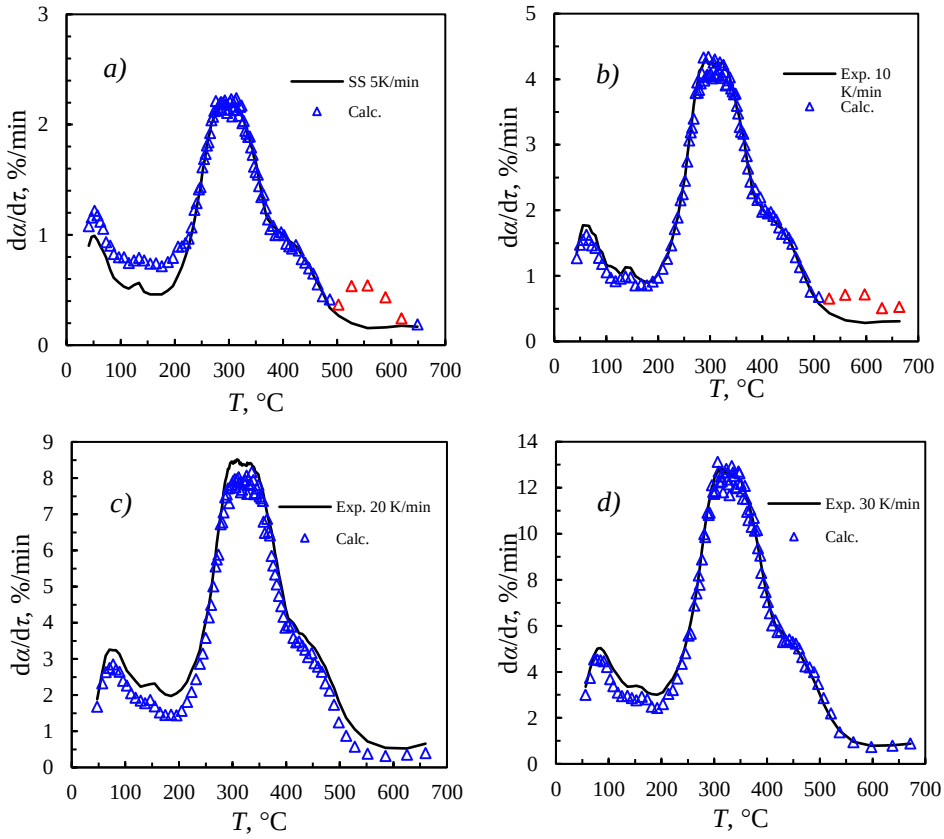

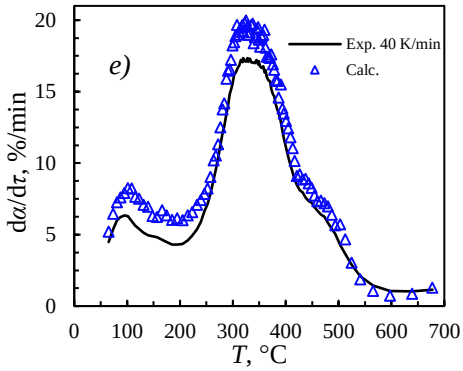

Fig. 6.32. SS pyrolysis conversion rate profiles calculated using isoconversional kinetic triplets to experiment results, R^2=0.9406, a) for 5 K/min, b) for 10 K/min, c) for 20 K/min, d) for 30 K/min, e) for 40 K/min.

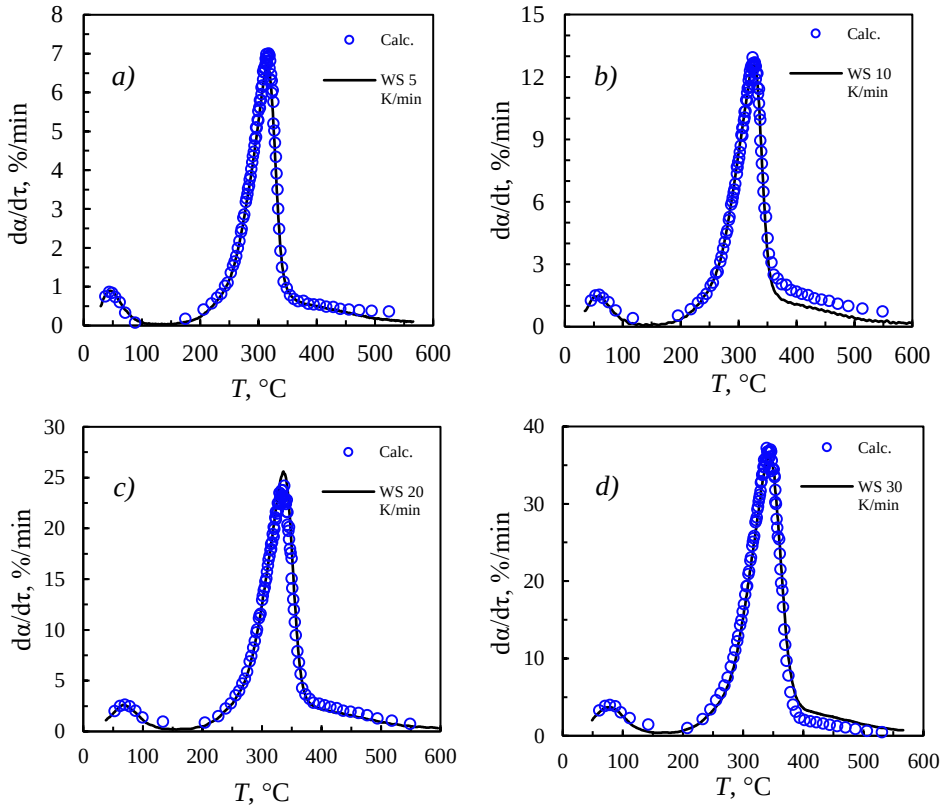

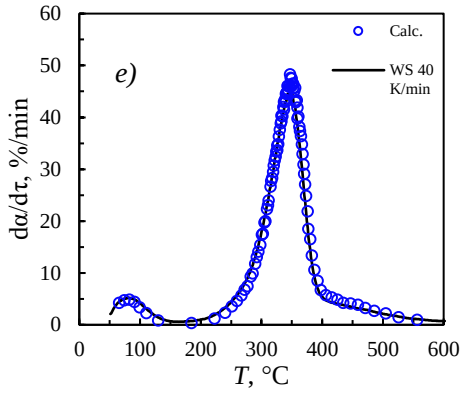

Fig. 6.33. WS pyrolysis conversion rate profiles calculated using isoconversional kinetic triplets to experiment results, R^2=0.9876, a) for 5 K/min, b) for 10 K/min, c) for 20 K/min, d) for 30 K/min, e) for 40 K/min.

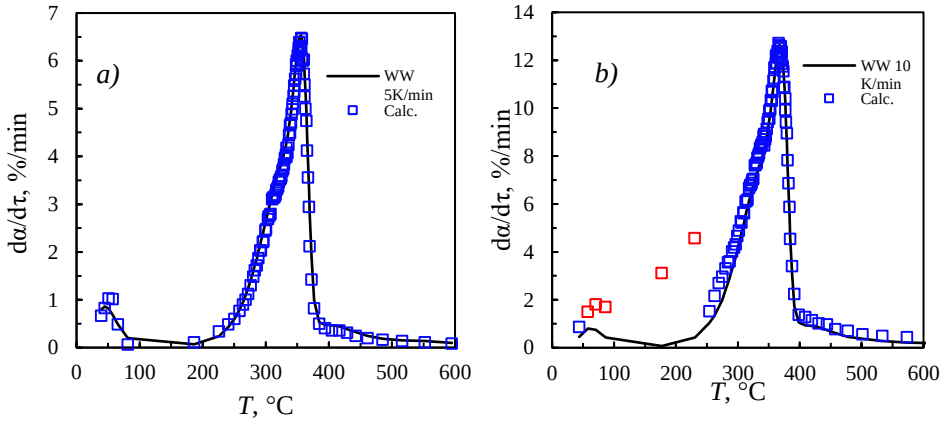

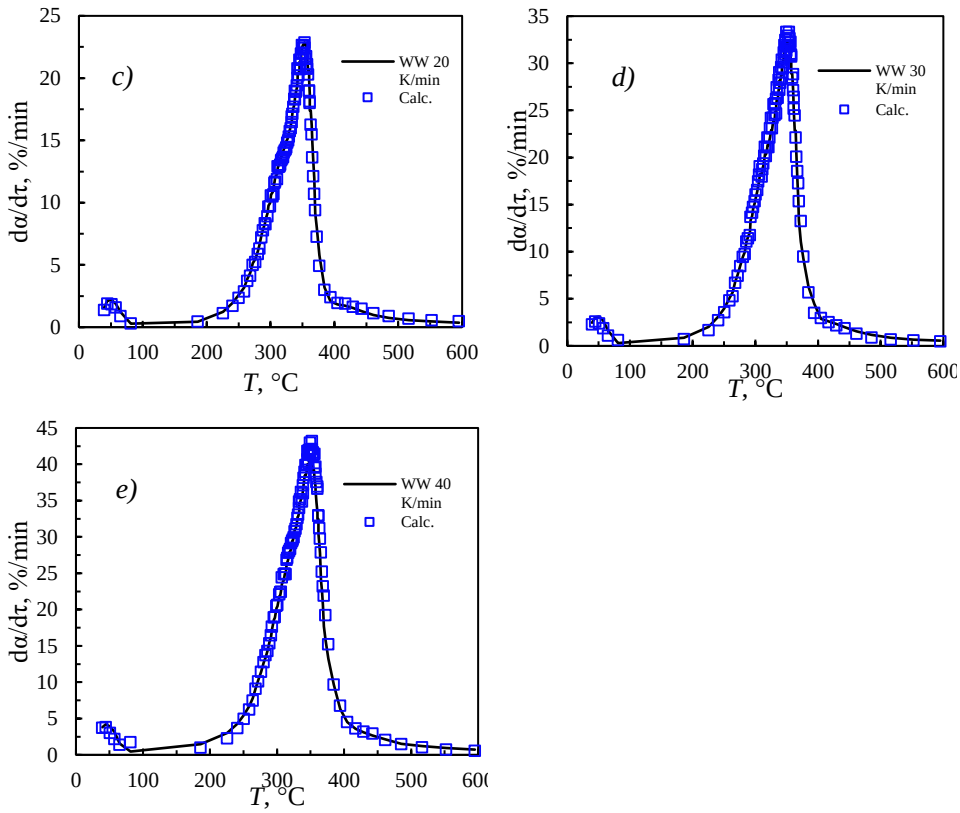

Fig. 6.34. WW pyrolysis conversion rate profiles calculated using isoconversional kinetic triplets compared to experiment results, R^2=0.9912.

6.5.5. Discussion of the isoconversional modelling results

Interestingly, modelled rate profiles for WS and WW pyrolysis resulted in final temperatures not exceeding 600°C. This phenomenon is strictly connected to the adapted isoconversional methodology, based on isoconversional triplets discretized over α ranging from 0.01 to 0.99 (Table 24). As the last modelled point is based on isoconversional triplet α=0.99, corresponding temperature is considered as a final one, in case of lignocellulosic biomass 600°C. Virtually each of presented mathematical model describing biomass pyrolysis presented acceptable or satisfactory fit according to R^2. R^2 calculation is based on a ratio of a sum of residual squares related to the total variance. In non-linear regression, the variance estimate Eq. (6.1) is usually much higher than the nominator, which is why

even poor kinetic models provide non-linear R^2 fairly high. Supplementing solution is a calculation of the standard error of the estimate, $\sigma_{est,}$ Eq. (6.2), being a more engineering-friendly evaluation of the model given as the same unit as the dependent variable. Table 25 lists R^2 and σ_{est} values for each feedstock pyrolysis at 5 heating rates.

$$R^2 = 1 - \left[\frac{\sum_{i=1}^{|\beta|=5} \sum_{j=1}^{|N|=99} \left(f(x)_{i,j} - y_{i,j} \right)^2}{\sum_{i=1}^{|\beta|=5} \sum_{j=1}^{|N|=99} \left(y_{i,j} - y_{avg.} \right)^2} \right] \tag{6.1}$$

$$\sigma_{est.} = \sqrt{\frac{\sum_{j=1}^{|N|=99} \left(f(x)_j - y_j \right)^2}{N}} \tag{6.2}$$

Table 24: The standard error of the estimated conversion rate and R^2 for isoconversional pyrolysis model.

β, K/min	$\sigma_{est.WS}$, %/min	$\sigma_{est.WW}$, %/min	$\sigma_{est.SS}$, %/min
5	0.198657	0.220348	0.131739
10	0.363725	0.692877	0.14025
20	1.305509	0.494788	0.493642
30	1.155443	0.758598	0.394945
40	1.842317	1.437177	1.764176
R^2	0.9876	0.9913	0.9406

As σ_{est} values are increasing with the increase of the β, an additional statistical parameter was formed to consider a simultaneous increase of dependent variable range, $d\alpha/dt$. Percentage error of the calculation, Δ presents the ratio of σ_{est} to an average value of $d\alpha/d\tau$ denoted at specific β (Fig. 6.35).

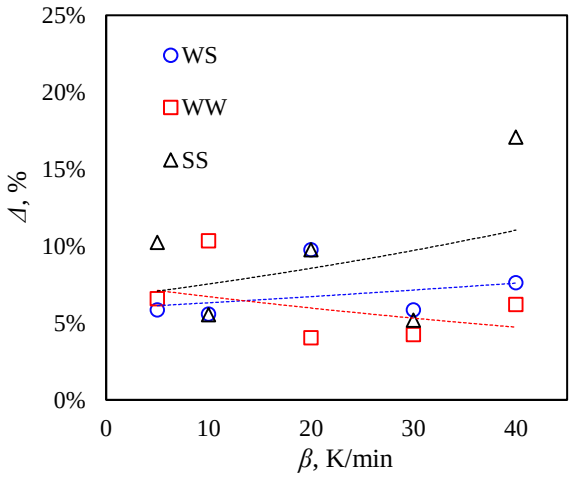

Fig. 6.35. Heating rate impact on the percentage standard error of the estimate related to average dα/dt denoted at each heating rate.

Table 25: Percentage error of calculation for isoconversional modeling of specific feedstock type pyrolysis.

	Δ, %		
β, K/min	WS	WW	SS
5	5.8%	6.6%	10.2%
10	5.6%	10.3%	5.5%
20	9.8%	4.0%	9.8%
30	5.8%	4.2%	5.2%
40	7.6%	6.2%	17.1%

Data presented in Tables 24 and 25 allow to accurately evaluate prepared mathematical models for the pyrolysis of WS, WW, and SS samples. Each of the models presented results with fit quality R^2 higher than 0.9, respectively 0.9876, 0.9912, and 0.9406 for WS, WW, and SS. However, an additional statistical parameter was calculated to evaluate model results for each of the heating rate. Fig. 6.35 presented values of model percentage error, *Δ,* for each heating run, with a very crude exponential trend line, just to show any trend that would show the heating rate dependency of the model deviations. It can be said that for WS isoconversional model yields fairly constant deviations, not dependent on the *β*, while WW and SS results show some negative and positive *β* correlation respectively. First, regarding the model for WS pyrolysis, calculation results deviate from

experimental values by 5.8-9.8 %, what for differential conversion profile over time is a very good result. WW pyrolysis model noted even lower deviations, from 4.0 to 6.6% with one high error at β 10 K/min, 10.3%. The σ_{est} for that specific heating rate revealed deviations in the decomposition route, at low temperatures and conversion , which was notified earlier, despite even the highest R^2 among the biomass species pyrolysis models. The probable explanation of this phenomenon is that sample examined at 10 K/min had lower actual moisture content, which is most likely results of heterogeneity of selected WW pellets sample for analysis, which is formed from wide range of waste-derived wood. The Isoconversional model for SS decomposition provided the lowest R^2 with σ_{est} 5.25% to as high as 17.1% for the highest heating rate of 40 K/min. SS pyrolysis was the slowest process with arguably the highest numbers of independent reactions occurrence providing the biggest signal noise during decomposition. However, the proposed method still provided meaningful results for even such complex feedstock as SS.

Overall values of the tested isoconversional kinetic model for three different waste biomass types pyrolysis can form a conclusion that is it possible to accurately recreate the rate of the pyrolysis as $d\alpha/d\tau$ without reaction model assumptions. It is crucial to mention, that the presented methodology does not need any significant computational effort, nor a computational time. Presented solutions can be applied for any type of feedstock in any environment (atmospheres) that can be evaluated in thermoanalytical measurements *e.g.*, TGA.

6.6. Solar pyrolysis experiments results

Within this part of the dissertation, extensive presentation of the solar pyrolysis experiment results are presented comprising: products characterization, yields, feedstock heating behavior and original approach actual heating rates profiles. Interestingly, kinetic results presented in previous part of the work, *i.e.*, model-free kinetic predictions, found reflection in the pyrolysis gas formation profiles, what has not been reported in the literature so far.

6.6.1. Temperature and heating rate profiles of the reacting feedstock

After the experiments, data recorded during three runs for each feedstock type were collected and evaluated. Recorded temperature profiles for each pellet were statistically evaluated with *t-distribution* for 90% CI, to obtain the expected temperature profile and standard deviation estimate for 6 observations. After expected values of feedstock, temperatures were obtained where the first temperature derivative over time was calculated as an actual heating rate of the feedstock ($dT/d\tau$) and the temperature profiles are presented in Figs. 6.36-6.38 for WW, WS, and SS, respectively.

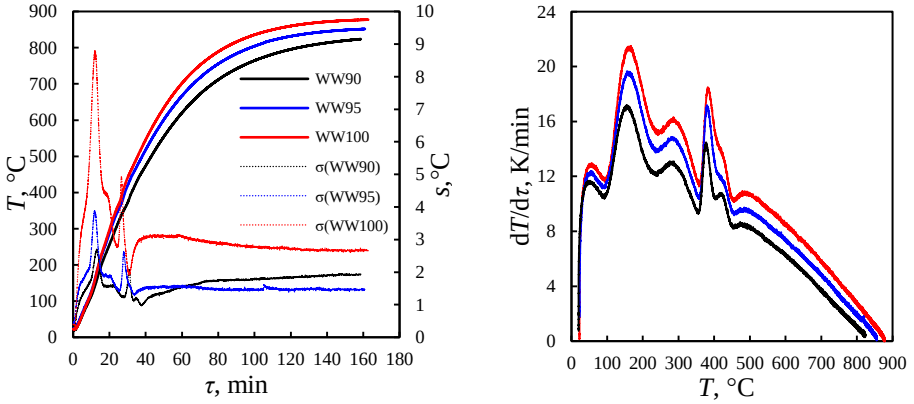

Fig. 6.36. Temperature profiles with confidence interval (left) and actual heating rates (right) determined during solar pyrolysis experiments for WW samples.

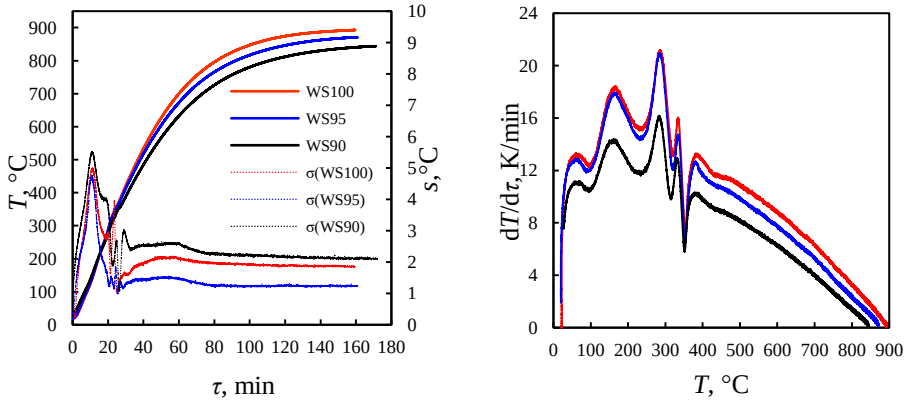

Fig. 6.37. Temperature profiles with confidence interval (left) and actual heating rates (right) determined during solar pyrolysis experiments for WS samples.

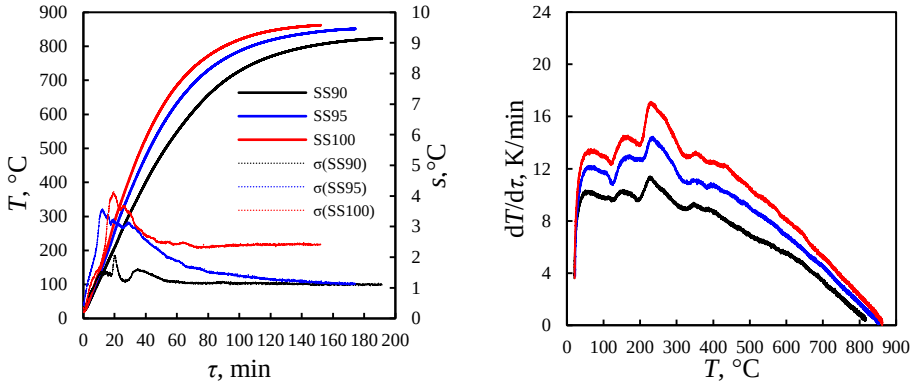

Fig. 6.38. Temperature profiles with confidence interval (left) and actual heating rates (right) determined during solar pyrolysis experiments for SS samples.

Proposed experimental method resulted in biomass heating from 160-190 min at variable xenon lamp power, with final feedstock temperatures exceeding 800 °C. Noticeable deviations of temperature recordings are observed at the beginning of pyrolysis, which is possibly caused by variations in moisture content of individual pellets. Additionally, during the primary volatiles release step at temperatures 200-400 °C, the highest mass loss of the sample is expected according to TGA data previously published [112,121,163]. The reports state that despite efforts to provide uniformity of samples, random heterogeneity of SS and random distribution of lignocellulosic structures within the biomass samples WW and WS can influence random changes in the decomposition behavior during the process. The highest deviations in thermocouples recording are found for WW decomposition, extending the confidence interval to 18 K deviation, and considering the complexity of the pyrolysis process it is reasonable and acceptable. Above 400 °C, the thermocouples deviations reach a stable level, 1-3 K for variable lamp powers and lasts until the end of the process.

More dynamic insight into pyrolysis behavior was achieved by calculating the actual heating rate profiles ($dT/d\tau$), presented on the right side of Figs. 6.36-6.38. Differential heating rate profiles present a dynamic course of heating behavior during the process. During the decomposition process the actual heating rates vary significantly, with the most intense changes being observed at 100-450 °C during primary volatiles release. Due to consistent heat supply from the reactor wall to the samples, it is proposed that any change in heating rate is caused by the chemical phenomena occurring inside the feedstock. Investigated samples of green-derived biomass cellulose, hemicellulose, and lignin shares are 54.8 wt.%, 11.8 wt.%, 27.9 wt.%, and 49.7 wt.%, 31.6 wt.%, 6.0 wt.% for WW and WS, respectively (Table 3). Regarding WW pyrolysis heating rate profiles, presented in Fig. 6.36, each experiment provides similar $dT/d\tau$ patterns. Momentary peaks of WW samples occur at the same temperatures, first at 57-63 °C corresponding to moisture evaporation, to

which extent could be expressed as a additional heat sink that "slowed down" further heating. After reaching 100 °C the heating rate significantly increases until the second peak temperatures at 163-174 °C, followed by the second lower peak at 293 °C and third very sharp peak at 383 °C accompanied by a visible shoulder. The shoulder at 400 °C moves towards higher temperature at 428 °C during the experiment at the lowest lamp power, namely 85.5%. Further heating was conducted at a continuously diminishing rate, until the end of the process. Fig. 6.37 presents WS temperature profiles recorded during solar pyrolysis experiments. WS samples exhibit similar heating behavior compared to WW. The first peaks are found at 78-81 °C, followed by a wide peak at 162-173 °C, and then two very sharp peaks at 291 °C and 335 °C, respectively. The last peak is followed by a significant drop in the heating rate at 351 °C. According to the literature regarding energy demand in the course of pyrolysis, cellulose behaves differently from hemicellulose and lignin [164]. The pyrolysis of the former is endothermic, with a very quick decomposition rate due to polymeric structure. Once the energy barrier is achieved higher yields of CO are produced, whereas pyrolysis of hemicellulose and lignin is exothermic, in which release of CO_2, CH_4, and H_2 occurs [155,165]. SS heating behavior shown in Fig. 6.38, displays a more random and less complex $dT/d\tau$ profile compared to WW and WS, both in terms of peak number and magnitude. The first wide peak is observed at 61-120 °C, which may be associated with the significant amount of moisture denoted in the proximate analysis of SS samples (Table 3). Furthermore, the complex moisture release nature for studied sludge was previously observed in the kinetic study of SS samples decomposition, which was examined at TGA for the same temperature range [121]. Compared to lignocellulosic biomass, SS heating rate peaks are non-symmetric and more irregular across the experiments. In the case of SS heating rates peaks positions, the second and third peak denoted are recorded at 140-170 °C and 242-250 °C.

Despite the complex pyrolysis behavior of the investigated samples, average heating rates calculated over the entire pyrolysis time ware similar, but dependent on the actual specific properties of the biomass types *i.e.*, thermal diffusivity. Actual heating rates observed for 90, 95 and 100% xenon lamp power are 4.51, 5.32, and 5.49 K/min for WS; 5.10, 5.19, and 5.37 K/min for WW; and 3.95, 4.48, and 5.25 K/min for SS, respectively.

6.6.2. Solar pyrolysis products shares and their characterization

Fig. 6.39 shows the cumulative results of the solar pyrolysis products distribution for WW, WS and SS investigated xenon lamp powers that are presented as a function of the resulting average heating rates. Selected experimental conditions impact on actual product yields is rather low, where resulting heating rates of the feedstock remains within the slow pyrolysis conditions with the highest shares of the liquid product [166]. During pyrolysis of each feedstock type a decreasing trend in the final solid residue is observed, where the

heating rate increases followed by higher final process temperature and enhanced char decomposition [31]. Regarding liquid products, by increasing the heating rate during WW and SS pyrolysis results in increasing trends of the liquid and decreasing final gas dry-yield. Generally, the gas and liquid product yields are contrasting due to secondary cracking of the vapors leading to dry, non-condensable gas formation [35]. This phenomenon can be observed during WS pyrolysis, where increasing heating rate influences enhancement of gas formation at the expense of liquid products due to catalytic metals present in biomass [76], as well as high cellulose and hemicellulose content (Table 3), leading to CO and CO_2 formation during pyrolysis [165]. In the case of char yields, the heating rate increase causes a slight decrease in final char yields, where 21.91 wt.%, 21.66 wt.%, and 21.21 wt.% for WW; 27.45 wt.%, 26.66 wt.%, and 27.08 wt.% for WS; and 39.54 wt.%, 38.53 wt.%, and 38.29 wt.% for SS. The highest char yields are observed for SS, which can be related to the highest ash content of the feedstock (33.44 wt.%), where that of WW and WS is 21.59 wt.% and 21.06 wt.%, respectively. The exact values of pyrolysis gas shares for WW solar pyrolysis are 9.74±0.67 wt.%, 9.20±0.65 wt.%, and 8.59±0.54 wt.%; for WS 8.77±0.83 wt.%, 11.65±0.96 wt.%, and 11.48±0.92 wt.%; for SS 10.50±1.37 wt.%, 9.15±0.88 wt.%, and 8.94±0.97 wt.% for increasing heating rates, respectively. The bio-oil yields are the highest shares denoted in the study, are 68.36 wt.%, 69.14 wt.%, and 70.20 wt.% for WW; 63.78 wt.%, 61.69 wt.%, and 61.43 wt.% for WS, and 49.96 wt.%, 52.32 wt.%, and 52.77 wt.% for SS, at investigated heating rates range.

Denoted product shares are consistent with the literature data. T. Kan et al. [167] reviewed lignocellulosic biomass pyrolysis focusing on process parameters on numerous factors, including product shares and bio-oil elemental composition. Product yields of WW and WS correspond well to the data presented for Hardwood pyrolysis (liquid yields 50-55 wt.%, char 25-27 wt.%, gas *not given*), and Switchgrass (liquid 60.7 wt.%, char 12.9 wt.%, and gas 11.3 wt.%), at similar heating rates 6 K/min and temperature ranges. The reports state that the samples were similar in terms of cellulose, hemicellulose, and lignin content. Another study referenced the shares of wood slow pyrolysis, however, at isothermal 425 °C as 27 wt.%, 51 wt.% and 22 wt.% shares for gas, oil, and char respectively [168]. Regarding SS product yields, similar tendencies were observed by J. Alvarez et al. [169] for SS pyrolysis at 500 °C using a conical spouted bed reactor. The final shares of char, liquid, and gas were 45 wt.%, 50 wt.%, and 5 wt.%, respectively. Moreover, a similar elemental composition of the bio-oil was described.

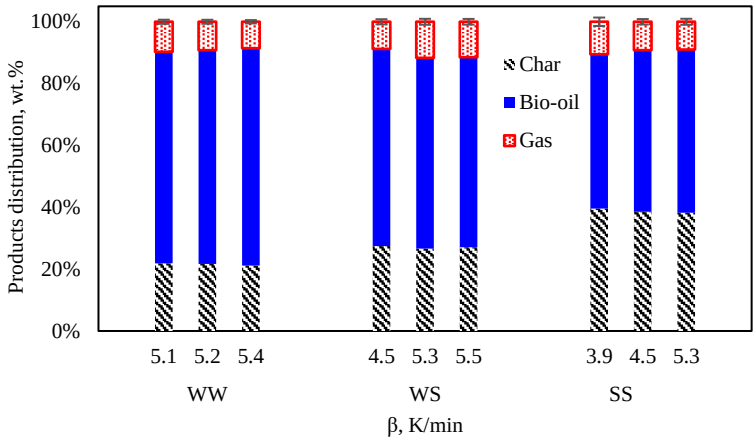

Fig. 6.39. Solar pyrolysis products distribution of investigated feedstock.

6.6.3. Biochar

After solar pyrolysis experiments the obtained chars for WW, WS, and SS were analyzed in terms of elemental composition *C, H, N, O*, and porosity by BET surface area measurements. Fig. 6.40 shows the impact of pyrolysis conditions on BET surface area of the obtained char samples, which are compared to raw feedstock pellets. Due to the pelletization process, involving relatively high ~60-80 °C temperature formation of the dense-packing matter in pellets, BET area of the raw feedstock is very low, 0.21, 0.52, and 0.55 m^2/g for WW, WS, and SS, respectively. Despite the small change in investigated heating rates, the adapted method for experiment termination resulted in significant differences in final feedstock residence times, which may strongly impact the final BET area of the solid product. Table 26 lists ash deformation temperatures of WW, WS, and SS using a microscopic – photographic method, according to CEN/TS 15370-1:2007 standard. The highest specific surface area denoted in the study is observed for WW sample at 5.2 K/min, with BET surface area of 145.09 m^2/g from the experiment with 95% xenon lamp power. SS chars present a slightly increasing trend of BET area with increasing heating rate, but it did not exceed 43 m^2/g. Almost identical values are reported by J. Alvarez for SS pyrolysis char BET 42.9 m^2/g under similar experimental conditions [169]. WS samples porous structures are probably destroyed during pyrolysis, because the final process temperatures exceed the ash shrinkage deformation temperatures of WS (Table 26). During WS solar pyrolysis experiments temperature of ash shrinkage 690 °C is reached after 60-80 min in every experimental run for WS (Fig. 6.40). After reaching shrinkage temperature,

the temperature of the sample was increasing for more than 1 h towards ash deformation temperatures, which possibly destroyed any porous structures in WS chars. SEM photos of the selected bio-chars samples from experiments with 90% of the xenon lamp power are presented in Fig. 6.41. Resolution of the photographs was set to 100 μm. It can be seen that the WW scanning picture captured the high porosity plant cell wall area what corresponds to the BET area results presented in Fig. 6.40. Similar patterns can be seen for the SEM photos of the WS sample, however, no visible pores can be denoted. Interestingly, photos of the SS chars shows rock-like particles what resembles the is a mineral and ash residue after devolatilization during the process.

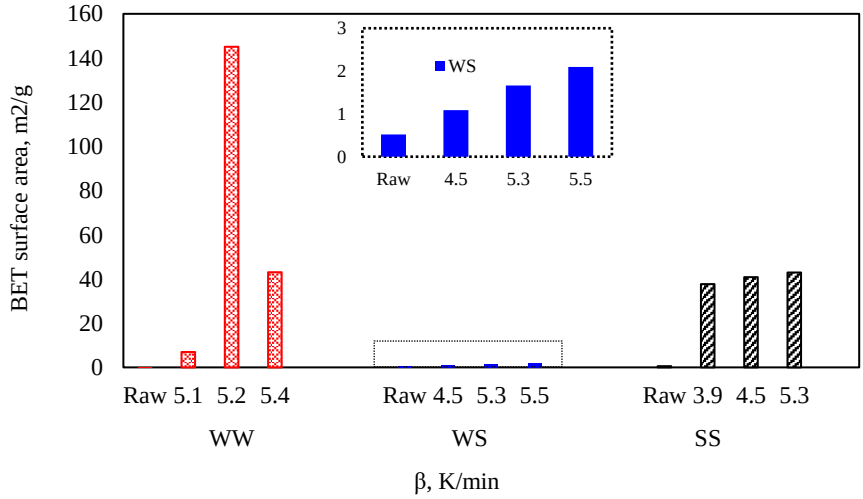

Fig. 6.40. Impact of heating rate on char BET surface area.

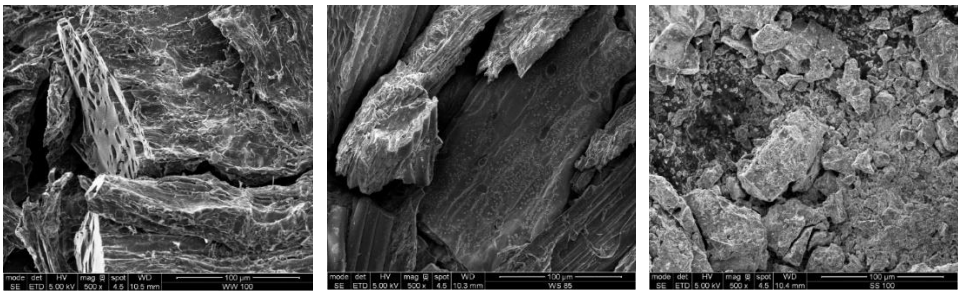

Fig. 6.41. Microstructures SEM photos for WW, WS and SS biochars (from left to right).

Table 26: Specific ash deformation temperatures under inert atmosphere for the investigated feedstock.

Ash fusion specific properties	WW	WS	SS
Shrinkage temperature, SST, °C	1140	690	860
Deformation temperature, DT, °C	1180	810	1010

Fig. 6.42 displays changes in the elemental composition of the feedstock with increasing solar pyrolysis, and expressed by xenon arc lamp power. A significant increase in *C* content is observed for lignocellulosic feedstock, WW and WS, with a simultaneous decrease of *O*, that significantly improves HHV of chars compared to the raw biomass. Final shares of elemental *C* in WW and WS are 87.90 wt.% compared to 49.31 wt.% of raw WW, and 69.67 wt.% for WS chars compared to 47.02 wt.% raw WS, which displays significant elemental *C* content increase. H content in solar pyrolysis chars is lower in comparison to the raw feedstock by average of 4.04-4.57 wt.%. Elemental *N* content slightly increases for chars from WS and WW by 0.3-0.5%, while a significant decrease is observed for SS chars by average of 4.11 wt.%. This can be explained by *N* migration to the bio-oil, whose elemental composition is presented in Fig. 68 [166]. After pyrolysis, the moisture and volatiles content containing a significant amount of *H* and *O* is reduced, increasing the relative carbon content within the sample. In addition, lignocellulosic biomass during pyrolysis, due to high initial *O* and moisture content, loses relatively more *O* compared to *e.g.*, coal, increasing the calorific value of the resulting product [170].

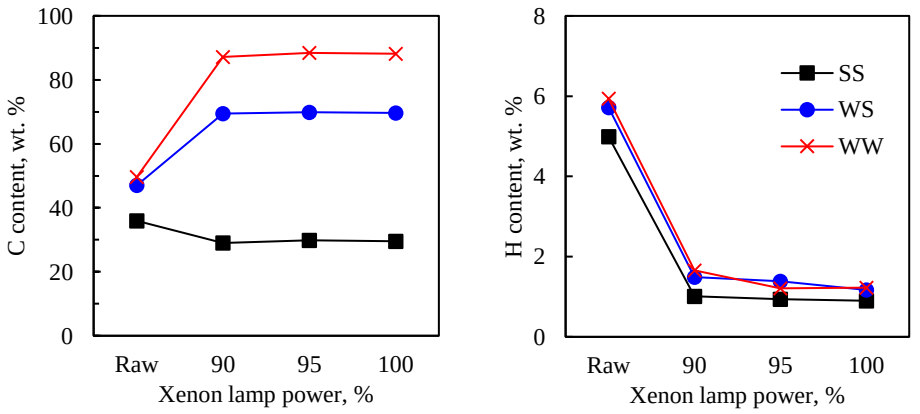

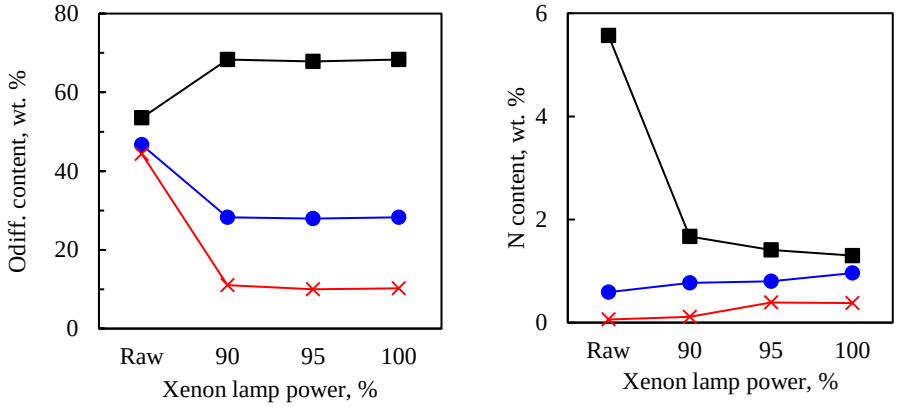

Fig. 6.42. Impact of xenon lamp power on C, H, N, O content of feedstock and char.

The influence of solar pyrolysis on feedstock HHV shows a significant increase of calorific values in lignocellulosic samples, with exact values listed in Table 27. The highest HHV is found for WW chars with an average of 27.09 MJ/kg, calculated based on *Jenkins* formula, presented previously in Eq. (1.5). WS chars HHV has an average of 22.72 MJ/kg, while SS chars show lower HHV than raw feedstock with an average of 12.96 MJ/kg compared to 16.10 MJ/kg for raw SS. By considering the significant HHV increase of feedstock compared to raw samples, *van Krevelen's* diagram (Fig. 6.43) was constructed with *H*/*C* and *O*/*C* atomic ratios calculated based on the elemental composition of raw feedstock (Table 3) and obtained bio-chars (Table 27), respectively. Impact of the pyrolysis conditions on the solid product HHV is presented in Fig. 6.44. As solar pyrolysis dramatically increase, the lignocellulosic samples move into higher carbonization zones, while SS due to very high *O* content and low *C* content compared to raw samples, chars move into the opposite direction. After solar pyrolysis, *H*/*C* ratios of WW and WS reduce from 1.427 and 1.450 to average 0.185 and 0.231, respectively. Atomic *O*/*C* ratios follow a pattern and reduced from 0.672 and 0.745 to an average of 0.089 and 0.303 for WW and WS, respectively. For SS samples, *H*/*C* ratios with an initial 1.655 reduces to an average of 0.385, however, *O*/*C* ratios increase from 1.118 to 1.739. This can be explained by migration of elemental *C* from the char with a simultaneous relative increase of elemental *O* in SS bio-chars. However, obtained bio-chars of WW samples display very high carbonization level, with *H*/*C* and *O*/*C* ratios corresponding to the anthracite atomic ratios range.

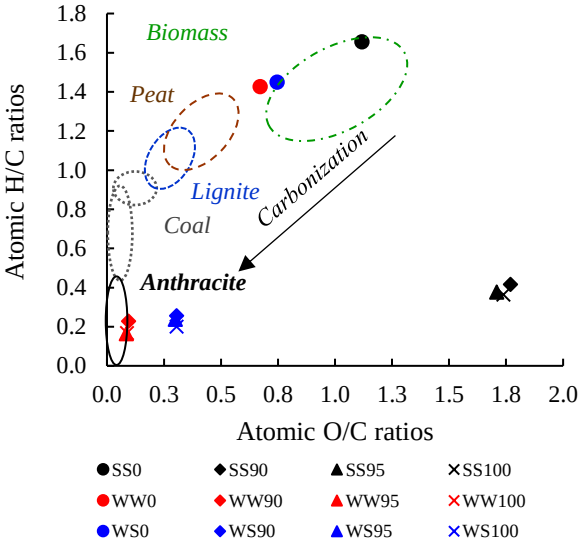

Fig. 6.43. Van Krevelen's diagram for raw biomass samples and obtained bio-chars.

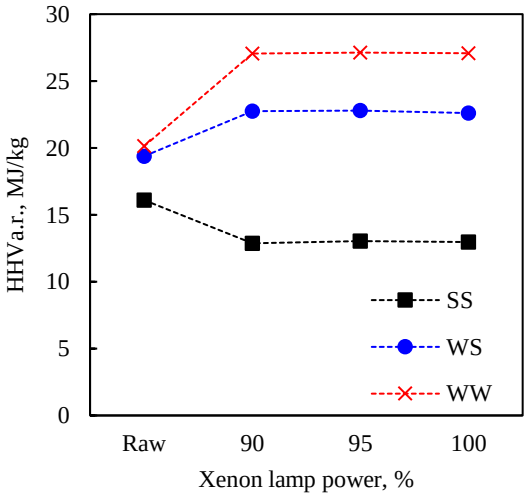

Fig. 6.44. Impact of the heating rate on char HHV.

6.6.4. Dry pyrolysis gas

Fig. 6.45 shows the final shares of gaseous compounds forming dry pyrolysis gas. Gas shares were calculated based on numerical integration (rectangle method) of the recorded formation profiles over time, where the final yield was proportional to the volumetric area of the specific gas components, related to the total sum of each compound area. The volumes of gases were quantified from the volumetric percentage of gas components, with exclusion of the inert gas N_2, focusing at the species released from the biomass only. Then, the molar quantities and masses of each gas component were calculated based on the ideal gas law as proposed by Zeng et al. [35]. H_2 is the most dominant component in the pyrolysis gas, which is rather unusual for slow pyrolysis according to the literature [2]. The very high volumetric content of H_2 stems from the selected experimental method, with emphasis on the release of a maximum amount of dry gas during the experiment. Since H_2 is the last species to be recorded, its release occurs at a very slow rate and high temperatures, hence, its formation occurs over a prolonged time period resulting in the highest yields after the integration of analyzers indications over the experiment time. H_2 yields in pyrolysis gas are 47.58 vol.%, 51.33 vol.%, and 52.77 vol.% for WW; 48.31 vol.%, 47.53 vol.%, and 49.30 vol.% for WS; and 57.15 wt.%, 54.75 wt.%, and 54.61 wt.% for SS, for increasing heating rates, respectively. The second most abundant gas in the final share is CO_2 with detected yields of 23.57 vol.%, 20.17 vol.%, and 19.63 vol.% for WW; 27.29 vol.%, 28.46 vol.%, and 27.60 vol.% for WS; and 22.65 vol.%, 21.33 vol.%, and 21.31 vol.% for SS, respectively. The intense formation of CO_2 is due to the oxidation reactions in the first stages of decomposition, unavoidable given the high oxygen content of the biomass. CO shares for WW and WS comparable across the experiments with average yields of 16.17 vol.% and 14.64 vol.%, respectively, whereas SS content in the final gas varies from 11.86 vol.% for the lowest heating rate to 16.01 vol.% and 16.42 vol.% for 4.5 and 5.3 K/min, respectively. CH_4 content is highest for WW pyrolysis, with similar yields denoted across the experiment with an average of 10.55 vol.% and 8.04 vol.% for WS, and 5.83 vol.% for SS. Hence, due to low formation intensity and rate of CH_4, low concentrations exhibit considerable uncertainty in the final yield, ±1.59-2.39 vol.%. The released oxygen during pyrolysis experiments did not exceed 2.3 vol.% of the total composition. The exact values of the final gas components shares with uncertainties are presented in Table 27.

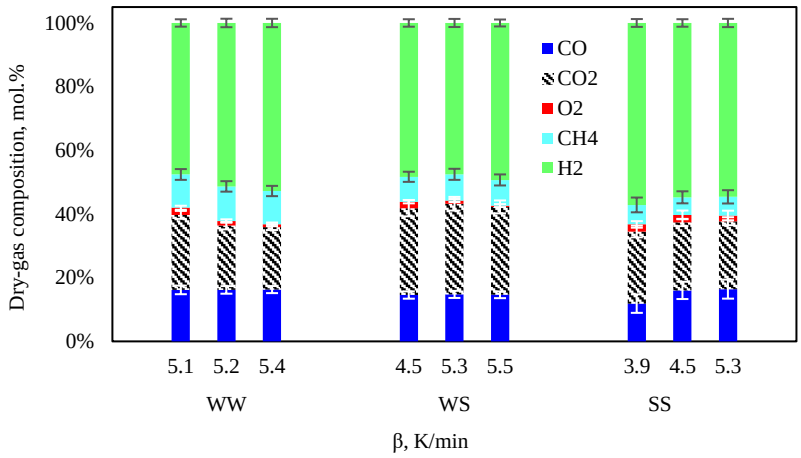

Fig. 6.45. Components shares in the final pyrolysis gaseous product.

Table 27: Final results of the solar pyrolysis study with denoted product shares and characterization.

Process conditions		Product yields, wt.%				Char and bio-oil properties						Pyrolysis gas properties											
Sample	Heating rate	Char	Bio-oil	Pyrolytic gas		*N*, wt.%	*C*, wt.%	*H*, wt.%	*O*, wt.%	BET, m^2/g	HHV, MJ/kg	CO, vol.%		CO_2, vol.%		O_2, vol.%		CH_4, vol.%		H_2, vol.%		HHV, MJ/kg	EUF, %
WW0	Raw					0.06	49.61	5.94	44.39	0.21	20.13												
WW90	4.5 K/min	21.91	68.36	9.74	±0.67	0.11	87.21	1.66	11.02	6.97	27.06	16.16	±1.35	23.57	±1.25	2.24	±0.64	10.46	±1.69	47.58	±1.16	13.94	+10.88
WW95	5.0 K/min	21.66	69.14	9.20	±0.65	0.39	88.42	1.21	9.98	145.09	27.13	16.16	±1.19	20.17	±1.17	1.47	±0.53	10.87	±1.65	51.33	±1.33	16.08	+12.08
WW100	5.5 K/min	21.21	70.20	8.59	±0.54	0.38	88.17	1.23	10.22	43.06	27.08	16.27	±1.11	19.63	±0.93	0.88	±0.55	10.46	±1.62	52.77	±1.31	16.56	+12.29
WW	Bio-oil					0.00	55.55	6.92	37.53	-	21.99												
WS0	Raw					0.59	47.02	5.72	46.67	0.52	19.38												
WS90	4.5 K/min	27.45	63.78	8.77	±0.83	0.77	69.5	1.49	28.24	1.09	22.75	14.55	±1.15	27.29	±2.57	2.01	±0.50	7.84	±1.59	48.31	±1.17	12.16	-8.45
WS95	5.0 K/min	26.66	61.69	11.65	±0.96	0.8	69.88	1.39	27.93	1.67	22.79	14.76	±1.11	28.46	±2.15	1.01	±0.47	8.23	±1.74	47.53	±1.28	12.06	-9.34
WS100	5.5 K/min	27.08	61.43	11.48	±0.92	0.96	69.62	1.17	28.25	2.10	22.61	14.63	±1.06	27.60	±2.03	0.41	±0.47	8.06	±1.73	49.30	±1.08	12.61	-9.08
WS	Bio-oil					5.24	36.41	5.26	53.09	-	16.36												
SS0	Raw					5.57	35.93	4.99	53.51	0.55	16.10												
SS90	4.5 K/min	39.54	49.96	10.50	±1.37	1.67	29.00	1.01	68.32	37.69	12.87	11.86	±2.90	22.65	±1.85	2.22	±1.03	6.12	±2.32	57.15	±1.23	14.43	-19.16
SS95	5.0 K/min	38.53	52.32	9.15	±0.88	1.41	29.8	0.94	67.85	40.84	13.04	16.01	±2.72	21.33	±1.14	2.39	±1.37	5.52	±1.89	54.75	±1.18	13.98	-19.14
SS100	5.5 K/min	38.29	52.77	8.94	±0.97	1.30	29.50	0.90	68.30	42.94	12.96	16.42	±3.00	21.31	±1.25	1.81	±1.51	5.85	±2.09	54.61	±1.30	14.21	-19.22
SS	Bio-oil					2.37	13.38	9.05	75.19	-	12.83												

6.6.5. Bio-oil and energy upgrade factor

Comparison of the elemental composition (wt.%) of the bio-oil averaged samples obtained from WW, WS, and SS solar pyrolysis is presented in Fig. 6.46. Denoted bio-oil from WW solar pyrolysis can be considered as a quality product, with zero elemental *N*, 55.55 wt.% of *C*, 6.92 wt.% of *H*, and lowest *O* content amongst investigated samples (37.53 wt.%) with estimated HHV of 21.99 MJ/kg compared to other studies on wood pyrolysis bio-oil quality [166]. WS pyrolysis bio-oil contains less elemental *C* 36.41 wt.%, and *H* 5.26 wt.%, in favor of higher *O* content 53.09 wt.%, with the highest share of elemental *N* 5.24 wt.%, giving a final estimated HHV of 16.36 MJ/kg. The lowest quality bio-oil is observed for the solar pyrolysis of SS samples, with a major share of *O* 75.19 wt.%, which is probably due to the highest share of oxygenated compounds in final bio-oil composition, and content significantly exceeding reported values [171].

Based on estimated HHV values of solar pyrolysis products and determined product yields, the Energy Upgrade Factor (EUF) was calculated according to Eq. (9.6) and presented in Table 28. For this study, the solar pyrolysis process of WW feedstock provides 10.88-12.29 % of primal chemical energy of the feedstock upgrade, while WS and WW EUF value is negative, corresponding to loss of the primal chemical energy during solar pyrolysis.

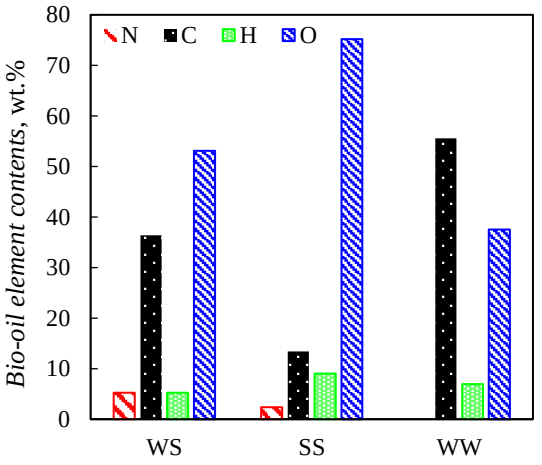

Fig. 6.46. Weight percentages of C, H, N, O of averaged bio-oil samples.

6.6.6. Correlation of the gaseous products formation to model-free kinetic predictions

The evolution of gaseous compounds recorded during pyrolysis is presented in Figs. 6.48-6.50 for WW, WS, and SS. The impact of the heating rate on gaseous compound formation is very low. The significant novelty of the study is the comparison of model-free (MF) kinetic predictions and the conversion rate profiles calculated for the observed heating rates based on isoconversional parameters determined for the same feedstock during dynamic TGA runs that were previously studied [163]. As E_α profiles used for MF predictions calculation in this study were validated in previous studies that were compared to the experimental TGA data, the values of predicted $d\alpha/d\tau$ are accurate. Low heating rates and high-intensity sampling of the gas analyzers allow the generation of high-quality profiles of gaseous compound formations as a function of time, which is later correlated to the actual temperature of the feedstock. Significant similarities between MF predicted conversion rates and gas formation profiles can be observed, however, exact quantification of the correlation is problematic, and will be a subject of a detailed future study. The information encrypted in E_α, presented and validated previously gives greater insight into probable $d\alpha/d\tau$ profiles of the reacting feedstock at investigated heating rates. Predicted conversion profiles in Figs. 6.48-6.50 for WW, WS, and SS first reflect the peak of moisture evaporation at initial heat supply. Next, the most visible correlation can be observed between the main predicted devolatilization peaks, which are represented by CO_2 and CO formation during solar pyrolysis experiments, as well as monitoring the overlapping conversion profile shoulders. Predicted conversion profiles of WW (Fig. 6.48) and WS (Fig. 6.49) found little reflection in CH_4 and H_2 formation because, as they are related to minimal mass loss of the samples at high temperatures of the charring pyrolysis regime [42]. Predicted conversion rate profiles of SS (Fig. 6.50) determined the best resemblance in evolving CO_2, at the same temperature range as main mass loss denoted during TGA measurements of the same sample [43]. Contrary to lignocellulosic biomass, SS predicted pyrolysis conversion rate profiles at temperatures above 500 °C exhibit overlapping peaks and shoulders that allow monitoring by H_2, CH_4, and CO formation, resulting from secondary and tertiary reaction occurring in the complex structures of the sludge.

Continuing the discussion of gas evolution profiles, the first gas released is CO_2, with first concentrations denoted at 200 °C, followed by very low, however concerning, O_2 concentration <0.8 vol.%. To the best of our knowledge, no study has reported oxygen release during biomass pyrolysis so far. After careful measurement error analysis including installation tightness test and consultation with gas analyzer specialists, followed by exclusion of any overlapping spectra, and finally oxygen measuring cell replacement in ABB AO2020 analyzer, certain conclusions can be highlighted for future attention. High elemental oxygen content in the raw biomass *i.e.*, 44.37, 46.59, and 51.49 wt.% for WW,

WS, and SS, respectively, despite lack of external oxygen, minor amounts of O_2 detected during solar pyrolysis experiments, consistently for each experimental run. Numerous reactions were identified and presented for biomass gasification by B. Wojnicka et al. [30] and pyrolysis by Z. Kaczor et. al [100] and H. Weldekidan [172], however, none of which lead to pure O_2 formation. Adressing the O_2 formation issue even more, Fig. 6.47 was formed, comparing the feedstock heating profiles with the heating rate of the reactor recorded during the same experiments. As temperature and heating rate profiles are in good agreement with each other across the investigated lamp power range, only results for the highest variable are presented and discussed. First, at temperatures below 150 °C feedstock heating is slower than the reactor, obviously due to moisture evaporation. Interestingly, the feedstock heating profiles exceed the reactor heating rates, indicating exothermic behavior of the investigated feedstock during pyrolysis. Despite the absences of oxidizer supplied externally to the reactor system, the high oxygen content within the biomass acts as an oxidant boosting the decomposition intensity with increasing feedstock heating rates, which possibly favors auto-gasification reactions at early decomposition stages. For WW pyrolysis, O_2 is released randomly between 250 and 400 °C with CO_2 and CO. In the case of WS pyrolysis, each experimental run O_2 release correlates with CO formation. During SS pyrolysis, O_2 is formed in conjunction with other gaseous components once temperature reaches 340 °C. After reaching 500 °C, the heating rate profiles of the feedstock converge with the reactor heating profiles until the end of the experiments, where more passive reactions occur *i.e.*, charring, leading mainly to CH_4 and H_2 formation.

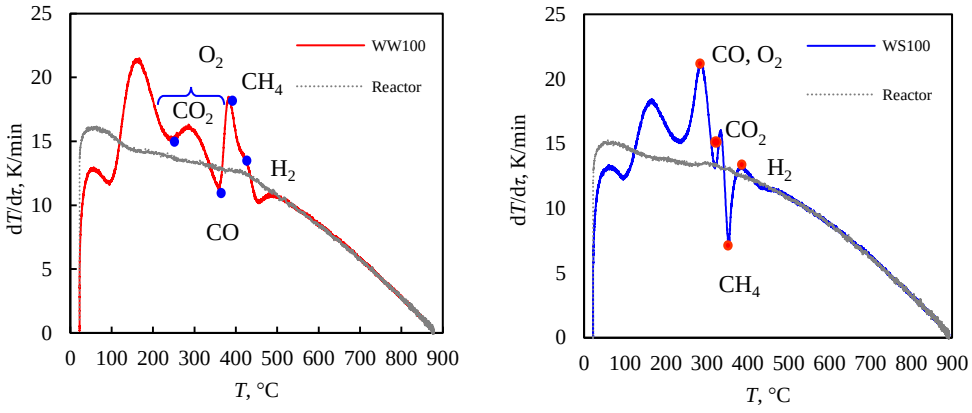

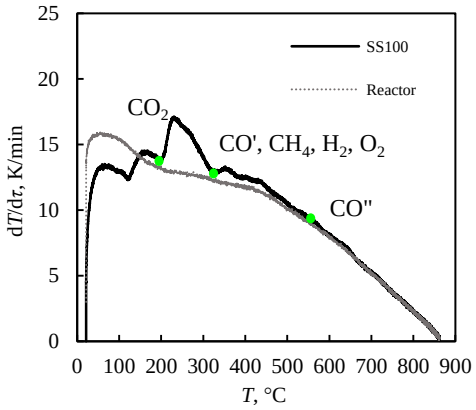

Fig. 6.47. Comparison of heating rates of the reacting feedstock with indicated gas formation temperatures, and reactor during experiments with 100% lamp power.

Regarding specific dry-gas formation for each feedstock type, staring from the WW samples (Fig. 6.48), the first detected gas component is CO_2 released at 220-250 °C, while indications of CO, CH_4, and H_2 start at the narrow temperature window of ~300-360 °C, which follows the primary pyrolysis rate law presented in, however, the specific evolution profiles differ from each other [63]. During WW pyrolysis CO_2 formed a steep and sharp, symmetric peak, which represents the high reaction rate of the pyrolysis step, and may reflect the pyrolysis of cellulose [173]. CO peak followed CO_2 profile at first and then significantly slows down at 450 °C, where the first peaks of CH_4 and H_2 appeared. Further heating amplified significantly H_2 formation that was the most dominant species at final temperatures, where CH_4 release correlated with CO formation and has ended at ~750 °C. The overlapping character of CO, CH_4, and H_2 formation profiles can correspond to additional decomposition reaction occurrence that release the same products. Yang et al. [165] studied pyrolysis characteristics of pure cellulose, hemicellulose, and lignin with TGA, and found that hemicelluloses consisting of various saccharides *e.g.*, mannose, xylose, galactose, glucose, decomposes first at 260-300 °C. Due to cellulose's polymeric structure it shows a very quick and intense decomposition of long D-glucose chains (n>200) chains generating levoglucosan via cleavage of β-1,4-glycosidic bonds upon reaching 300-400 °C. Lignin slowly reacts throughout the reaction process with a slight increase in intensity at 200-400 °C. Generally, CO_2 and CO release is associated with pyrolysis of cellulose and hemicellulose, especially from cracking of carbonyl (C-O-C) and carboxyl (C=O) groups [155,165], whose decomposition also yields the majority of bio-oil compounds compared to lignin [165], whereas CH_4 and H_2 are mainly formed from lignin. The release of CH_4 is mainly due to cracking of methoxy groups (-O-CH_3) at temperature below 600 °C. According to the literature, lignocelluloses releases CH_4 during primary and

secondary pyrolysis at temperatures vary from 200-600 °C, however, lignin dominates because of high -O-CH_3 content [174]. H_2 reaches highest concentration later than CH_4 above 700 °C, which is also consistent with the literature [35,174]. This can be explained by H_2 not only being produced via decomposition of biopolymers but also release from cracking and deformation of aromatic C-H and C=C bonds, where amorphous lignin possesses the highest content [175]. Temperature plays a significant role in H_2 formation owing to high carbon-hydrogen bond stability that are more prone to cleavage at high temperatures [176].

Gaseous species evolution during WS pyrolysis are presented in Fig. 6.49, where the evolving profiles display similar tendencies compared to the obtained WW profiles. The major differences include symmetrical formation trends of CH_4 and H_2 without overlapping peaks, which were observed during the solar pyrolysis of WW. CO and CO_2 formation were very similar, both supported by a slight shoulder that shifts towards higher temperatures. The lack of the first peak of CH_4 and H_2 formation in WS pyrolysis that was clearly visible during WW experiments at 470 °C, what could be partially assigned to much lower lignin content 6.0 wt.% in WS samples compared to 27.9 wt.% in WW samples.

Finally, Fig. 6.50 shows gas compounds evolution during SS solar pyrolysis, resulting in very irregular gas formation profiles. Contrary to WW and WS samples, SS as a feedstock contained very little lignocelluloses and leaving the majority of the components to lipids, proteins, organic wastes, and inorganic ash [26,121,177]. The thermal decomposition began at 200 °C with the intense release of CO_2 and simultaneous low-intensity O_2 formation. At temperatures of 300-330 °C, corresponding to O_2 release, the intense release of H_2 and CH_4 begins with a simultaneous slow release of CO. CO_2 release continued throughout the majority of the process until 750 °C, what could be somehow associated with bond cleavage of carboxyl groups (-O-C=O) present in the fatty acids [178]. By comparing SS gas evolution to WS and WW, it is revealed that CO generation is separated from CO_2 formation. In the case of lignocellulosic biomass origin of CO it is related to the pyrolysis of cellulose and hemicellulose, in which low content in SS can influence low-intensity release at temperatures 300-550 °C. Another probable CO origin in SS pyrolysis is *Boudouard* reaction, which is the redox reaction of an equilibrium mixture of CO_2 and char, $CO_{2(g)}+C_{(s)} \rightleftharpoons CO_{(g)}$, highly endothermic, usually occurring at temperatures ~700 °C [179]. The intense release of H_2 and following CH_4 can be again justified through rearrangement of the carbon structures in char, occurring at high temperatures.

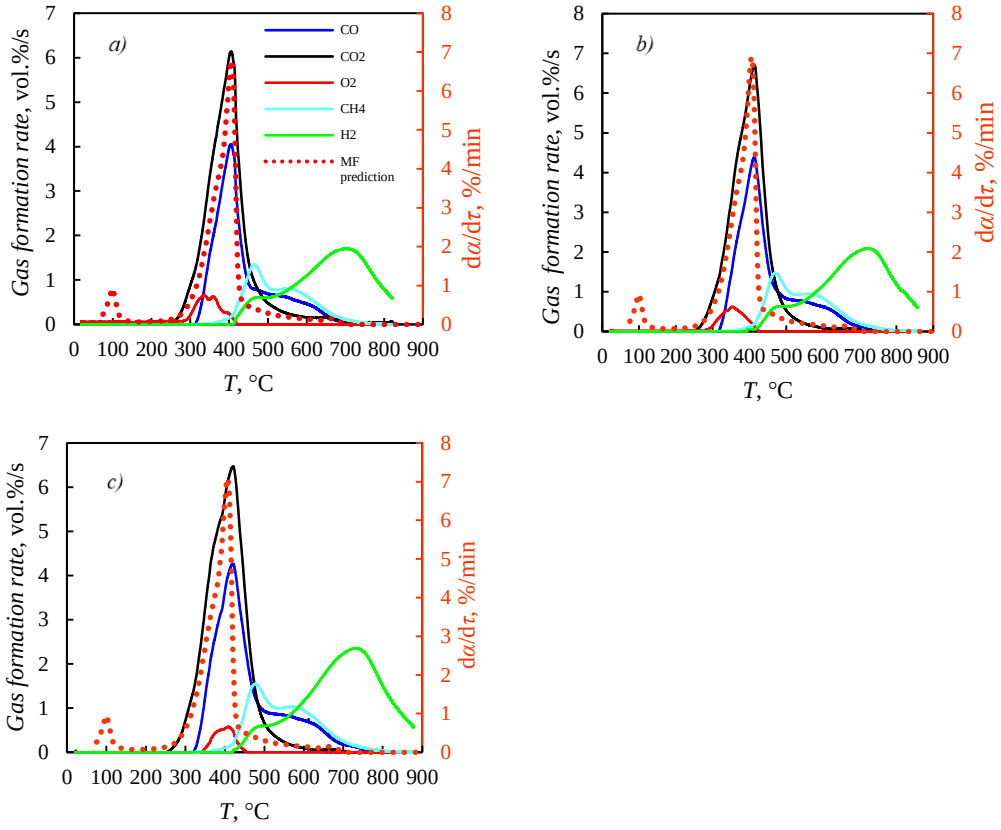

Fig. 6.48. Gaseous species evolution profiles during WW solar pyrolysis compared to *predicted WW conversion rate profiles for the a) 5.1 K/min, b) 5.2 K/min and c) 5.4 K/min.*

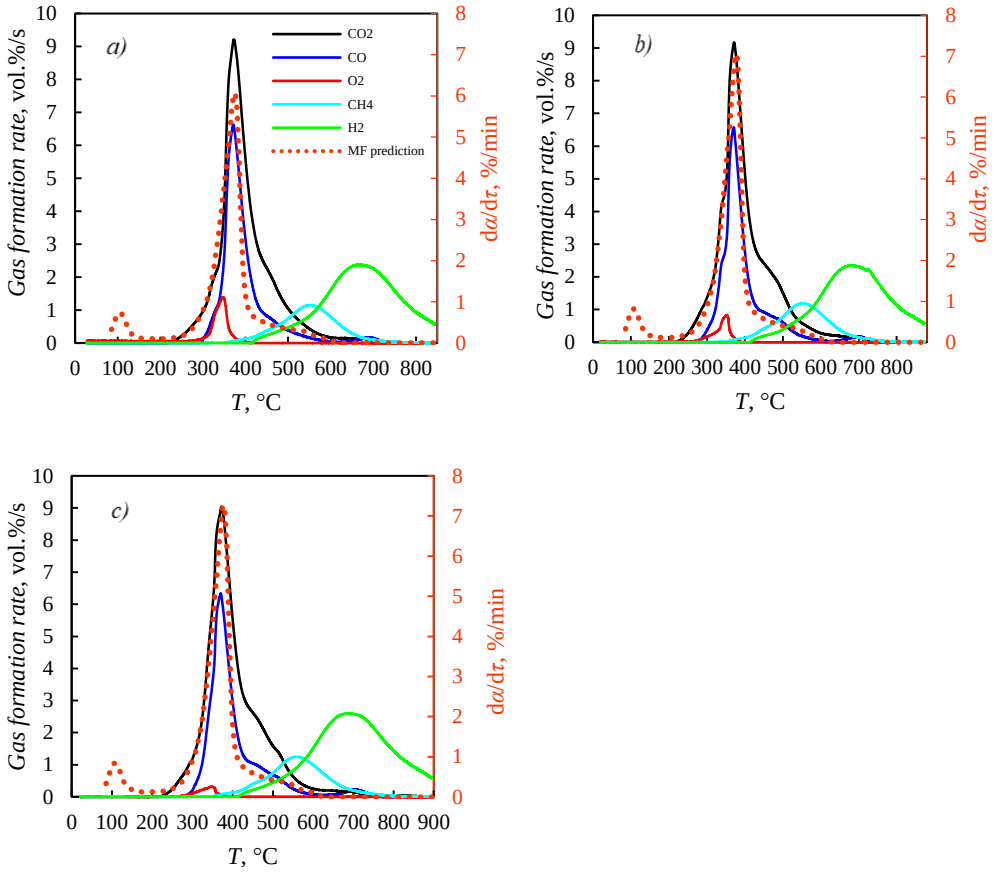

Fig. 6.49. Gaseous species evolution profiles during WS solar pyrolysis compared to predicted WS conversion rate profiles for the a) 4.5 K/min, b) 5.3 K/min and c) 5.5 K/min.

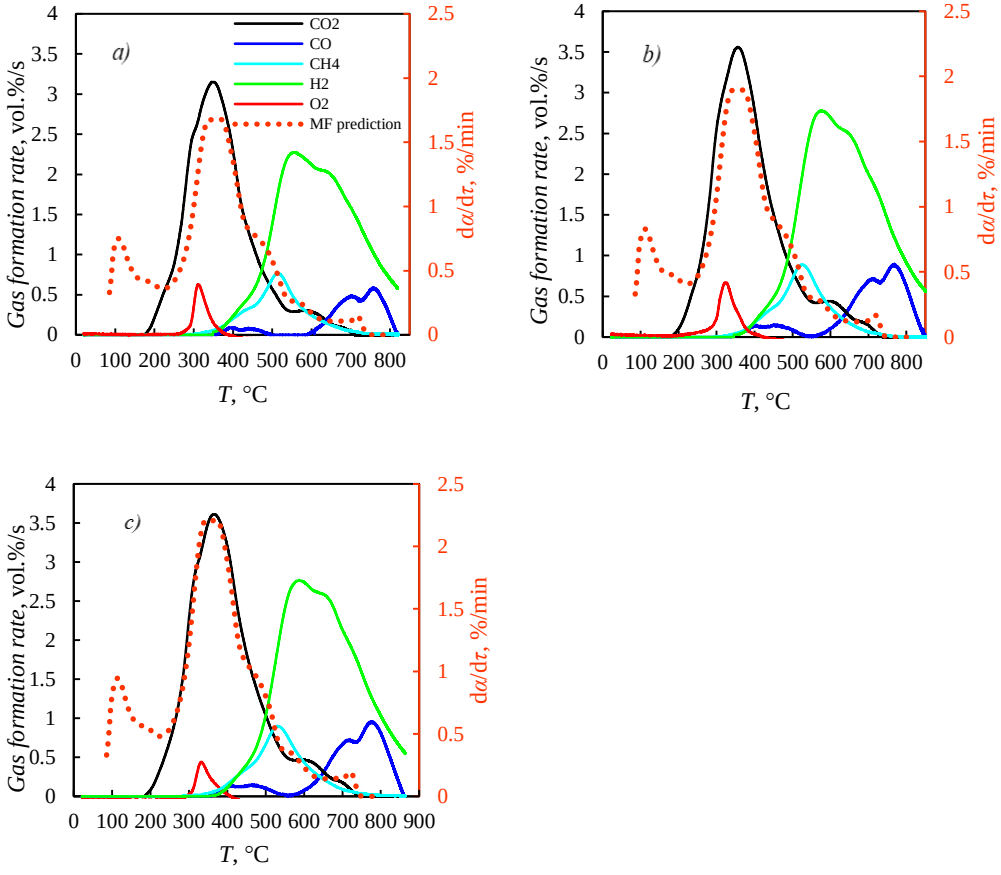

Fig. 6.50. Gaseous species evolution profiles during SS solar pyrolysis compared to predicted SS conversion rate profiles for the a) 3.9 K/min, b) 4.5 K/min and c) 5.3 K/min.

Summary

As a first part of thesis research, the design of the bench-scale solar pyrolysis reactor is presented and discussed. A review of the pyrolysis process fundamentals and existing solar pyrolysis reactors has been presented. Thermal processes with complex characters and mechanisms, such as pyrolysis, provide a field for further complex experimental investigation. The design idea comprised latest literature review findings, focusing on indirect heating of the feedstock. In order to power the solar-driven biomass pyrolysis, based on the review of artificial light sources for solar-thermal biomass conversion applications, the 1.6 kW xenon-arc lamp was chosen as the radiation source for the study.

Simultaneously to experimental work in the laboratory, the thermoanalytical measurements of the pyrolysis decomposition behavior of the investigated feed was studied on the TGA. Three waste biomass samples pyrolysis was investigated at the heating rates 5-40 K/min at temperature range of 25-700 °C. Single experiment was carried out for 5 mg of a milled, non-sieved, sample in alumina crucibles, while the pyrolysis atmosphere was provided by the 50 ml/min nitrogen flow. Feedstock presented well-corresponding pyrolysis behavior according to the other results presented in the literature. All of the obtained mass-loss profiles were in good agreement with each other in terms of peak temperatures and overall mass-loss, proving analysis quality, and making further kinetic calculations viable.

Model-free, isoconversional Friedman method proved to be a powerful tool for kinetic analysis of waste biomass pyrolysis, providing apparent kinetic parameters and quality fit to experimental data. Two approaches were analyzed analyzing WW decomposition, 3-PC model, and pyrolysis gas compounds formation in E-MP model. Gas analyzer indications provided vital information for the kinetic model establishment, which resulted in a good fit for experimental data and kinetic predictions. The generalized master-plot method proved that pyrolysis of waste wood obeyed diffusion mechanism with a transition to phase boundary models. Contribution factors of main mass balance equation for the E-MP model addressed shares of gaseous products especially well during charring. Charring period, described by two consecutive steps in the E-MP model proved that char formation is associated with high activation energy reactions 249.71 and 162.01 kJ/mol for methane and hydrogen formation respectively, yet with a low contribution, so overall thermal effect of those reactions on total decomposition process was low. 3-PC model described charring as a single step with lower activation energy 96.49 kJ/mol, high reaction order, and contribution, as average lignin decomposition reaction. The approach of the E-MP model originated from an invert modeling idea, engineering perspective, where

pyrolysis kinetic studies should aim for process industrialization, setting the need for product formations identification for different types of feedstock, in order to allow maximization of desirable compounds yields. Approach of 3-PC model is already well described in the literature, over the years identified thermal regimes of biomass compounds degradation, cellulose, hemicellulose, and lignin, which is useful in the case of biomass efficient utilization, without consideration of pyrolysis products, or gaining knowledge on wildfire spread and behavior. It is plausible, that experimentally based models, established inversely based on the identification of pyrolysis products forming reactions, are valuable for future process optimization and commercialization, especially using renewable solar energy, if only the reactions and corresponding reaction models can be identified explicitly.

Regarding SS pyrolysis kinetics, isoconversional analysis yielded initial parameters for establishing a complex kinetic model consisting of 10 elementary reactions. Linkage of isoconversional and model-based kinetic methods have been presented and discussed. Regarding the literature review, the proposed model describes sewage sludge holistic pyrolysis, without temperature zones separations. Both isoconversional and model-based kinetics shown a tendency for activation energy increase with conversion progress, which is typical for the process with deaccelerating kinetic character. A similar conclusion can be drawn from the master-plot method, resulting in fitting to order-based reaction models. Friedman method proved to be a fast and effective method (R^2=0.9999) of apparent kinetic parameters estimation, with isoconversional activation energies and pre-exponential factors E_α (31.4-244.9) kJ/mol and A_α (1.17-14.4) log(1/s) respectively. Investigated sewage sludge presented deaccelerating character during pyrolysis, which was confirmed by fitting to n^{th} order reaction models and high slope of Friedman isoconversion lines. The kinetic model was established on plateau regimes of isoconversional parameters, perceived as actual elementary reaction step. 10 isoconversional "steps" were transduced into kinetic computations resulting in 10 independent nth order reaction model and optimized using the least square method for objective $R^2 \rightarrow$max. Stolarek and Ledakowicz's thesis was proved, that high order reaction models in single-step kinetic modelling are in fact a product of a set of low reaction orders of elementary steps.

WS pyrolysis kinetics were described using numerical deconvolution method, based on available peakfit.m Matlab function block. The three-step Gaussian algorithm resulted in three elementary conversion profiles, which sum evaluated the experimental decomposition profile with R^2=0.99906. The decrypted kinetic parameters of the elementary pyrolysis steps, correlated again to the independent decomposition of the cellulose, hemicellulose and lignin. Exact values of the Arrhenius parameters, *E*, *A*, and *n*, were: 142.0±6.3 kJ/mol, $6.86 \cdot 10^{14} \pm 5.81 \cdot 10^{14}$ min^{-1}, 1.52±0.06 for hemicellulose, 227.1±23.1 kJ/mol, $5.02 \cdot 10^{22} \pm 44.81 \cdot 10^{22}$ min^{-1}, 1.23±0.01 for cellulose, 25.3±1.9 kJ/mol, $8.02 \cdot 10^{2} \pm 6.27 \cdot 10^{2}$ min^{-1} 0.98±0.05 for lignin.

Apart from traditional model-based kinetics, an original approach to model-free modeling of the waste biomass pyrolysis has been successfully presented. Friedman isoconversional method provided apparent activation energies as a root for kinetic calculations with the values carrying across the conversion: 48.1-294.3 kJ/mol for WS,

21.0-361.9 kJ/mol for WW and 58.1-484.3 kJ/mol for SS. Isoconversional pre-exponential factors were determined using linear compensation effect and were $7.2 \cdot 106$-$1.8 \cdot 10^{21}$ 1/min, $1.6 \cdot 1^{4}$-$1.2 \cdot 10^{25}$ 1/min, and $1.5 \cdot 10^{9}$-$3.2 \cdot 10^{30}$ min^{-1} for WS, WW, and SS respectively, with corresponding R^2 equal to 0.9912, 0.9876, and 0.9406. The proposed method can be applied to any feedstock type not only for pyrolysis, yet for any thermal decomposition process that can be experimentally evaluated in TGA.

Last but not least, the final results of the solar pyrolysis experimental campaign are presented. The experimental methodology, including measurement techniques, sample preparation, and experimental setup are presented. Xenon-arc lamp provided plenty of radiant power to carry out the solar pyrolysis process, with final temperatures exceeding 900 °C. WAGO PFC100 PLC proved to be effective data acquisition system for the 18 measured variables, however, simultaneous visualization of the recoded values caused software stability problems, due to limited RAM capacity of the device. Nonetheless, the PLC-based measurement methodology allowed to record 18 measured variables with 1 s data resolution for 90 min duration of the single experiment. For the future studies regarding indirect heating-based solar pyrolysis, copper implementation should be reconsidered, due to relatively low melting-point comparing to other materials with sufficient conductivity, *e.g.*, stainless steel. Feedstock temperature measurement, using a set of 0.5 mm K-type thermocouples packed with copper net, did not cause any major problems, and is highly advised as a method for reacting feedstock temperature measurement for the future. Thanks to the over-sized bio-oil condenser, no bio-oil contamination was denoted within the NDIR analyzer cells. Regarding obtained products and their final shares, the study well responded for the shortage of basic research within the slow solar pyrolysis field. Original approach to the actual heating rates of the reacting feedstock are proposed and discussed. The final heating rate value, on which the very process classification is based on, is highly fragile to the assumed calculation method. Within this study, final average heating rate did not exceeded 6 K/min, while actual, momentary values gave a novel insight into thermal behavior the pyrolysis process.

Conclusion

1. Hydrogen-rich pyrolysis gas was obtained during the solar pyrolysis processing of each feedstock with HHV varying from 27.34 MJ/m^3 for the WS to 30.35 MJ/m^3, what may have been influenced by significant amounts of heavy metals and act as potential catalysts in the ash samples. Negligible amounts of free oxygen were released during the most dynamic pyrolysis part, arguably due to elemental oxygen reactions with possible smaller impact of catalytic thermal degradation of oxides present within the biomass. Despite high calorific value of the gas, the final shares of the gaseous fraction in products were low, not exceeding 12 wt.%.
2. Solar pyrolysis proved to be not only a method for highly-porous and highly-calorific biochar production from waste biomass, yet a promising way to generate hydrogen-rich pyrolysis gas, even at moderate heating conditions. Obtained chars, especially after solar pyrolysis of lignocellulosic biomass, showed HHV of 27.09 MJ/kg and 22.02 MJ/kg for WW and WS, respectively, which has significant potential for renewable solid fuel. Porosity measurements of the solar pyrolysis chars indicated that process temperature should not exceed ash-fusion temperatures. Exceeding specified temperatures during the process and cause significant loss of BET area. An increase of lamp power and long process time caused degradation of porous structures within the biomass. The highest BET area was denoted for WW samples at 5.0 K/min with 145.09 m^2/g.
3. Each studied feedstock is promising method for solar upgraded bio-oil, with average yields of 69.23 wt.%, 62.3 wt.%, and 51.68 wt.% for WW, WS, and SS, respectively. Bio-oil composition varied for different feedstock types, with major content of elemental oxygen. The highest quality bio-oil was obtained from WW pyrolysis with the lowest oxygen to carbon fraction and HHV of 21.99 MJ/kg. Further studies should focus on the possibility of bioactive compounds extraction from solar liquid fuels.
4. The average solar pyrolysis product yields (bio-oil, gas, char) were 51.68, 9.53, and 38.79 wt.% for SS, 69.23, 9.18, and 21.59 wt.% for WW, 62.30, 10.64, and 27.06 wt.% for WS. Investigated slow solar-pyrolysis resulted in liquid-rich product yields, with dry-gas shares less than 10 wt.%. The SS char yields and char's SEM photos resembles to the feedstock ash content and ash mineral structures.
5. During the laboratory experiments, possible exothermic behavior of the waste biomass decomposition was observed, interpreted as internal heat generation within feedstock pellets, resulting in the overtake of the reacting biomass heating

profiles over the reactor heating profiles. Exothermic reaction could have been favored by the high elemental oxygen content of the feed, resulting in partial-oxidation reactions leading to intense formation of the CO_2, and low amounts of the free O_2. The high elemental oxygen content was observed in the bio-oil and dry pyrolysis gas, however, the final quantities meet the elemental balance concerning elemental composition of the feed and the study assumptions.

6. The 1.6 kW xenon lamp power controlled within 90-100% range provided specific average heating rates of 4.51, 5.32, and 5.49 K/min for WS; 5.10, 5.19, and 5.37 K/min for WW; and 3.95, 4.48, and 5.25 K/min for SS, respectively. Temperature measurement inside the reacting particle proved the complexity of the pyrolysis process, with exothermal character, and significantly higher reactivity of the lignocellulosic biomass compared to SS.
7. For this study, the solar pyrolysis process energy upgrade factor EUF was determined. Amongst the investigated feedstock, and for the specified experimental conditions, only WW feedstock provides 10.88-12.29 % of primal chemical energy of the feedstock upgrade, while for the WS and WW processing EUF value is negative, corresponding to loss of the primal chemical energy during solar pyrolysis.
8. Generalized master-plot methods gave insight into the probable reaction model functions governing the pyrolysis decomposition of the investigated feedstock during the kinetic analysis. It was confirmed that lignocellulosic biomass generally obeys deaccelerating kinetics with corresponding reaction models of the diffusion and contracting geometry. Stolarek's and Ledakowicz's hypothesis that high reaction orders in single-step kinetics are in fact a product of lumped approach to a system of a set of elementary reactions was proved for the SS pyrolysis, resulted in 10 independent, order based models steps, with reaction orders lower than 3.0.
9. Possible correlation between model-free dynamic predictions and gaseous species evolution was found, highlighting the value of apparent activation energy profiles in describing the actual solar pyrolysis process in laboratory reactor. Predicted conversion profiles, based on isoconversional kinetic parameters extrapolated to the heating rates and temperatures denoted during laboratory experiments reflected dry-pyrolysis gas formation profiles.

Literature

[1] R. Adib REN, M. Folkecenter, A. Development Bank, M. Eckhart Mohamed El-Ashry David Hales Kirsty Hamilton Peter Rae, F. Bariloche, Renewables 2018 · Global Status Report, 2018. doi:978-3-9818911-3-3.

[2] K. Zeng, D. Gauthier, J. Soria, G. Mazza, G. Flamant, Solar pyrolysis of carbonaceous feedstocks: A review, Solar Energy. 156 (2017) 73–92. doi:10.1016/j.solener.2017.05.033.

[3] R. Quadrelli, S. Peterson, The energy-climate challenge: Recent trends in CO2emissions from fuel combustion, Energy Policy. 35 (2007) 5938–5952. doi:10.1016/j.enpol.2007.07.001.

[4] European Commision, The European Green Deal, Brussels, 11.12.2019 COM(2019) 640 final., 2019.

[5] Q. Bach, K. Tran, Ø. Skreiberg, Combustion kinetics of wet-torrefied forest residues using the distributed activation energy model (DAEM), Applied Energy. 185 (2017) 1059–1066. doi:10.1016/j.apenergy.2016.02.056.

[6] S.A. El-Sayed, M.E. Mostafa, Pyrolysis characteristics and kinetic parameters determination of biomass fuel powders by differential thermal gravimetric analysis (TGA/DTG), Energy Conversion and Management. 85 (2014) 165–172. doi:10.1016/j.enconman.2014.05.068.

[7] L. Nowicki, M. Markowski, Gasification of pyrolysis chars from sewage sludge, Fuel. 143 (2015) 476–483. doi:10.1016/j.fuel.2014.10.056.

[8] S. Werle, S. Sobek, Z. Kaczor, Biomass pyrolysis-the predictions of the process behaviour based on the chemical structure of fuel, Journal of International Scientific Publications. 13 (2019) 128–135.

[9] European Commision, Communication from the Commission to the European Parliament, the Council, the European economic and social Committee and the Committee of the Regions - A policy framework for climate and energy in the period from 2020 to 2030, European Commission. (2014) Brussels. doi:10.1007/s13398-014-0173-7.2.

[10] P. Šuhaj, J. Husár, J. Haydary, Modelling of syngas production from municipal solid waste (MSW) for methanol synthesis, Acta Chimica Slovaca. (2018). doi:10.1515/acs-2017-0019.

[11] M. Edo, N. Skoglund, Q. Gao, P.E. Persson, S. Jansson, Fate of metals and emissions of organic pollutants from torrefaction of waste wood, MSW, and RDF, Waste Management. 68 (2017) 646–652. doi:10.1016/j.wasman.2017.06.017.

[12] P. Wienchol, A. Szlęk, M. Ditaranto, Waste-to-energy technology integrated with carbon capture – Challenges and opportunities, Energy. 198 (2020). doi:10.1016/j.energy.2020.117352.

[13] E.C. Efika, J.A. Onwudili, P.T. Williams, Products from the high temperature pyrolysis of RDF at slow and rapid heating rates, Journal of Analytical and Applied Pyrolysis. 112 (2015) 14–22. doi:10.1016/j.jaap.2015.01.004.

[14] V. Belgiorno, G. De Feo, C. Della Rocca, R.M.A. Napoli, Energy from gasification of solid wastes, Waste Management. (2003). doi:10.1016/S0956-053X(02)00149-6.

[15] N. Kobyashi, Y. Itaya, G. Piao, S. Mori, M. Kondo, M. Hamai, M. Yamaguchi, The behavior

of flue gas from RDF combustion in a fluidized bed, Powder Technology. 151 (2005) 87–95. doi:10.1016/j.powtec.2004.11.038.

[16] J. Chung-Yin Tsai, H.G. Im, T. Kim, J. Kim, Computational modeling of pyrolysis and combustion in a fixed-bed waste gasifier, International Journal of Numerical Methods for Heat & Fluid Flow. 22 (2012) 949–970. doi:10.1108/09615531211271808.

[17] S. Aluri, A. Syed, D.W. Flick, J.D. Muzzy, C. Sievers, P.K. Agrawal, Pyrolysis and gasification studies of model refuse derived fuel (RDF) using thermogravimetric analysis, Fuel Processing Technology. 179 (2018) 154–166. doi:10.1016/j.fuproc.2018.06.010.

[18] A.M.L. Násner, E.E.S. Lora, J.C.E. Palacio, M.H. Rocha, J.C. Restrepo, O.J. Venturini, A. Ratner, Refuse Derived Fuel (RDF) production and gasification in a pilot plant integrated with an Otto cycle ICE through Aspen plus™ modelling: Thermodynamic and economic viability, Waste Management. (2017). doi:10.1016/j.wasman.2017.08.006.

[19] I.H. Hwang, J. Kobayashi, K. Kawamoto, Characterization of products obtained from pyrolysis and steam gasification of wood waste, RDF, and RPF, Waste Management. 34 (2014) 402–410. doi:10.1016/j.wasman.2013.10.009.

[20] H.E. Whyte, K. Loubar, S. Awad, M. Tazerout, Pyrolytic oil production by catalytic pyrolysis of refuse-derived fuels: Investigation of low cost catalysts, Fuel Processing Technology. 140 (2015) 32–38. doi:10.1016/j.fuproc.2015.08.022.

[21] M. Sieradzka, P. Rajca, M. Zajemska, A. Mlonka-Mędrala, A. Magdziarz, Prediction of gaseous products from refuse derived fuel pyrolysis using chemical modelling software - Ansys Chemkin-Pro, Journal of Cleaner Production. (2019) 119277. doi:10.1016/J.JCLEPRO.2019.119277.

[22] J.J. Manyà, F. García-Ceballos, M. Azuara, N. Latorre, C. Royo, Pyrolysis and char reactivity of a poor-quality refuse-derived fuel (RDF) from municipal solid waste, Fuel Processing Technology. 140 (2015) 276–284. doi:10.1016/j.fuproc.2015.09.014.

[23] M.G. Grønli, A theoretical and experimental study of the thermal degradation of biomass, (1996) 282.

[24] T.T. Trinh, S. Werle, K.-Q. Tran, A. Magdziarz, S. Sobek, M. Pogrzeba, Energy crops for sustainable phytoremediation – Fuel characterization, Energy Procedia. 158 (2019) 873–878. doi:10.1016/j.egypro.2019.01.224.

[25] S. Sobek, S. Werle, Thermal Processing of Biomass Using Solar Energy, (2005).

[26] S. Werle, R.K. Wilk, A review of methods for the thermal utilization of sewage sludge: The Polish perspective, Renewable Energy. 35 (2010) 1914–1919. doi:10.1016/j.renene.2010.01.019.

[27] M.J. Prins, K.J. Ptasinski, F.J.J.G. Janssen, More efficient biomass gasification via torrefaction, Energy. 31 (2006) 3458–3470. doi:10.1016/j.energy.2006.03.008.

[28] P. Basu, Biomass Gasification and Pyrolysis Handbook, 2010. doi:http://dx.doi.org/10.1016/B978-0-12-374988-8.00001-5.

[29] T. Pape, H. Hauggaard-nielsen, B. Gøbel, P. Stoholm, J. Ahrenfeldt, U.B. Henriksen, D.S. Müller-stöver, Low temperature circulating fluidized bed gasification and co-gasification of municipal sewage sludge . Part 2 : Evaluation of ash materials as phosphorus fertilizer, Waste Management. 66 (2017) 145–154. doi:10.1016/j.wasman.2017.04.043.

[30] B. Wojnicka, M. Ściążko, J.C. Schmid, Modelling of biomass gasification with steam, Biomass Conversion and Biorefinery. (2019). doi:10.1007/s13399-019-00575-2.

[31] K. Zeng, D. Gauthier, D.P. Minh, E. Weiss-Hortala, A. Nzihou, G. Flamant, Characterization of solar fuels obtained from beech wood solar pyrolysis, Fuel. 188 (2017) 285–293. doi:10.1016/j.fuel.2016.10.036.

[32] Ö. Čepelioɨullar, A.E. Pütün, Products characterization study of a slow pyrolysis of biomass-

plastic mixtures in a fixed-bed reactor, Journal of Analytical and Applied Pyrolysis. 110 (2014) 363–374. doi:10.1016/j.jaap.2014.10.002.

[33] V. Mangut, E. Sabio, J. Gañán, J.F. González, A. Ramiro, C.M. González, S. Román, A. Al-Kassir, Thermogravimetric study of the pyrolysis of biomass residues from tomato processing industry, Fuel Processing Technology. 87 (2006) 109–115. doi:10.1016/j.fuproc.2005.08.006.

[34] S. Wang, G. Dai, H. Yang, Z. Luo, Lignocellulosic biomass pyrolysis mechanism: A state-of-the-art review, Progress in Energy and Combustion Science. 62 (2017) 33–86. doi:10.1016/j.pecs.2017.05.004.

[35] K. Zeng, D. Gauthier, R. Li, G. Flamant, Solar pyrolysis of beech wood: Effects of pyrolysis parameters on the product distribution and gas product composition, Energy. 93 (2015) 1648–1657. doi:10.1016/j.energy.2015.10.008.

[36] S. Werle, K.-Q. Tran, A. Magdziarz, S. Sobek, M. Pogrzeba, T. Løvås, Energy crops for sustainable phytoremediation - Fuel characterization, in: Energy Procedia, 2019. doi:10.1016/j.egypro.2019.01.223.

[37] R. Isemin, A. Mikhalev, D. Klimov, P. Grammelis, N. Margaritis, D.S. Kourkoumpas, V. Zaichenko, Torrefaction and combustion of pellets made of a mixture of coal sludge and straw, Fuel. 210 (2017) 859–865. doi:10.1016/j.fuel.2017.09.032.

[38] M. Atienza-Martínez, I. Fonts, J. ábrego, J. Ceamanos, G. Gea, Sewage sludge torrefaction in a fluidized bed reactor, Chemical Engineering Journal. 222 (2013) 534–545. doi:10.1016/j.cej.2013.02.075.

[39] K. Singh, J. Zondlo, Characterization of fuel properties for coal and torrefied biomass mixtures, Journal of the Energy Institute. 90 (2017) 505–512. doi:10.1016/j.joei.2016.05.012.

[40] Q.V. Bach, O. Skreiberg, Upgrading biomass fuels via wet torrefaction: A review and comparison with dry torrefaction, Renewable and Sustainable Energy Reviews. 54 (2016) 665–677. doi:10.1016/j.rser.2015.10.014.

[41] J.S. Tumuluru, S. Sokhansanj, J.R. Hess, C.T. Wright, R.D. Boardman, A review on biomass torrefaction process and product properties for energy applications, Industrial Biotechnology. 7 (2011) 384–401. doi:10.1089/ind.2011.0014.

[42] S. Sobek, S. Werle, Biomass torrefaction : a brief review, (n.d.).

[43] M. Wilk, A. Magdziarz, K. Jayaraman, M. Szymańska-Chargot, I. Gökalp, Hydrothermal carbonization characteristics of sewage sludge and lignocellulosic biomass. A comparative study, Biomass and Bioenergy. (2019). doi:10.1016/j.biombioe.2018.11.016.

[44] Y. Zhang, W.T. Chen, 5 - Hydrothermal liquefaction of protein-containing feedstocks, in: Direct Thermochemical Liquefaction for Energy Applications, 2018. doi:10.1016/B978-0-08-101029-7.00004-7.

[45] Y. Marcus, Extraction by subcritical and supercriticalwater, methanol, ethanol and their mixtures, Separations. 5 (2018). doi:10.3390/separations5010004.

[46] A. Kubátová, D.J. Miller, S.B. Hawthorne, Comparison of subcritical water and organic solvents for extracting kava lactones from kava root, Journal of Chromatography A. 923 (2001) 187–194. doi:10.1016/S0021-9673(01)00979-7.

[47] K.Q. Tran, Fast hydrothermal liquefaction for production of chemicals and biofuels from wet biomass – The need to develop a plug-flow reactor, Bioresource Technology. 213 (2016) 327–332. doi:10.1016/j.biortech.2016.04.002.

[48] J. Zeaiter, M.N. Ahmad, D. Rooney, B. Samneh, E. Shammas, Design of an automated solar concentrator for the pyrolysis of scrap rubber, Energy Conversion and Management. 101 (2015) 118–125. doi:10.1016/j.enconman.2015.05.019.

[49] M. Sánchez, B. Clifford, J.D. Nixon, Modelling and evaluating a solar pyrolysis system, Renewable Energy. 116 (2018) 630–638. doi:10.1016/j.renene.2017.10.023.
[50] W. Wang, L. Aichmayer, J. Garrido, B. Laumert, Development of a Fresnel lens based high-flux solar simulator, Solar Energy. 144 (2017) 436–444. doi:10.1016/j.solener.2017.01.050.
[51] O. Boutin, M. Ferrer, J. Lédé, Flash pyrolysis of cellulose pellets submitted to a concentrated radiation: Experiments and modelling, Chemical Engineering Science. 57 (2002) 15–25. doi:10.1016/S0009-2509(01)00360-8.
[52] K. Wang, K.H. Kim, R.C. Brown, Catalytic fast pyrolysis of lignocellulosic biomass, Chemical Society Reviews. 43 (2014) ASAP. doi:10.1039/c3cs60414d.
[53] H. Yang, S. Kudo, H.P. Kuo, K. Norinaga, A. Mori, O. Mašek, J.I. Hayashi, Estimation of enthalpy of bio-oil vapor and heat required for pyrolysis of biomass, Energy and Fuels. 27 (2013) 2675–2686. doi:10.1021/ef400199z.
[54] J. Rath, M.G. Wolfinger, G. Steiner, G. Krammer, F. Barontini, V. Cozzani, Heat of wood pyrolysis, Fuel. 82 (2003) 81–91. doi:10.1016/S0016-2361(02)00138-2.
[55] A.K. Burnham, Estimating the Heat of Formation of Foodstuffs and Biomass, (2010) 1–11. https://e-reports-ext.llnl.gov/pdf/459155.pdf.
[56] T. Yuan, A. Tahmasebi, J. Yu, Comparative study on pyrolysis of lignocellulosic and algal biomass using a thermogravimetric and a fixed-bed reactor, Bioresource Technology. 175 (2015) 333–341. doi:10.1016/j.biortech.2014.10.108.
[57] M. Stenseng, A. Jensen, K. Dam-Johansen, Investigation of biomass pyrolysis by thermogravimetric analysis and differential scanning calorimetry, Journal of Analytical and Applied Pyrolysis. 58–59 (2001) 765–780. doi:10.1016/S0165-2370(00)00200-X.
[58] J. Lédé, Biomass pyrolysis: Comments on some sources of confusions in the definitions of temperatures and heating rates, Energies. 3 (2010) 886–898. doi:10.3390/en3040886.
[59] X. Li, Y. Shen, L. Wei, C. He, A.A. Lapkin, W. Lipiński, Y. Dai, C.H. Wang, Hydrogen production of solar-driven steam gasification of sewage sludge in an indirectly irradiated fluidized-bed reactor, Applied Energy. 261 (2020) 114229. doi:10.1016/j.apenergy.2019.114229.
[60] M.C. Ndukwu, I.T. Horsfall, E.A. Ubouh, F.N. Orji, I.E. Ekop, N.R. Ezejiofor, Review of solar-biomass pyrolysis systems: Focus on the configuration of thermal-solar systems and reactor orientation, Journal of King Saud University - Engineering Sciences. (2020). doi:10.1016/j.jksues.2020.05.004.
[61] K. Zeng, R. Li, D.P. Minh, E. Weiss-Hortala, A. Nzihou, D. Zhong, G. Flamant, Characterization of char generated from solar pyrolysis of heavy metal contaminated biomass, Energy. 206 (2020) 118128. doi:10.1016/j.energy.2020.118128.
[62] K. Zeng, J. Soria, D. Gauthier, G. Mazza, G. Flamant, Modeling of beech wood pellet pyrolysis under concentrated solar radiation, Renewable Energy. 99 (2016) 721–729. doi:10.1016/j.renene.2016.07.051.
[63] J. Soria, R. Li, G. Flamant, G.D. Mazza, Influence of pellet size on product yields and syngas composition during solar-driven high temperature fast pyrolysis of biomass, Journal of Analytical and Applied Pyrolysis. 140 (2019) 299–311. doi:10.1016/j.jaap.2019.04.007.
[64] A. Ayala-Cortés, D.R. Lobato-Peralta, C.E. Arreola-Ramos, D.C. Martínez-Casillas, D.E. Pacheco-Catalán, A.K. Cuentas-Gallegos, C.A. Arancibia-Bulnes, H.I. Villafán-Vidales, Exploring the influence of solar pyrolysis operation parameters on characteristics of carbon materials, Journal of Analytical and Applied Pyrolysis. 140 (2019) 290–298. doi:10.1016/j.jaap.2019.04.006.
[65] L. Arribas, N. Arconada, C. Gonzï¿½lez-Fernï¿½ndez, C. Lï¿½hrl, J. Gonzï¿½lez-Aguilar, M. Kaltschmitt, M. Romero, Solar-driven pyrolysis and gasification of low-grade

carbonaceous materials, International Journal of Hydrogen Energy. 42 (2017) 13598–13606. doi:10.1016/j.ijhydene.2017.02.026.

[66] A.H. Rony, D. Mosiman, Z. Sun, D. Qin, Y. Zheng, J.H. Boman, M. Fan, A novel solar powered biomass pyrolysis reactor for producing fuels and chemicals, Journal of Analytical and Applied Pyrolysis. 132 (2018) 19–32. doi:10.1016/j.jaap.2018.03.020.

[67] D.R. Lobato-Peralta, D.E. Pacheco-Catalán, P.E. Altuzar-Coello, F. Béguin, A. Ayala-Cortés, H.I. Villafán-Vidales, C.A. Arancibia-Bulnes, A.K. Cuentas-Gallegos, Sustainable production of self-activated bio-derived carbons through solar pyrolysis for their use in supercapacitors, Journal of Analytical and Applied Pyrolysis. 150 (2020). doi:10.1016/j.jaap.2020.104901.

[68] S. Morales, R. Miranda, D. Bustos, T. Cazares, H. Tran, Solar biomass pyrolysis for the production of bio-fuels and chemical commodities, Journal of Analytical and Applied Pyrolysis. 109 (2014) 65–78. doi:10.1016/j.jaap.2014.07.012.

[69] H. Grassmann, M. Boaro, Solar Biomass Pyrolysis with the Linear Mirror II, Smart Grid and …. (2015) 179–186. http://search.proquest.com/openview/4a55bbabd411640d4f5c1e223d0b86c5/1?pq-origsite=gscholar.

[70] V. Chintala, Production, upgradation and utilization of solar assisted pyrolysis fuels from biomass – A technical review, Renewable and Sustainable Energy Reviews. 90 (2018) 120–130. doi:10.1016/j.rser.2018.03.066.

[71] H. Weldekidan, V. Strezov, G. Town, T. Kan, Production and analysis of fuels and chemicals obtained from rice husk pyrolysis with concentrated solar radiation, Fuel. 233 (2018) 396–403. doi:10.1016/j.fuel.2018.06.061.

[72] A. Namin, C. Jivacate, D. Chenvidhya, K. Kirtikara, J. Thongpron, Construction of tungsten halogen, pulsed LED, and combined tungsten halogen-LED solar simulators for solar cell i - V characterization and electrical parameters determination, International Journal of Photoenergy. 2012 (2012). doi:10.1155/2012/527820.

[73] G. Grandi, A. Ienina, M. Bardhi, Effective low-cost hybrid LED-halogen solar simulator, IEEE Transactions on Industry Applications. 50 (2014) 3055–3064. doi:10.1109/TIA.2014.2330003.

[74] V. Esen, Ş. Sağlam, B. Oral, Light sources of solar simulators for photovoltaic devices: A review, Renewable and Sustainable Energy Reviews. 77 (2017) 1240–1250. doi:10.1016/j.rser.2017.03.062.

[75] M.G. Gronli, M.C. Melaaen, M. Grønli, M.C. Melaaen, Mathematical model for wood pyrolysis - Comparison of experimental measurements with model predictions, Energy & Fuels. 14 (2000) 791–800. doi:10.1021/ef990176q.

[76] O. Authier, J. Lédé, The image furnace for studying thermal reactions involving solids. Application to wood pyrolysis and gasification, and vapours catalytic cracking, Fuel. 107 (2013) 555–569. doi:10.1016/j.fuel.2013.01.041.

[77] V. Pozzobon, S. Salvador, J.J. Bézian, M. El-Hafi, Y. Le Maoult, G. Flamant, Radiative pyrolysis of wet wood under intermediate heat flux: Experiments and modelling, Fuel Processing Technology. 128 (2014) 319–330. doi:10.1016/j.fuproc.2014.07.007.

[78] M. Hu, Z. Chen, S. Wang, D. Guo, C. Ma, Y. Zhou, J. Chen, M. Laghari, S. Fazal, B. Xiao, B. Zhang, S. Ma, Thermogravimetric kinetics of lignocellulosic biomass slow pyrolysis using distributed activation energy model, Fraser-Suzuki deconvolution, and iso-conversional method, Energy Conversion and Management. 118 (2016) 1–11. doi:10.1016/j.enconman.2016.03.058.

[79] D. Tapasvi, R. Khalil, G. Várhegyi, K.-Q. Tran, M. Grønli, Ø. Skreiberg, Thermal

Decomposition Kinetics of Woods with an Emphasis on Torrefaction, Energy & Fuels. 27 (2013) 6134–6145. doi:10.1021/ef4016075.

[80] Z. Sun, B. Xu, A.H. Rony, S. Toan, S. Chen, K.A.M. Gasem, H. Adidharma, M. Fan, W. Xiang, Thermogravimetric and kinetics investigation of pine wood pyrolysis catalyzed with alkali-treated CaO/ZSM-5, Energy Conversion and Management. 146 (2017) 182–194. doi:10.1016/J.ENCONMAN.2017.04.104.

[81] M.Z. Farooq, M. Zeeshan, S. Iqbal, N. Ahmed, S.A.Y. Shah, Influence of waste tire addition on wheat straw pyrolysis yield and oil quality, Energy. 144 (2018) 200–206. doi:10.1016/j.energy.2017.12.026.

[82] K. Gorazda, B. Tarko, S. Werle, Z. Wzorek, Sewage sludge as a fuel and raw material for phosphorus recovery : Combined process of gasification and P extraction, Waste Management. 73 (2018) 404–415. doi:10.1016/j.wasman.2017.10.032.

[83] S. Werle, S. Sobek, Gasification of sewage sludge within a circular economy perspective: a Polish case study, Environmental Science and Pollution Research. 26 (2019). doi:10.1007/s11356-019-05897-2.

[84] T.T. Trinh, S. Werle, K.Q. Tran, A. Magdziarz, S. Sobek, M. Pogrzeba, Energy crops for sustainable phytoremediation - Thermal decomposition kinetics, Energy Procedia. 158 (2019) 873–878. doi:10.1016/j.egypro.2019.01.224.

[85] G. Vtirhegyi, M.J. Antal, E. Jakab, P. Szab, Kinetic modeling of biomass pyrolysis, Journal of Analytical and Applied Pyrolysis. 42 (1997) 73–87.

[86] B.M. Ekman, G. Brooks, M.A. Rhamdhani, Development of high flux solar simulators for solar thermal research, Energy Technology 2015: Carbon Dioxide Management and Other Technologies. 141 (2016) 149–159. doi:10.1007/978-3-319-48220-0_17.

[87] Mantosh K. Chawla, A step by step guide to selecting the " right " Solar Simulator for your solar cell testing application, (2017) 1–6.

[88] X. Dong, Z. Sun, G.J. Nathan, P.J. Ashman, D. Gu, Time-resolved spectra of solar simulators employing metal halide and xenon arc lamps, Solar Energy. 115 (2015) 613–620. doi:10.1016/j.solener.2015.03.017.

[89] A. Georgescu, G. Damache, M.A. Gîrţu, Class A small area solar simulator for dye-sensitized solar cell testing, Journal of Optoelectronics and Advanced Materials. 10 (2008) 3003–3007.

[90] M. Tawfik, X. Tonnellier, C. Sansom, Light source selection for a solar simulator for thermal applications: A review, Renewable and Sustainable Energy Reviews. 90 (2018) 802–813. doi:10.1016/j.rser.2018.03.059.

[91] L.S. Overview, A.L. Sources, D.L. Sources, I. Emitter, No Title, (n.d.).

[92] S. Sobek, Shipping address : Invoice address : Quotation N ° 10391F - Solar Simulator Prospect , Silesian Total :, (n.d.) 135–137.

[93] S. Sobek, Shipping address : Invoice address : Quotation N ° 10391C - Solar Simulator Prospect , Silesian Total :, (n.d.) 135–136.

[94] B. Kongtragool, S. Wongwises, A four power-piston low-temperature differential Stirling engine using simulated solar energy as a heat source, Solar Energy. 82 (2008) 493–500. doi:10.1016/j.solener.2007.12.005.

[95] P. Boulet, G. Parent, Z. Acem, A. Collin, M. Försth, N. Bal, G. Rein, J. Torero, Radiation emission from a heating coil or a halogen lamp on a semitransparent sample, International Journal of Thermal Sciences. 77 (2014) 223–232. doi:10.1016/j.ijthermalsci.2013.11.006.

[96] O. Boutin, M. Ferrer, J. Lédé, Radiant flash pyrolysis of cellulose - Evidence for the formation of short life time intermediate liquid species, Journal of Analytical and Applied Pyrolysis. 47 (1998) 13–31. doi:10.1016/S0165-2370(98)00088-6.

[97] J. Lédé, Comparison of contact and radiant ablative pyrolysis of biomass, Journal of

Analytical and Applied Pyrolysis. 70 (2003) 601–618. doi:10.1016/S0165-2370(03)00043-3.

[98] M.J. Hermoso Orzáez, J.R. De Andrés Díaz, Comparative study of energy-efficiency and conservation systems for ceramic metal-halide discharge lamps, Energy. 52 (2013) 258–264. doi:10.1016/j.energy.2013.01.050.

[99] Z. Kaczor, Z. Bulinski, S. Werle, Numerical studies on capability to focus solar radiation with mirrors of different curvatures, Thermal Science. 23 (2019) 1153–1162. doi:10.2298/tsci19s4153k.

[100] Z. Kaczor, Z. Buliński, S. Werle, Modelling approaches to waste biomass pyrolysis: a review, Renewable Energy. 159 (2020) 427–443. doi:10.1016/j.renene.2020.05.110.

[101] M. Maciejewski, Computational aspects of kinetic analysis. Part B: The ICTAC Kinetics Project - The decomposition kinetics of calcium carbonate revisited, or some tips on survival in the kinetic minefield, Thermochimica Acta. 355 (2000) 145–154. doi:10.1016/S0040-6031(00)00444-5.

[102] A.K. Burnham, Computational aspects of kinetic analysis . Part D : The ICTAC kinetics project Ð multi-thermal ± history model- ® tting methods and their relation to isoconversional methods, 355 (2000) 165–170.

[103] S. Vyazovkin, A.K. Burnham, L. Favergeon, N. Koga, E. Moukhina, L.A. Pérez-Maqueda, N. Sbirrazzuoli, ICTAC Kinetics Committee recommendations for analysis of multi-step kinetics, Thermochimica Acta. 689 (2020) 178597. doi:10.1016/j.tca.2020.178597.

[104] S. Vyazovkin, A.K. Burnham, J.M. Criado, L.A. Pérez-maqueda, C. Popescu, N. Sbirrazzuoli, Thermochimica Acta ICTAC Kinetics Committee recommendations for performing kinetic computations on thermal analysis data, Thermochimica Acta. 520 (2011) 1–19. doi:10.1016/j.tca.2011.03.034.

[105] S. Vyazovkin, Isoconversional Kinetics of Thermally Stimulated Processes, Springer International Publishing Switzerland 2015, 2015.

[106] T. Sonobe, N. Worasuwannarak, Kinetic analyses of biomass pyrolysis using the distributed activation energy model, Fuel. 87 (2008) 414–421. doi:10.1016/j.fuel.2007.05.004.

[107] J.E. White, W.J. Catallo, B.L. Legendre, Biomass pyrolysis kinetics: A comparative critical review with relevant agricultural residue case studies, Journal of Analytical and Applied Pyrolysis. 91 (2011) 1–33. doi:10.1016/j.jaap.2011.01.004.

[108] E. Moukhina, Determination of kinetic mechanisms for reactions measured with thermoanalytical instruments, (2012) 1203–1214. doi:10.1007/s10973-012-2406-3.

[109] S. Vyazovkin, C.A. Wight, Model-free and model-fitting approaches to kinetic analysis of isothermal and nonisothermal data, Thermochimica Acta. 340–341 (2002) 53–68. doi:10.1016/s0040-6031(99)00253-1.

[110] S. Vyazovkin, Modern Isoconversional Kinetics: From Misconceptions to Advances, in: Handbook of Thermal Analysis and Calorimetry, 2018. doi:10.1016/S1573-4374(13)60004-7.

[111] H. Zou, J. Zhang, J. Liu, M. Buyukada, F. Evrendilek, G. Liang, Pyrolytic behaviors, kinetics, decomposition mechanisms, product distributions and joint optimization of Lentinus edodes stipe, Energy Conversion and Management. 213 (2020) 112858. doi:10.1016/j.enconman.2020.112858.

[112] S. Sobek, S. Werle, Kinetic modelling of waste wood devolatilization during pyrolysis based on thermogravimetric data and solar pyrolysis reactor performance, Fuel. (2020). doi:10.1016/j.fuel.2019.116459.

[113] S.S. Ghadikolaei, A. Omrani, M. Ehsani, Non-isothermal degradation kinetics of Ethylene-Vinyl Acetate Copolymer nanocomposite reinforced with modified Bacterial Cellulose

Nanofibers using advanced isoconversional and master plot analyses, Thermochimica Acta. 655 (2017) 87–93. doi:10.1016/j.tca.2017.06.014.

[114] G. Baldauf-Sommerbauer, S. Lux, J. Wagner, M. Siebenhofer, Determination of the kinetic triplet by an isoconversional and a regression method applied to the decomposition of mineral iron carbonate in nitrogen, Thermochimica Acta. 649 (2017) 1–12. doi:10.1016/j.tca.2017.01.001.

[115] P.E. Sánchez-jiménez, L.A. Pérez-maqueda, A. Perejón, J.M. Criado, Thermochimica Acta Generalized master plots as a straightforward approach for determining the kinetic model : The case of cellulose pyrolysis, Thermochimica Acta. 552 (2013) 54–59. doi:10.1016/j.tca.2012.11.003.

[116] J.F. Peters, S.W. Banks, A. V. Bridgwater, J. Dufour, A kinetic reaction model for biomass pyrolysis processes in Aspen Plus, Applied Energy. 188 (2017) 595–603. doi:10.1016/j.apenergy.2016.12.030.

[117] F.C.R. Lopes, K. Tannous, Y.J. Rueda-Ordóñez, Combustion reaction kinetics of guarana seed residue applying isoconversional methods and consecutive reaction scheme, Bioresource Technology. 219 (2016) 392–402. doi:10.1016/j.biortech.2016.07.099.

[118] T.T. Trinh, S. Werle, K.-Q. Tran, A. Magdziarz, S. Sobek, M. Pogrzeba, Energy crops for sustainable phytoremediation – Thermal decomposition kinetics, Energy Procedia. 158 (2019) 873–878. doi:10.1016/j.egypro.2019.01.224.

[119] J. Cai, W. Wu, R. Liu, An overview of distributed activation energy model and its application in the pyrolysis of lignocellulosic biomass, Renewable and Sustainable Energy Reviews. 36 (2014) 236–246. doi:10.1016/j.rser.2014.04.052.

[120] C. Sronsri, B. Boonchom, Deconvolution technique for the kinetic analysis of a complex reaction and the related thermodynamic functions of the formation of LiMn0.90Co0.05Mg0.05PO4, Chemical Physics Letters. 690 (2017) 116–128. doi:10.1016/j.cplett.2017.10.045.

[121] S. Sobek, S. Werle, Solar pyrolysis of waste biomass: Part 2 kinetic modeling and methodology of the determination of the kinetic parameters for solar pyrolysis of sewage sludge, Renewable Energy. (2020). doi:10.1016/j.renene.2020.02.061.

[122] H.L. Friedman, Kinetics of thermal degradation of char-forming plastics from thermogravimetry. Application to a phenolic plastic, Journal of Polymer Science Part C: Polymer Symposia. 6 (1963) 183–195. doi:10.1002/polc.5070060121.

[123] R. Bedoić, V.O. Bulatović, L. Čuček, B. Ćosić, A. Špehar, T. Pukšec, N. Duić, A kinetic study of roadside grass pyrolysis and digestate from anaerobic mono-digestion, Bioresource Technology. 292 (2019) 121935. doi:10.1016/j.biortech.2019.121935.

[124] P. Brachi, F. Miccio, M. Miccio, G. Ruoppolo, Pseudo-component thermal decomposition kinetics of tomato peels via isoconversional methods, Fuel Processing Technology. 154 (2016) 243–250. doi:10.1016/j.fuproc.2016.09.001.

[125] D.R. Streltsov, A.I. Buzin, P. V. Dmitryakov, N.P. Bessonova, P. Kamasa, D.A. Ivanov, S.N. Chvalun, A study of p-xylylene polymerization kinetics by isoconversional analysis, Thermochimica Acta. 573 (2013) 175–180. doi:10.1016/j.tca.2013.09.008.

[126] H. Liu, M.S. Ahmad, H. Alhumade, A. Elkamel, S. Sammak, B. Shen, A hybrid kinetic and optimization approach for biomass pyrolysis: The hybrid scheme of the isoconversional methods, DAEM, and a parallel-reaction mechanism, Energy Conversion and Management. (2020). doi:10.1016/j.enconman.2020.112531.

[127] R. Hilten, J.P. Vandenbrink, A.H. Paterson, F.A. Feltus, K.C. Das, Linking isoconversional pyrolysis kinetics to compositional characteristics for multiple Sorghum bicolor genotypes, Thermochimica Acta. 577 (2014) 46–52. doi:10.1016/j.tca.2013.12.012.

[128] A. Ashraf, H. Sattar, S. Munir, A comparative applicability study of model-fitting and model-free kinetic analysis approaches to non-isothermal pyrolysis of coal and agricultural residues, Fuel. 240 (2019) 326–333. doi:10.1016/j.fuel.2018.11.149.

[129] R.K. Mishra, K. Mohanty, Pyrolysis kinetics and thermal behavior of waste sawdust biomass using thermogravimetric analysis, Bioresource Technology. 251 (2018) 63–74. doi:10.1016/j.biortech.2017.12.029.

[130] A. Chee, R. Lim, B. Lai, F. Chin, Z. Abbas, K. Ling, Kinetic analysis of rice husk pyrolysis using Kissinger-Akahira-Sunose (KAS) method, Procedia Engineering. 148 (2016) 1247–1251. doi:10.1016/j.proeng.2016.06.486.

[131] J. Yan, H. Jiao, Z. Li, Z. Lei, Z. Wang, S. Ren, H. Shui, S. Kang, H. Yan, C. Pan, Kinetic analysis and modeling of coal pyrolysis with model-free methods, Fuel. 241 (2019) 382–391. doi:10.1016/j.fuel.2018.12.079.

[132] A. Soria-Verdugo, E. Goos, N. García-Hernando, U. Riedel, Analyzing the pyrolysis kinetics of several microalgae species by various differential and integral isoconversional kinetic methods and the Distributed Activation Energy Model, Algal Research. 32 (2018) 11–29. doi:10.1016/j.algal.2018.03.005.

[133] M. Gogoi, K. Konwar, N. Bhuyan, R.C. Borah, A.C. Kalita, H.P. Nath, N. Saikia, Assessments of pyrolysis kinetics and mechanisms of biomass residues using thermogravimetry, Bioresource Technology Reports. 4 (2018) 40–49. doi:10.1016/j.biteb.2018.08.016.

[134] D. Xu, M. Chai, Z. Dong, M. Rahman, X. Yu, J. Cai, Kinetic compensation e ff ect in logistic distributed activation energy model for lignocellulosic biomass pyrolysis, 265 (2018) 139–145. doi:10.1016/j.biortech.2018.05.092.

[135] P. Stolarek, S. Ledakowicz, Pyrolysis kinetics of chitin by non-isothermal thermogravimetry, Thermochimica Acta. 433 (2005) 200–208. doi:10.1016/j.tca.2005.03.012.

[136] S.R. Naqvi, R. Tariq, Z. Hameed, I. Ali, M. Naqvi, W.H. Chen, S. Ceylan, H. Rashid, J. Ahmad, S.A. Taqvi, M. Shahbaz, Pyrolysis of high ash sewage sludge: Kinetics and thermodynamic analysis using Coats-Redfern method, Renewable Energy. 131 (2019) 854–860. doi:10.1016/j.renene.2018.07.094.

[137] X. Wang, M. Hu, W. Hu, Z. Chen, S. Liu, Z. Hu, B. Xiao, Bioresource Technology Thermogravimetric kinetic study of agricultural residue biomass pyrolysis based on combined kinetics, Bioresource Technology. 219 (2016) 510–520. doi:10.1016/j.biortech.2016.07.136.

[138] A. Jaramillo-Arango, I. Fonts, F. Chejne, J. Arauzo, Product compositions from sewage sludge pyrolysis in a fluidized bed and correlations with temperature, Journal of Analytical and Applied Pyrolysis. 121 (2016) 287–296. doi:10.1016/j.jaap.2016.08.008.

[139] K.-Q. Tran, S. Werle, T.T. Trinh, A. Magdziarz, S. Sobek, M. Pogrzeba, Fuel characterization and thermal degradation kinetics of biomass from phytoremediation plants, Biomass and Bioenergy. 134 (2020) 105469. doi:https://doi.org/10.1016/j.biombioe.2020.105469.

[140] S.R. Naqvi, Z. Hameed, R. Tariq, S.A. Taqvi, I. Ali, M.B.K. Niazi, T. Noor, A. Hussain, N. Iqbal, M. Shahbaz, Synergistic effect on co-pyrolysis of rice husk and sewage sludge by thermal behavior, kinetics, thermodynamic parameters and artificial neural network, Waste Management. 85 (2019) 131–140. doi:10.1016/j.wasman.2018.12.031.

[141] S.R. Naqvi, R. Tariq, Z. Hameed, I. Ali, S.A. Taqvi, M. Naqvi, M.B.K. Niazi, T. Noor, W. Farooq, Pyrolysis of high-ash sewage sludge: Thermo-kinetic study using TGA and artificial neural networks, Fuel. 233 (2018) 529–538. doi:10.1016/j.fuel.2018.06.089.

[142] A.I. Ferreiro, M. Rabaçal, M. Costa, A combined genetic algorithm and least squares fitting

procedure for the estimation of the kinetic parameters of the pyrolysis of agricultural residues, Energy Conversion and Management. 125 (2016) 290–300. doi:10.1016/j.enconman.2016.04.104.

[143] N. Kongkaew, W. Pruksakit, S. Patumsawad, Thermogravimetric Kinetic Analysis of the Pyrolysis of Rice Straw, 79 (2015) 663–670. doi:10.1016/j.egypro.2015.11.552.

[144] A. Magdziarz, M. Wilk, R. Straka, Combustion process of torrefied wood biomass: A kinetic study, Journal of Thermal Analysis and Calorimetry. 127 (2017) 1339–1349. doi:10.1007/s10973-016-5731-0.

[145] H.A. Shivaee, H.R.M. Hosseini, Advanced isoconversional kinetics of nanocrystallization in Fe73.5Si13.5B9Nb3Cu 1 alloy, Thermochimica Acta. 494 (2009) 80–85. doi:10.1016/j.tca.2009.04.020.

[146] A. Soria-verdugo, M. Rubio-rubio, E. Goos, U. Riedel, Combining the lumped capacitance method and the simpli fi ed distributed activation energy model to describe the pyrolysis of thermally small biomass particles, Energy Conversion and Management. 175 (2018) 164–172. doi:10.1016/j.enconman.2018.08.097.

[147] J.M. Pérez, M. Oliet, M. V. Alonso, F. Rodríguez, Cure kinetics of lignin-novolac resins studied by isoconversional methods, Thermochimica Acta. 487 (2009) 39–42. doi:10.1016/j.tca.2009.01.005.

[148] A.E. Jablonski, A.J. Lang, S. Vyazovkin, Isoconversional kinetics of degradation of polyvinylpyrrolidone used as a matrix for ammonium nitrate stabilization, Thermochimica Acta. 474 (2008) 78–80. doi:10.1016/j.tca.2008.06.003.

[149] F. Ferdosian, M. Ebrahimi, A. Jannesari, Curing kinetics of solid epoxy/DDM/nanoclay: Isoconversional modelsversus fitting model, Thermochimica Acta. 568 (2013) 67–73. doi:10.1016/j.tca.2013.06.001.

[150] V. Dhyani, T. Bhaskar, Kinetic Analysis of Biomass Pyrolysis Kinetic Analysis of Biomass Pyrolysis, Elsevier B.V., 2018. doi:10.1016/B978-0-444-63992-9.00002-1.

[151] C.N. Arenas, M.V. Navarro, J.D. Martínez, Pyrolysis kinetics of biomass wastes using isoconversional methods and the distributed activation energy model, Bioresource Technology. 288 (2019) 121485. doi:10.1016/j.biortech.2019.121485.

[152] S. Hu, A. Jess, M. Xu, Kinetic study of Chinese biomass slow pyrolysis : Comparison of different kinetic models, 86 (2007) 2778–2788. doi:10.1016/j.fuel.2007.02.031.

[153] S. Singh, J. Prasad Chakraborty, M. Kumar Mondal, Intrinsic kinetics, thermodynamic parameters and reaction mechanism of non-isothermal degradation of torrefied Acacia nilotica using isoconversional methods, Fuel. 259 (2020) 116263. doi:10.1016/j.fuel.2019.116263.

[154] A. Anca-Couce, R. Scharler, Modelling heat of reaction in biomass pyrolysis with detailed reaction schemes, Fuel. 206 (2017) 572–579. doi:10.1016/j.fuel.2017.06.011.

[155] R. Li, K. Zeng, J. Soria, G. Mazza, D. Gauthier, R. Rodriguez, G. Flamant, Product distribution from solar pyrolysis of agricultural and forestry biomass residues, Renewable Energy. 89 (2016) 27–35. doi:10.1016/j.renene.2015.11.071.

[156] Z. Ma, D. Chen, J. Gu, B. Bao, Q. Zhang, Determination of pyrolysis characteristics and kinetics of palm kernel shell using TGA – FTIR and model-free integral methods, Energy Conversion and Management. 89 (2015) 251–259. doi:10.1016/j.enconman.2014.09.074.

[157] S. Raza, R. Tariq, Z. Hameed, I. Ali, M. Naqvi, W. Chen, S. Ceylan, H. Rashid, J. Ahmad, S.A. Taqvi, M. Shahbaz, Pyrolysis of high ash sewage sludge : Kinetics and thermodynamic analysis using Coats-Redfern method, Renewable Energy. 131 (2019) 854–860. doi:10.1016/j.renene.2018.07.094.

[158] H. Shahbeig, M. Nosrati, Pyrolysis of municipal sewage sludge for bioenergy production:

Thermo-kinetic studies, evolved gas analysis, and techno-socio-economic assessment, Renewable and Sustainable Energy Reviews. (2019) 109567. doi:10.1016/j.rser.2019.109567.

[159] R. Freund, W. William, Statistical Methods, Second Edi, Academic Press, 2013. doi:10.1017/CBO9781107415324.004.

[160] A. Magdziarz, S. Werle, Analysis of the combustion and pyrolysis of dried sewage sludge by TGA and MS, Waste Management. (2014). doi:10.1016/j.wasman.2013.10.033.

[161] Y.J. Rueda-Ord????ez, K. Tannous, Isoconversional kinetic study of the thermal decomposition of sugarcane straw for thermal conversion processes, Bioresource Technology. 196 (2015) 1–9. doi:10.1016/j.biortech.2015.07.062.

[162] E. Neczaj, K. Fija, A. Grobelak, A. Grosser, Sewage sludge disposal strategies for sustainable development, 156 (2017) 39–46. doi:10.1016/j.envres.2017.03.010.

[163] S. Sobek, S. Werle, Isoconversional determination of the apparent reaction models governing pyrolysis of wood, straw and sewage sludge, with an approach to rate modelling, Renewable Energy. 161 (2020) 972–987. doi:10.1016/j.renene.2020.07.112.

[164] C. Quan, N. Gao, Q. Song, Pyrolysis of biomass components in a TGA and a fixed-bed reactor: Thermochemical behaviors, kinetics, and product characterization, Journal of Analytical and Applied Pyrolysis. 121 (2016) 84–92. doi:10.1016/j.jaap.2016.07.005.

[165] H. Yang, R. Yan, H. Chen, D.H. Lee, C. Zheng, Characteristics of hemicellulose, cellulose and lignin pyrolysis, Fuel. 86 (2007) 1781–1788. doi:10.1016/j.fuel.2006.12.013.

[166] W.J. Liu, W.W. Li, H. Jiang, H.Q. Yu, Fates of Chemical Elements in Biomass during Its Pyrolysis, Chemical Reviews. 117 (2017) 6367–6398. doi:10.1021/acs.chemrev.6b00647.

[167] T. Kan, V. Strezov, T.J. Evans, Lignocellulosic biomass pyrolysis: A review of product properties and effects of pyrolysis parameters, Renewable and Sustainable Energy Reviews. 57 (2016). doi:10.1016/j.rser.2015.12.185.

[168] J.F. Peters, S.W. Banks, A. V. Bridgwater, J. Dufour, A kinetic reaction model for biomass pyrolysis processes in Aspen Plus, Applied Energy. 188 (2017) 595–603. doi:10.1016/j.apenergy.2016.12.030.

[169] J. Alvarez, M. Amutio, G. Lopez, J. Bilbao, M. Olazar, Fast co-pyrolysis of sewage sludge and lignocellulosic biomass in a conical spouted bed reactor, Fuel. 159 (2015) 810–818. doi:10.1016/j.fuel.2015.07.039.

[170] K. Wan, Z. Wang, Y. He, J. Xia, Z. Zhou, J. Zhou, K. Cen, Experimental and modeling study of pyrolysis of coal, biomass and blended coal-biomass particles, Fuel. 139 (2015) 356–364. doi:10.1016/j.fuel.2014.08.069.

[171] J. Alvarez, G. Lopez, M. Amutio, M. Artetxe, I. Barbarias, A. Arregi, J. Bilbao, M. Olazar, Characterization of the bio-oil obtained by fast pyrolysis of sewage sludge in a conical spouted bed reactor, Fuel Processing Technology. 149 (2016) 169–175. doi:10.1016/j.fuproc.2016.04.015.

[172] H. Weldekidan, V. Strezov, R. Li, T. Kan, G. Town, R. Kumar, J. He, G. Flamant, Distribution of solar pyrolysis products and product gas composition produced from agricultural residues and animal wastes at different operating parameters, Renewable Energy. 151 (2020) 1102–1109. doi:10.1016/j.renene.2019.11.107.

[173] A. Anca-Couce, Reaction mechanisms and multi-scale modelling of lignocellulosic biomass pyrolysis, Progress in Energy and Combustion Science. 53 (2016) 41–79. doi:10.1016/j.pecs.2015.10.002.

[174] Y. Shen, X. Li, Z. Yao, X. Cui, C.H. Wang, CO2 gasification of woody biomass: Experimental study from a lab-scale reactor to a small-scale autothermal gasifier, Energy. 170 (2019) 497–506. doi:10.1016/j.energy.2018.12.176.

[175] T. Ohra-Aho, J. Linnekoski, Catalytic pyrolysis of lignin by using analytical pyrolysis-GC-MS, Journal of Analytical and Applied Pyrolysis. 113 (2015) 186–192. doi:10.1016/j.jaap.2014.12.012.

[176] Q. Yan, J. Li, J. Zhang, Z. Cai, Thermal decomposition of Kraft Lignin under Gas atmospheres of argon, hydrogen, and carbon dioxide, Polymers. 10 (2018). doi:10.3390/polym10070729.

[177] S. Werle, S. Sobek, Gasification of sewage sludge within a circular economy perspective: a Polish case study, Environmental Science and Pollution Research. (2019). doi:10.1007/s11356-019-06162-2.

[178] H. Seifi, S.M. Sadrameli, Bound cleavage at carboxyl group-glycerol backbone position in thermal cracking of the triglycerides in sunflower oil, Journal of Analytical and Applied Pyrolysis. 121 (2016) 1–10. doi:10.1016/j.jaap.2016.06.006.

[179] P. Lahijani, Z.A. Zainal, M. Mohammadi, A.R. Mohamed, Conversion of the greenhouse gas CO2 to the fuel gas CO via the Boudouard reaction: A review, Renewable and Sustainable Energy Reviews. 41 (2015) 615–632. doi:10.1016/j.rser.2014.08.034.